

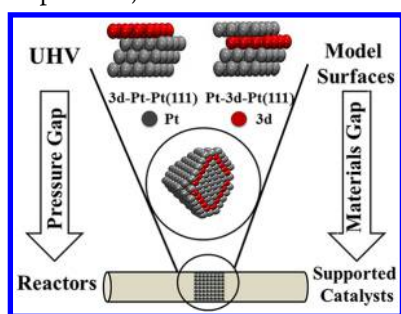
Review of Pt-Based Bimetallic Catalysis: From Model Surfaces to Supported Catalysts

Weiting Yu,[†] Marc D. Porosoff,[†] and Jingguang G. Chen^{*,†,‡,§}

[†]Catalysis Center for Energy Innovation, Department of Chemical and Biomolecular Engineering, University of Delaware, Newark, Delaware 19716, United States

[‡]Department of Chemical Engineering, Columbia University, New York, New York 10027, United States

[§]Chemistry Department, Brookhaven National Laboratory, Upton, New York 11973, United States



CONTENTS

1. Introduction	5780
1.1. Unique Properties of Bimetallic Surfaces and Catalysts	5780
1.2. Scope of the Current Review	5781
2. Preparation and Characterization of Bimetallic Surfaces and Catalysts	5781
2.1. Model Surfaces	5781
2.1.1. Preparation of Bimetallic Surfaces	5781
2.1.2. Common Characterization Techniques for Bimetallic Surfaces	5782
2.1.3. Example: Characterization of Ni/Pt Bimetallic Surfaces	5782
2.2. Supported Catalysts	5783
2.2.1. Synthesis of Supported Bimetallic Catalysts	5783
2.2.2. Common Characterization Techniques for Bimetallic Catalysts	5786
2.2.3. Example: Characterization of Supported Pt–Ni Bimetallic Catalysts	5788
3. Stability of Pt-Based Bimetallic Surfaces with Different Adsorbates	5788
3.1. DFT Calculations of Thermodynamic Stability	5788
3.2. Experimental Verification of Surface Segregation	5789
4. Utilization of Pt-Based Bimetallic Catalysts in Catalytic Reactions	5791
4.1. Hydrogenation Reactions	5791
4.1.1. C=C Hydrogenation	5791
4.1.2. C=O Hydrogenation	5796
4.1.3. N=O and C≡N Hydrogenation	5799
4.2. Dehydrogenation Reactions	5800
4.2.1. N–H Bond Scission	5800
4.2.2. C–H Bond Scission	5800
4.3. Reforming of Oxygenates	5803

4.3.1. Reforming of Alcohols and Polyols	5803
4.3.2. Reforming of Other Oxygenates	5805
4.4. Other Important Catalytic Reactions	5805
4.4.1. CO Oxidation	5805
4.4.2. Water Gas Shift Reaction	5808
4.4.3. CH ₄ Conversion	5808
4.5. Brief Summary of Pt-Based Bimetallic Electrocatalysts	5808
4.6. Brief Summary of Trimetallic Catalysts	5809
5. Conclusions and Future Research Opportunities	5809
Author Information	5810
Corresponding Author	5810
Notes	5810
Biographies	5810
Acknowledgments	5810
Dedication	5810
List of Abbreviations	5810
References	5811

1. INTRODUCTION

1.1. Unique Properties of Bimetallic Surfaces and Catalysts

The field of heterogeneous catalysis, specifically catalysis on bimetallic alloys, has seen many advances over the past few decades. Bimetallic catalysts, which often show electronic and chemical properties that are distinct from those of their parent metals, offer the opportunity to obtain new catalysts with enhanced selectivity, activity, and stability. Bimetallic catalysts started to gain considerable commercial interest in the 1960s for their use in hydrocarbon reforming because they displayed activities unlike those of the monometallic catalysts.^{1–3} The findings of these unexpected properties of bimetallic catalysts have inspired many extensive investigations on their possible applications. Currently bimetallic catalysts are widely utilized in many catalytic⁴ and electrocatalytic^{5,6} applications.

To understand the origins of the novel catalytic properties, bimetallic surfaces have also gained a considerable amount of interest for fundamental surface science research, as summarized in several earlier reviews.^{7–9} It is now well-known that bimetallic surfaces often show novel properties that are not present on either of the parent metal surfaces.^{7,8,10–23} The modification effect is especially important when the admetal coverage is in the submonolayer to monolayer regime.

Received: March 7, 2012

Published: August 24, 2012

However, it is difficult to know a priori how the electronic and chemical properties of a particular bimetallic surface will be modified relative to the parent metals. For this reason, the study of bimetallic surfaces in the field of catalysis has gained considerable interest. There are two critical factors that contribute to the modification of the electronic and chemical properties of a metal in a bimetallic surface. First, the formation of heteroatom bonds changes the electronic environment of the metal surface, giving rise to modifications of its electronic structure through the ligand effect. Second, the geometry of the bimetallic structure is typically different from that of the parent metals, e.g., the average metal–metal bond lengths change, resulting in the strain effect that is known to modify the electronic structure of the metal through changes in orbital overlap.¹⁶

In the past decade there have been significant efforts in density functional theory (DFT) calculations and ultrahigh vacuum (UHV) experiments on bimetallic surfaces. One of the new findings is that, depending on experimental conditions, the monolayer admetal can interact with the host metal substrate in one of the three structures: occupying the topmost surface sites to produce the *surface monolayer*, diffusing into the subsurface region to form the *subsurface monolayer*, and alloying with the surface to produce *intermixed bimetallic* surfaces. DFT modeling results clearly indicate that the modification on the surface d-band center is significantly different for the three types of bimetallic structures. Surface science results, using several probe molecules, also confirm the different chemical properties of bimetallic surfaces with *surface monolayer* and *subsurface monolayer* structures. In addition, the combination of DFT modeling and experimental results reveal a general correlation between the position of the surface d-band center and the adsorption energy for various bimetallic structures, making it possible to predict bimetallic structures with desirable chemical properties.

1.2. Scope of the Current Review

Although studies on model bimetallic surfaces provide fundamental insight into the novel catalytic properties, in an industrially relevant supported catalyst the active metal will be present in the form of nanoparticles on a high-surface-area support. The primary objective of the current review is to provide correlations between model surfaces and supported catalysts for several types of catalytic reactions. In particular, we will attempt to bridge the “materials gap” between model surfaces and supported catalysts and the “pressure gap” between UHV environment and reaction environment. We will utilize successful examples, such as hydrogenation reactions, to demonstrate the feasibility of bridging the materials and pressure gaps between model surfaces and real-world catalysis. We will also use other reactions to point out the challenges in applying fundamental surface science studies to predict stable bimetallic structures for catalysis.

Because of the enormous volumes of work in bimetallic catalysis, in the current review we will focus on Pt-based bimetallic surfaces and catalysts. The reasons for choosing Pt-based bimetallic systems are primarily 2-fold: (i) they are the most well-studied bimetallic surfaces using both DFT calculations and surface science experiments, and (ii) they are among the most commonly used bimetallic catalysts in both catalytic and electrocatalytic applications. In addition, other bimetallic catalysts without Pt also have interesting properties and important applications. In many cases, the benefits of Pt-

free bimetallic alloys are similar to those achieved with Pt. These bimetallic combinations also have similarly modified electronic properties that lead to increased activity and selectivity.²⁴ For example, Au–Ag catalysts are active for CO oxidation because the synergistic interaction between the two metals improves the catalytic performance. In this case, Au adsorbs CO molecules and the neighboring Ag adsorbs reactive oxygen species.²⁵ Non-noble metal bimetallic catalysts are also of interest because of the potential savings in material cost. The Ni–Cu system is one example that has been previously studied for the hydrolysis of NaBH₄ to release hydrogen.²⁶ Although non-Pt-containing systems have important applications, the scope of this review article is limited to Pt-based catalysts to provide a focused and in-depth review of bimetallic catalysis. In section 2 we will utilize one of the most thoroughly studied bimetallic systems, Ni/Pt, to introduce the preparation procedures and common characterization techniques for both bimetallic surfaces and supported catalysts. This will be followed in section 3 by DFT calculations and experimental verification of stable bimetallic structures under different reaction conditions. In section 4 we will summarize the unique properties and general trends of bimetallic surfaces and catalysts for different types of reactions, including hydrogenation, dehydrogenation, reforming, and oxidation reactions. The review will conclude by pointing out challenges and research opportunities for further advancing bimetallic catalysis.

2. PREPARATION AND CHARACTERIZATION OF BIMETALLIC SURFACES AND CATALYSTS

2.1. Model Surfaces

2.1.1. Preparation of Bimetallic Surfaces. Among the various deposition methods, physical vapor deposition (PVD) is most compatible with the UHV environment necessary for surface science studies. The PVD methods utilize line-of-sight deposition to produce a metal overlayer on the target substrate. The controlling parameters of typical PVD synthesis include the rate of metal vapor flux, time of deposition, substrate temperature, and deposition environment such as in vacuum or in the background of selected gases. Common PVD methods include magnetron sputtering, pulsed laser deposition, e-beam sputtering, and physical evaporation of the overlayer metal via thermal filament. Figure 1 shows the typical experimental setup of a metal source for thermal evaporation. The metal source consists of a thin (typically 0.2–0.5 mm) tungsten (W) or tantalum (Ta) wire, which is wrapped around with wire (typically 0.05–0.1 mm) of the metal of interest. The W or Ta

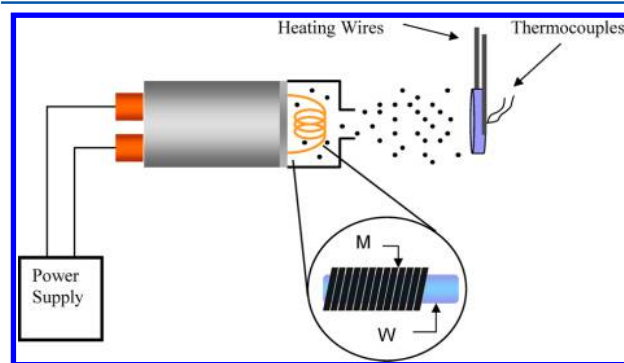


Figure 1. Schematic diagram of line-of-sight deposition of metal overlayer by physical vapor deposition with thermal filament.

wire is connected to the power supply through a UHV feedthrough to a DC or AC power supply for resistive heating. The extremely high melting temperature of the W or Ta filament allows deposition of the metal of interest without contamination from W or Ta. The evaporation filament is typically housed in a stainless steel cylinder, with a small opening at the front face of the cylinder to direct the metal deposition onto the substrate and to prevent the evaporation of metals onto other components in the UHV system. The metal source is gradually heated to the temperature of evaporation and held for a certain amount of time to achieve reproducible deposition of an impurity-free metal overlayer. Such conditioning of the source takes many hours, often at a current or voltage slightly higher than what is used for the metal deposition. The pressure in the UHV system should be 5×10^{-10} Torr or lower during evaporation to prevent the accumulation of background impurities on the bimetallic surface.

Procedures for the preparation of bimetallic surface structures under UHV conditions have been described in detail previously.^{27,28} For example, when a 3d transition metal is deposited onto a Pt(111) surface at 300 K, the 3d atoms stay on the topmost layer to produce the 3d–Pt–Pt(111) surface configuration. If this surface is subsequently heated to 600 K, or if the monolayer deposition of the 3d metal occurs with the Pt(111) substrate held at 600 K, most of the 3d atoms diffuse into the subsurface region to produce the Pt–3d–Pt(111) subsurface structure. As shown in Figure 2, monolayer

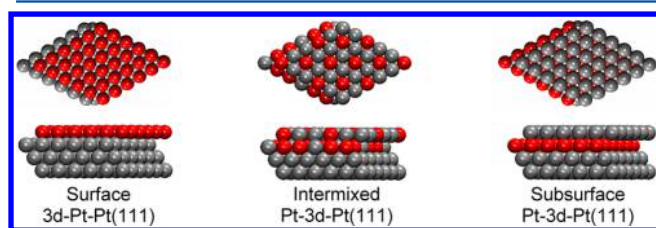


Figure 2. Idealized bimetallic surface structures with one monolayer of 3d metals on a Pt(111) substrate.

bimetallic surfaces can have three idealized configurations: a surface 3d–Pt–Pt(111) configuration, where the metal monolayer grows epitaxially on the surface of the Pt substrate; an intermixed configuration, where the 3d atoms reside in the first two Pt layers to some varying degree; and the subsurface Pt–3d–Pt(111) configuration, where the first layer is composed of Pt atoms and the second layer consists of the 3d atoms. Determination of the structures and elemental compositions of various bimetallic surfaces requires the utilization of a battery of UHV techniques, as described in the next section.

2.1.2. Common Characterization Techniques for Bimetallic Surfaces. *Auger Electron Spectroscopy and X-ray Photoelectron Spectroscopy.* The Auger electron spectroscopy (AES) peak-to-peak intensities and X-ray photoelectron spectroscopy (XPS) peak areas are often used to quantify the elemental compositions of bimetallic surfaces after normalization by the relevant sensitivity factors and consideration of the sampling depth of the Auger electrons or photoelectrons.¹⁰ AES and XPS are also useful techniques to determine the growth mechanism of the metal overlayer, either in a layer-by-layer fashion or via 3-dimensional (3D) island formation. In the latter growth mechanism, a uniform monolayer is not formed because the cohesive energy between

metal overlayer atoms (M–M) is generally higher than the adsorption energy between the metal overlayer and the substrate surface (M–S). The layer-by-layer and the 3D island growth mechanisms can often be differentiated by measuring the AES or XPS intensities as a function of deposition time. In the layer-by-layer mechanism, the peak intensity of both the metal overlayer and the substrate show distinct breaks, with the first break indicating the deposition time for the completion of the first monolayer. In contrast, such breaks are absent for the 3D island growth mechanism.¹⁰ Because of the relative ease of these experiments, the AES or XPS growth calibration curves should be measured whenever a new overlayer/substrate system is investigated.

Low-Energy Ion Scattering. Compared with AES and XPS, low-energy ion scattering (LEIS)²⁹ is much more sensitive in detecting the elemental composition of the topmost layer of bimetallic surfaces. In LEIS experiments, the surface is bombarded with positive ions of an inert element, such as He, Ne, or Ar, at a relatively low energy (100–5000 eV). The incident ions are scattered back with an energy that is directly related to the mass of the surface atom with which they collide. Because the ions have different sensitivities toward atoms of different atomic numbers, the intensity of the scattering peaks needs to be normalized to the intensity of a pure surface of each element. In the case of bimetallic surfaces, the sensitivity factor for the substrate is determined by measuring the intensity of the LEIS signal for a clean substrate surface and that of the thick metal film of interest.

Low-Energy Electron Diffraction. Low-energy electron diffraction (LEED) is a useful technique to determine the overlayer structure in bimetallic surfaces. LEED is very useful in identifying the periodicity of the metal overlayer with respect to the single-crystal substrate.^{30,31} For example, LEED studies have helped reveal that bimetallic alloy surfaces, such as Pt₈₀Ni₂₀(001), Pt₈₀Co₂₀(111), and Pt₈₀Fe₂₀(111), all exhibit a pure Pt outermost layer with a Pt-depleted layer underneath.³² LEED measurements are also important to confirm the epitaxial growth of the metal overlayer.

Scanning Tunneling Microscopy. Scanning tunneling microscopy (STM) is often used to determine the structure and morphology of the metal overlayer in bimetallic surfaces. In STM experiments a tip is scanned over a sample surface in a regular array, adjusting the height of the tip to keep either the tunneling current or the voltage constant between the STM tip and the surface. The fluctuations of intensity can often be related to differing elements, which is useful in determining the growth mechanism of the metal overlayer as well as the morphology of bimetallic surfaces.

2.1.3. Example: Characterization of Ni/Pt Bimetallic Surfaces. In this section we will illustrate the synthesis and characterization of bimetallic surfaces following the deposition of one monolayer of Ni on either a Pt(111) single crystal or a polycrystalline Pt substrate. The characterization of Ni/Pt(111) bimetallic surfaces is very useful in providing structural models for DFT calculations. It is also critical in correlating bimetallic structures with the electronic and chemical properties of bimetallic surfaces.¹⁰

For example, Figure 3 shows the LEIS and AES results following the annealing of the 300 K Ni–Pt–Pt(111) surface to 900 K. For the LEIS experiments (Figure 3a), Ni was deposited at 300 K and the initial coverage of Ni was ~ 1 ML. After a small initial increase in the Ni intensity, possibly due to desorption of contaminant H₂, the Ni intensity decreased

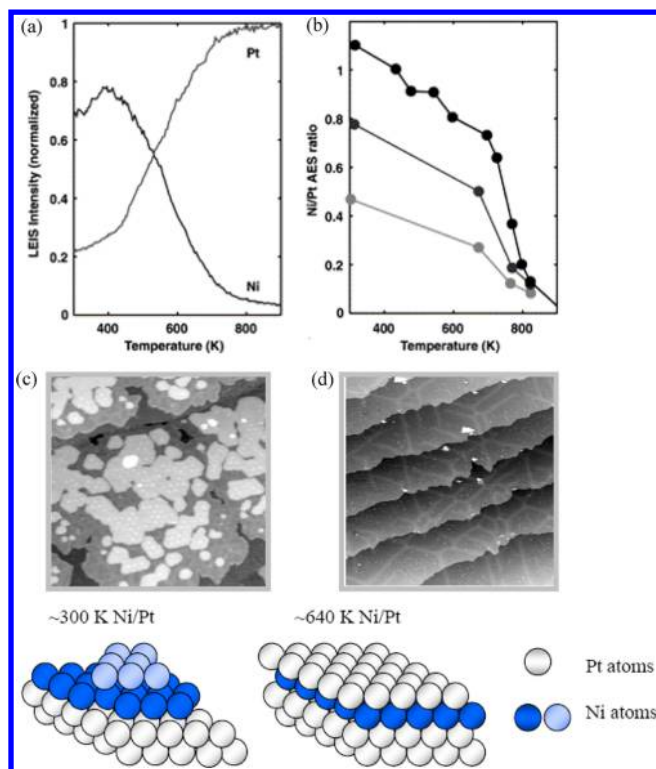


Figure 3. Schematics of surface Ni–Pt–Pt(111) and subsurface Pt–Ni–Pt(111) structures derived from AES, low-energy ion scattering (LEIS), and scanning tunneling microscopy (STM).²⁸

significantly with increasing temperature until it became nearly undetectable by 800 K. There were corresponding increases in the Pt intensity as the annealing temperature increased. Similar trends were observed in the AES experiments (Figure 3b), which were performed at three different initial coverages. The Ni/Pt AES ratio underwent significant decreases at above 700 K, indicating the diffusion of Ni into regions that were beyond the detection limit of the AES measurements.^{27,28}

The STM images provided further characterization of the 300 and 640 K Ni/Pt(111) surfaces. As shown in Figure 3c, after deposition at 300 K, Ni atoms formed islands that were a single atomic layer thick and nucleated at the step edges of the Pt(111) surface. Upon annealing to 640 K, all of the island features disappeared, as shown in Figure 3d. The surface appeared fairly uniform, with many small, “wormlike” features, which were attributed to the strain caused by the subsurface Ni atoms in Pt(111). Overall, the AES, LEIS, XPS, and STM results confirmed the presence of a surface Ni monolayer on Pt(111) after the deposition of Ni at 300 K. The characterization following annealing to 600–640 K was consistent with the diffusion of Ni into the subsurface region of Pt(111); the possibility of the production of the Pt–Ni–Pt(111) structure, with Ni atoms staying directly underneath the surface Pt, was further suggested from DFT calculations and experimental measurements of chemical properties, as described later.

In practice, bimetallic catalysts are often supported nanoparticles of varying shape and size. Polycrystalline bimetallic films provide a potential way to bridge the “materials gap” between single-crystal surfaces and supported catalysts. As illustrated in Figure 4, it is reasonable to assume that the surface chemistry of the nanoparticle should be dominated primarily by the first few atomic layers. It is also reasonable to assume that the chemistry of the individual crystal facets on the nanoparticle

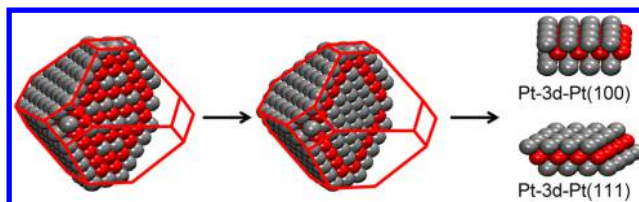


Figure 4. Schematic of the (100) and (111) regions of a supported bimetallic particle.²⁰⁰

(primarily (111) and (100) for a face-centered cubic (fcc) nanoparticle) can be approximated by their respective single-crystal extensions. With these assumptions, Menning and Chen deposited Ni on a polycrystalline Pt film that contained mainly the (111) and (100) facets to mimic supported bimetallic particles.³³ Similar to Pt(111), monolayer Ni was deposited on the polycrystalline Pt foil at room temperature to produce the Ni–Pt–Pt surface structure, followed by annealing to higher temperatures to obtain the Pt–Ni–Pt subsurface structure. More about the similar catalytic properties between single-crystal Pt–Ni–Pt(111), polycrystalline Pt–Ni–Pt, and supported Pt–Ni catalysts will be illustrated later.

In addition to the examples given above, many UHV techniques have been utilized to characterize the surface structures of several bimetallic systems. Table 1 provides a list of selected bimetallic surfaces, along with the corresponding UHV techniques or theoretical calculations used to characterize the surface properties.

2.2. Supported Catalysts

2.2.1. Synthesis of Supported Bimetallic Catalysts.

Supported bimetallic catalysts have been synthesized using a wide range of synthesis techniques. In this section we will provide a summary of some of the most commonly utilized synthesis methods and the potential advantages of each method.

Wet Impregnation Method. Incipient wetness impregnation is the most commonly utilized method because of its ease in sample preparation. It involves infusing the desired support material with a solution containing a precursor of the desired metallic species. The support is impregnated with a volume of precursor solution that is equal to the pore volume of the support material. The amount of precursor required is calculated based on the desired metal loading for each catalyst, and the volume of the pores of the support material is measured prior to impregnation using deionized water.¹³⁷ To synthesize the catalyst, a known mass of a metal precursor is dissolved in a solvent. Deionized water is the most commonly used solvent for wet impregnation, but research groups have also used Pt–acetylacetonates dissolved in toluene to avoid acidification of the support,¹³⁸ ethylene glycol,¹³⁹ formic acid,¹⁴⁰ and acetone.¹⁴¹ Catalysts can also be prepared with organometallic bimetallic molecular precursors. These precursors are advantageous to traditional metallic salts because the bimetallic bond is already present, leading to a higher extent of bimetallic bonds and a higher activity of bimetallic catalysts.¹⁴²

Once the precursor is fully dissolved, the solution is added dropwise to the support. Capillary action carries the aqueous solution up into the pores of the support, where the metal precursor is deposited. By varying the drying rate of the catalyst, the precursor can deposit deep within the pores or solely at the pore entrances. After drying, the catalyst is calcined

Table 1. Summary of Studies of Pt-Based Bimetallic Surfaces and the Corresponding Characterization Techniques and Computational Methods

surface	technique	surface	technique
Pt/Co(111)	DFT, ³⁴ MD ³⁵	Ni/Pt(111)	AES, ^{28,54,64,88–90} LEED, ^{28,88–90} STM, ²⁸ LEIS, ²⁸ MCS, ⁹¹ DFT ^{64,68,92}
Pt/Cu(100)	CAICISS, ³⁶ LEED, ^{36–41} XPS, ³⁶ LEIS, ³⁶ PES, ⁴⁰ BFS, ⁴² AES ⁴¹	Ni ₅₀ Pt ₅₀ (111)	MCS ⁸⁷
Pt/Cu(111)	DFT, ⁴³ AES, ^{44,45} TDS, ⁴⁴ PES, ⁴⁶ LEED, ^{45,47} MEIS, ⁴⁸ LEIS ^{47,49,50}	Ni/Pt(997)	STM ⁹³
PtAu cluster	DFT ⁵¹	Pd/Pt(111)	CV, ⁹⁴ FTIR, ⁹⁴ DFT, ⁹⁵ SXS ⁹⁶
Pt/Ni(110)	XPS, ⁵² LEED ⁵²	Rh/Pt(100)	STM, ⁹⁷ LEED ⁹⁷
Pt/Ni(111)	AES, ^{53,54} DFT ^{34,55}	Rh/Pt(110)	STM, ⁹⁷ LEED ⁹⁷
Pt/Pd(111)	PES ^{56,57}	Ru/Pt(100)	LEED, ⁹⁸ XPS, ^{98,99} IRAS ⁹⁹
Al/Pt(111)	XPS, ⁵⁸ AES, ⁵⁸ STM ⁵⁸	Ag/Pt(100)	STM, ¹⁰⁰ AES ¹⁰⁰
Ce/Pt(111)	LEED, ⁵⁹ XPS ⁵⁹	Ag/Pt(111)	DFT, ⁴³ PES, ¹⁰¹ STM, ^{102,103} LEED, ^{104–106} AES, ^{104,105} UPS ^{104,105}
Co/Pt(111)	AES, ^{60–64} LEED, ^{61,63,65,66} UPS, ⁶¹ STM, ⁶⁵ DFT, ^{64,67,68} SMOKE, ^{62,69,70} MEIS ^{69,70}	Ag/Pt(997)	PES ¹⁰¹
Co ₂₀ Pt ₈₀ (111)	IS, ⁷¹ MCS ⁷¹	Sn/Pt(100)	AES, ^{107–109} STM, ¹⁰⁷ LEED, ^{107–109} ALISS ¹⁰⁹
Cu/Pt(100)	PAX, ⁷² AES, ⁷² LEED ⁷²	Sn/Pt(111)	AES, ^{110–112} LEED, ^{111–116} DFT, ¹¹⁷ XPS, ^{112,113,115} STM, ¹¹² CV, ¹¹³ PES ^{114,116}
Cu/Pt(111)	HAS, ⁷³ STM, ⁷³ AES, ^{74,75} PES ⁴⁶	Ti/Pt(111)	DFT ^{64,68}
Cu/Pt(12 12 11)	HAS, ⁷⁶ MEIS ⁷⁶	Tm/Pt(111)	LEED, ¹¹⁸ XPS ¹¹⁸
Cr/Pt(001)	DFT ⁷⁷	V/Pt(001)	DFT ⁷⁷
Cr/Pt(111)	STM, ⁷⁸ DFT ^{64,68}	V/Pt(111)	DFT ^{64,68}
Au/Pt(111)	XPS ⁷⁹	Pt/Rh(100)	LEIS, ¹¹⁹ PES, ¹²⁰ LEED, ⁹⁷ STM ⁹⁷
Au/polycrystalline Pt	XPS, ⁸⁰ TPD ⁸⁰	Pt/Rh(110)	LEED, ⁹⁷ STM ⁹⁷
AuPt clusters	DFT ⁵¹	Pt/Rh(111)	AES, ¹²¹ UPS, ¹²¹ LEIS, ¹²¹ STM, ¹²¹ PAX ¹²¹
Fe/Pt(111)	DFT, ^{64,68} XPS, ⁸¹ LEED, ⁸¹ LEIS ⁸¹	Pt ₂₅ Rh ₇₅ (410)	LEIS ¹²²
Fe/Pt(997)	TEAS, ⁸² AES ⁸²	Pt/Ru(0001)	STM ^{123–125}
La/Pt(111)	PES, ^{83,84} LEED ⁸⁴	Pt/W(110)	LEED, ¹²⁶ $\Delta\Phi$, ¹²⁶ AES ¹²⁷
Mn/Pt(001)	DFT ⁷⁷	Pt/W(111)	HRXPS, ¹²⁸ SXPS, ^{9,129} AES, ⁹ LEED, ⁹ LEEM, ^{9,130} TPD, ⁹ STM, ¹³⁰ FEM ¹³¹
Mn/Pt(111)	DFT ^{64,68}	Pt/W(211)	SXPS, ^{9,132,133} AES, ^{9,132–134} LEED, ^{9,133,134} LEEM, ⁹ TPD, ^{9,133,134} DFT, ¹³⁵ STM ¹³⁴
Mo/Pt(111)	XPS, ⁸⁵ LEED, ⁸⁶ AES, ⁸⁶ $\Delta\Phi$ ⁸⁶	Pt/Re(1121)	LEED, ¹³⁶ STM, ¹³⁶ LEIS, ¹³⁶ XPS ¹³⁶
Ni ₅₀ Pt ₅₀ (110)	MCS ⁸⁷		

at high temperature to vaporize the nonmetallic components of the precursor salt, leaving the metal in an oxidized state on the support surface. Calcination is required to stabilize metals on the support surface and to prevent metal dissolution when exposed to moisture. Incipient wetness impregnation of bimetallic catalysts can be performed sequentially or simultaneously. In sequential impregnation, one metal is impregnated first, and then the catalyst is dried and calcined. After calcination, the second metal is impregnated to complete the catalyst synthesis. Sequential impregnation is preferred in cases where the metal precursors react with each other, but it has been shown that simultaneous impregnation of a bimetallic catalyst yields a greater extent of bimetallic bond formation and higher activity.¹⁴³ For example, Lonergan et al. have shown that Pt–Ni catalysts synthesized by simultaneous impregnation were more active for 1,3-butadiene and benzene hydrogenation than catalysts synthesized using sequential impregnation.¹⁴³

Slurry Synthesis Method. This method is used for synthesizing catalysts with high metal loadings and/or supports with low surface areas. The slurry is made with the support material, metal precursor, and water. The amounts of support and precursor are chosen to achieve the desired weight loading of catalyst, and typically ~15 mL of deionized water is used for each gram of catalyst. After mixing the components, the slurry is stirred for at least 8 h, during which an equilibrium amount of the precursor should adsorb to the support.¹⁴⁴ During stirring, the pH value is controlled to a set level using NaOH. Once the

set stirring time has elapsed, the slurry is filtered and washed and then placed in a drying oven to evaporate the excess water. Catalysts are calcined at high temperatures after drying to stabilize the metal on the support and to remove unwanted elements from the metal precursors. This synthesis method has been used to prepare catalysts for the hydrogenation of nitroaromatics, which shows that adding a small amount of Pt to an Au/TiO₂ catalyst increases the hydrogenation activity by an order of magnitude.¹⁴⁴

Organometallic Cluster Precursors. Metal segregation, sintering, surface enrichment of one of the metals, and the inherent heterogeneity of bimetallic particles make the preparation of highly dispersed and uniform bimetallic particles difficult with conventional impregnation and slurry methods.¹⁴⁵ The dispersion of the active phase on the surface of a support is controlled by many factors, including the support type, method of preparation, calcination conditions, precursors, and metal loading.¹⁴⁶ A common problem of impregnation and slurry techniques is the separation of the precursor ions as they pass through the pore structure of the support, preventing the effective formation of the bimetallic bonds. An improved method to achieve higher uniformity of bimetallic catalysts is to adsorb ligand-stabilized bimetallic molecular precursors onto the support and then thermally remove the ligands.¹⁴⁷ For example, a bimetallic cluster, [(PPh₃)Pt(AuPPh₃)₆](NO₃)₂, is used to prepare a Pt–Au catalyst particle, previously described in detail for different bimetallic precursors.¹⁴⁸ The organo-

metallic cluster is mixed with an organic solvent such as CH_2Cl_2 , and the cluster solution is slowly added to the oxide support with constant swirling. The clusters are spontaneously adsorbed onto the oxide support, and the remaining solvent is decanted. Residual solvent is removed by heating in vacuum, and the clusters are activated by heating in oxygen up to 573 K. Studies have shown that the bimetallic core of the cluster remains intact while the ligands are removed after heating.¹⁴⁵ In probe reactions of ethanol reforming, bimetallic catalysts synthesized with organometallic clusters outperformed catalysts synthesized using traditional impregnation methods.¹⁴⁹

Reductive Deposition Precipitation. This is a useful method to produce highly coordinated bimetallic catalysts from monometallic catalysts. It is an alternative to the organometallic precursor method, which sometimes experiences premature decomposition of the organometallic complex, leading to inactive phases on the catalyst support.¹⁴⁰ In reductive deposition precipitation, a monometallic catalyst, for example, Pt, is prepared by conventional wet impregnation or slurry methods and then held under hydrogen. The hydrogen atoms adsorbed on the Pt particles react with a second metal precursor, resulting in the formation of a bimetallic surface complex. The surface complex is decomposed in hydrogen, leading to formation of a stabilized bimetallic species.¹⁵⁰ However, this method does not exclusively lead to formation of bimetallic particles, with some of the second metal precursor also depositing on the support.¹⁵¹ Ekou et al. have shown that Pt–Ge/TiO₂ catalysts synthesized using the reductive deposition precipitation method are active for the selective hydrogenation of citral into unsaturated alcohols.¹⁵²

Electroless Deposition. This method is similar to reductive deposition but uses a controlled chemical reaction, catalyzed by Pt, to deposit a metal salt onto an activated metal site of a preexisting monometallic catalyst. This method is used for the synthesis of Pt–Ag bimetallic catalysts.¹⁵³ A preprepared Pt catalyst is suspended in deionized water with a second metal source (AgNO_3), an ionic strength adjuster (NaNO_3), a reducing agent (HCHO), and NaOH or HNO_3 to adjust the solution pH. The mixture is stirred for 2 h while the pH is kept at 9 by small additions of NaOH or HNO_3 . After deposition, the slurry is filtered and washed to remove excess ions, then fully dried. Results indicate that Ag deposition is restricted to the Pt surface and does not readily occur on the catalyst support.¹⁵³ For hydrogenation of 3,4-epoxy-1-butene (EpB), the addition of Ag to a monometallic Pt catalyst increases the activity by ~ 3 times. The effect of Ag addition is not as pronounced on the catalyst prepared using impregnation, indicating that electroless deposition leads to targeted placement of Ag on the Pt surface.¹⁵³

Colloidal Synthesis. This method has the potential to synthesize supported catalysts with precise control over the size and composition of the bimetallic particles because the metallic colloid is prepared in the presence of a surfactant, which prevents the coalescence of small particles. The metallic colloid is prepared by making a solution of metal precursors, such as K_2PtCl_4 for Pt, in the presence of a cationic surfactant such as C_{14}TABr . For bimetallic synthesis, precursors of both metals are mixed with the surfactant. The interaction between the precursor metal anions and the surfactant cation in aqueous solution leads to the formation of an organic metal precursor. The reactants are then stirred vigorously and heated to 323 K upon addition of NaBH_4 , a reducing agent. After reaction, the metallic particles are precipitated and washed in decreasing

concentration of ethanol and increasing concentration of water until the particles are filtered and stored.¹⁵⁴ To prepare a supported catalyst, the metallic nanoparticles are added to the desired support in chloroform and sonicated for several hours. The suspension is centrifuged and washed with an acetone–ethanol mixture and then dried in an oven.¹⁵⁵ It is important to point out that the removal of carbon from the surfactants and colloids is critical for the utilization of these materials for catalytic applications. In particular, further studies are needed to identify procedures for carbon removal without changing the structure and surface morphology of the catalysts. Pt–Co catalysts prepared by this method and supported on mesoporous silica have been used for CO_2 hydrogenation into CO and CH_4 between 473 and 573 K.¹⁵⁵

Core–Shell Synthesis. Core–shell nanoparticle catalysts consist of a transition metal core covered with a 1–2 monolayer shell of another metal, such as Pt. The transition metal core is prepared by dissolving a metallic chloride precursor in ethylene glycol with polyvinyl alcohol as a surfactant, while holding the solution under nitrogen. The solution is heated and the metal precursor is reduced by dropwise addition of NaBH_4 . After reaction, the colloid is quenched on ice, centrifuged in an acetone–ethanol mixture, and then dispersed in ethylene glycol.¹⁵⁶ To form the Pt shells, PtCl_2 is dissolved in ethylene glycol at room temperature. With a syringe, a small amount of the metallic nanoparticle suspension is added to the PtCl_2 solution. The mixture is often heated and held at elevated temperatures before quenching in an ice bath. The supported catalysts are formed by adding an oxide support to the colloidal suspension and drying the slurries in vacuum. Pt@Ru core–shell nanoparticles synthesized with this method were shown to be more active than their constituent pure metal nanoparticles, as well as their nanoalloys synthesized from conventional methods for CO oxidation in hydrogen.¹⁵⁶

For core–shell systems, it is also desirable to synthesize catalysts with a low-cost transition metal core and Pt or other precious metals at the outermost layer. Mayrhofer et al. have found that, in PtCo@Pt core–shell nanoparticles, Pt segregates to the surface under a CO environment.¹⁵⁷ Another study with a M@Pt ($\text{M} = \text{Ni}, \text{Co}$) system shows high activity for hydrolysis of ammonia borane (NH_3BH_3).¹⁵⁸ Fe@Pt NPs supported on carbon have also been used for NH_3BH_3 oxidation. These catalysts are low cost, highly stable, and much more active than the commercial Pt/C catalysts used for NH_3BH_3 oxidation.¹⁵⁹

Reverse Micelle Synthesis. This method uses microemulsions to produce supported metallic nanoparticles with a narrow size distribution. The microemulsion is formed by dissolving a small amount of a metal precursor in an aqueous environment inside of a nonionic surfactant. Upon addition of a reducing agent, such as hydrazine (N_2H_4), the metal precursors are chemically reduced, leaving nanosized metallic particles.¹⁶⁰ Synthesis of supported catalysts begins by mixing an aqueous solution with the metal precursor and surfactant with an oil-phase solution of the reducing agent. Under stirring, the solution becomes clear, indicating the formation of reverse micelles. A metal oxide support is added as the solution is titrated with acetone to disrupt the micelles, leading to the adsorption of micelles to the support.¹⁶¹ Reverse micelle synthesis is a useful technique because the size of the metallic nanoparticles can be directly controlled by the ratio of water to surfactant. The amount of reducing agent can also influence the

size of particles by increasing the nucleation rate and, thus, decreasing the particle size.¹⁶⁰ Pt–Ni/ γ -Al₂O₃ catalysts synthesized using this method exhibit increased activity over their parent metals for 1,3-butadiene hydrogenation due to an enhanced bimetallic effect.¹⁶²

Dendrimer Support Synthesis. Synthesis of metallic nanoparticles with dendrimer supports yields monodisperse particles with a diameter of 1–2 nm. This synthesis method overcomes the weakness of traditional impregnation techniques, which tend to make nanoparticles with wide size distributions.¹⁶³ Dendrimer-encapsulated nanoparticles (DENs) are synthesized by extracting metal ions into the interior of dendrimers and then chemically reducing the metal ions to form monodisperse particles that are <3 nm in diameter.¹⁶⁴ DENs are prepared by adding a low concentration of K₂PtCl₄, or another metallic precursor, to an aqueous solution of hydroxyl-terminated dendrimers. The generation (size) of the dendrimers can be used to directly control the size of the metallic nanoparticles. After adding the metal precursor to the dendrimer solution and stirring for 3 days, the solution is purged with N₂ and then chemically reduced with NaBH₄ overnight. The metallic nanoparticles are removed by dialysis and then filtered.¹⁶⁵ Once the solution of metallic nanoparticles is obtained, the particles can be deposited on a support by impregnation. Catalysts synthesized with dendrimer supports have been tested in several catalytic applications including hydrogenation¹⁶⁴ and CO oxidation.¹⁶³

Other Synthesis Methods. Several other synthesis techniques have been employed to synthesize supported catalysts. Microwave-assisted polyol reduction (MAPR) allows very rapid uniform heating of the metal precursors to a high temperature within a few seconds. This shortens the crystallization period of the metal nanoparticles, leading to more homogeneous nucleation when compared to traditional synthesis methods. In MAPR synthesis, the support is immersed in an aqueous metal precursor solution and then dried in vacuum.¹⁶⁶ The MAPR method can be applied to bimetallic catalysts by adding a second metal precursor to the aqueous solution. Pt-based bimetallic catalysts have been successfully synthesized using the MAPR method with high activity and selectivity for cinnamaldehyde hydrogenation, with the MAPR catalysts outperforming catalysts synthesized by the conventional impregnation method.¹⁶⁶

Another interesting approach is to directly deposit metal on an oxide support on the reactor wall. The reactor consists of an Fe–Cr–Al cylinder placed in a stainless steel tube, which is heated to high temperatures to produce a γ -Al₂O₃ film on the surface of the cylinder.¹⁶⁷ To prepare the supported catalyst, the Fe–Cr–Al alloy cylinder is dipped into a slurry of metallic precursors until the desired loading is reached, followed by drying and calcining the alloy cylinder.¹⁶⁷ The advantage of this synthesis process is that the catalyst is formed directly on the walls of the reactor, allowing for high loading and potentially uniform catalyst deposition. This approach has been used for preferential oxidation of carbon monoxide in hydrogen-rich gas streams, leading to a reduction of CO in the feed from 1% to <10 ppm.¹⁶⁷

Finally, laser vaporization has been used to synthesize monometallic and bimetallic catalysts of approximately the same size, morphology, and composition. In the laser-vaporization technique, a low-energy Nd:YAG pulsed laser vaporizes a metal of interest from a rod to create a plasma. Crystal growth begins by introducing a continuous flow of He

or Ar into the evaporation chamber, leading to the deposition of metal clusters onto the catalyst support. These clusters are highly uniform in size and composition as they are fully formed before they are deposited onto the support.¹⁶⁸ Although the quantity of the catalysts produced in this method is relatively small, these samples offer the opportunity for obtaining fundamental correlations between catalytic properties and the size, shape, and composition of bimetallic catalysts. Pt–Pd/ γ -Al₂O₃ catalysts prepared by laser vaporization show similar trends as catalysts prepared by traditional methods for toluene hydrogenation.¹⁶⁸

2.2.2. Common Characterization Techniques for Bimetallic Catalysts. *CO and H₂ Chemisorption.* One of the most important parameters of bimetallic catalysts is the number of active metal sites, which is typically obtained using CO chemisorption. The CO uptake can be measured using many specialized instruments, but as an example, an AMI-200ip (Altamira Instruments) is a viable option. Measurements are performed by loading a known quantity of calcined catalyst into a quartz tube, which is then inserted into the instrument. Catalysts are reduced with a desired H₂-containing gas mixture at a specified temperature and then are cooled to room temperature. After cooling, CO is pulsed over the catalyst, and the amount of effluent CO is measured using a thermal conductivity detector (TCD). For proper comparison of catalytic activity among different catalysts, the reaction rates must be normalized by the values of CO uptake on each catalyst. CO chemisorption can also be used to estimate metal dispersion by assuming the stoichiometry of M/CO = 1:1 (M = Pt, Ni, Pd, etc.), although the 1:1 ratio is clearly an oversimplification. The dissociative adsorption of H₂ is also used to determine the number of active metal sites. However, care must be taken because hydrogen starts to desorb from some bimetallic surfaces at room temperature.

Elemental Analysis. Two techniques are commonly used to quantify the concentrations of elements in supported bimetallic catalysts. Atomic absorption spectroscopy (AAS) is a quantitative technique used to measure the absorption of light by free atoms in the gaseous state. In a typical AAS experiment, an analyte solution is prepared by dissolving a supported catalyst, which is then made into an aerosol with a nebulizer and atomized using an air–acetylene flame. The concentration of metallic ions in the solution is obtained after normalizing the AAS intensity with reference compounds.¹⁶⁹ Another technique, inductively coupled plasma atomic/optical emission spectroscopy (ICP-AES/OES), is also used to quantify the concentration of trace metals within a bimetallic catalyst.¹⁷⁰ In principle, ICP-AES/OES should have a higher detection limit than AAS for most metals, although it is a more sophisticated and expensive instrument than AAS.

Temperature-Programmed Reduction and Oxidation. Temperature-programmed reduction (TPR) is used to measure the temperatures at which metals and/or supports are reduced in a catalyst. After calcination, a catalyst is placed in a reactor under flowing H₂ and heated at a constant ramp rate. As the temperature increases, the catalyst is reduced by the H₂ and oxygen is removed from the catalyst in the form of water. With a TCD connected to the effluent stream, the change in concentration of water can be measured to determine the reduction temperature(s). The TPR measurements provide information on the optimal reduction temperature for a catalyst, as well as whether the presence of Pt reduces the reduction temperature of bimetallic catalysts. Temperature-

programmed oxidation (TPO) is similar in theory to TPR, but it is used to measure the amount of coke deposited on the surface of a catalyst. In TPO measurements, a spent catalyst is placed in a reactor under flowing O_2 and heated at a constant rate. As the temperature increases, the coke on the surface of the catalyst is oxidized by O_2 and the carbon is removed from the catalyst in the form of CO_2 . Using a TCD to monitor the composition of the effluent stream, the area of the CO_2 intensity versus temperature curve can be measured to determine the amount of surface carbon. This technique can also be used to determine the strength of interaction between the surface carbon and the supported catalyst because a higher oxidation temperature indicates the coke is more difficult to remove. A related technique, thermogravimetric analysis/differential thermal analysis (TGA/DTA), is also used sometimes to determine the amount of surface carbon through precise weight measurements during TPO of spent catalysts.^{171,172}

Temperature-Programmed Desorption. Temperature-programmed desorption (TPD) is used to determine the binding energy of adsorbates on catalysts. In TPD experiments a catalyst is loaded into a reactor fitted with a mass spectrometer. The catalyst can be pretreated under reduction conditions or used in the calcined form. After pretreatment, the catalyst is treated with an adsorbate, which is usually a reactant of interest. The excess adsorbate that is not strongly bound to the catalyst is removed by flowing He. The catalyst is heated linearly at a constant rate,¹³⁹ and the effluent products are monitored using a mass spectrometer. By plotting the evolution of the adsorbate and its derivatives versus temperature, information can be inferred regarding reaction sites and binding energies of the adsorbate.

Transmission Electron Microscopy and Scanning Electron Microscopy. Transmission electron microscopy (TEM) and scanning electron microscopy (SEM) are two primary forms of electron microscopy to characterize the morphology of catalysts. TEM uses transmission of a high-energy electron beam (~ 200 keV) through a thin sample to produce an image, whereas SEM rasters a high-energy electron beam (1–40 keV) across the surface of a sample. In TEM, two primary imaging modes are used to investigate particle size and morphology of catalysts. Imaging can be performed in either bright field (BF) or dark field (DF) modes by selecting the direct beam (transmitted through the sample) or diffracted beam (diffracted off of the sample), respectively. BF imaging is used mainly to view catalyst morphology because the contrast between the metal and the support is too low to accurately quantify metallic particle sizes on supported catalysts. DF imaging has much more utility for viewing high atomic number (Z) transition metals supported on low-Z metal oxides. When combined with scanning transmission electron microscopy (STEM), catalysts can be imaged with very high Z-contrast in high-angle annular dark field (HAADF) imaging. In HAADF imaging, the STEM probe is a focused beam that is rastered across an area of the sample. As the atomic number of the element increases, the scattering angle of the electrons also increases. Therefore, HAADF imaging easily distinguishes between different elements by Z-contrast to create a high-contrast image.¹⁷³ Unlike TEM, electrons in SEM are not transmitted through the sample. The most common mode of image capture in SEM is by secondary electrons. An image constructed with secondary electrons contains rich topographic information and has a 3D appearance. SEM is particularly useful for characterizing the

morphology and topography of catalyst surfaces. Because the morphology of the catalysts often changes under reaction conditions, further development and applications of environmental TEM and SEM should provide additional means for catalyst characterization.

Recently, there have been advances to correct intrinsic imperfections in the lenses of electron microscopes to improve resolution at very high magnification. These microscopes contain additional lenses to correct for spherical and chromatic aberrations. Spherical aberration corrected TEM (C_s -TEM) is capable of distinguishing features up to ~ 0.1 nm for the viewing of individual metal atoms. This technique has been used recently to correlate strain effects in Pt–Fe@Pt nanoparticles to activity in the oxygen reduction reaction.¹⁷⁴ In addition to increasing the resolution of TEM, advances have been made in performing TEM under in situ conditions, referred to as environmental TEM (E-TEM). E-TEM has been used to study the behavior of Cu/CeO₂ catalysts under reduction and oxidation conditions for several reactions including the water gas shift reaction, methanol synthesis, and methanol reforming.¹⁷⁵

The chemical composition of a catalyst can be measured using energy-dispersive X-ray spectroscopy (EDS) in both TEM and SEM. EDS relies on the principle of X-ray fluorescence to collect compositional data in specific areas of the sample. A fluorescent X-ray is created from atoms that are ionized by the incident electron beam.¹⁷⁶ The fluorescent X-ray has a characteristic energy that is equal to the difference of energy of the outer-shell and inner-shell electrons for a specific element. The peak intensities in EDS measurements can be used to estimate the elemental compositions of the sampled area after proper normalization.

Infrared Spectroscopy. Infrared (IR) spectroscopy is a very useful technique to determine the bonding configuration of reaction intermediates adsorbed on catalysts, as well as to measure the concentrations of reactants and products in the gas or aqueous phase. Several types of IR spectroscopy are used in catalytic research. The most common one is Fourier transform infrared (FTIR) spectroscopy,^{177,178} which is used to measure the transmission of infrared radiation through a catalyst pellet or reaction environment. The IR cell is a gas-phase batch reactor that allows the heating and in situ reduction of the catalyst pellet. The rate constant and product distribution can be obtained by measuring gas-phase FTIR as a function of reaction time. In addition, FTIR measurements are often useful in determining the surface termination of bimetallic particles by measuring the vibrational frequencies of adsorbed carbon monoxide (CO). Because the frequencies of adsorbed CO are distinct for different transition metals, a comparison of FTIR spectra between the bimetallic and monometallic catalysts reveals which metals occupy the topmost surfaces of the bimetallic particles. As will be demonstrated later, the surface termination of bimetallic catalysts plays a critical role in the catalytic performance. Two other types of IR spectroscopy are also used in catalyst characterization. Attenuated total reflectance infrared (ATR-IR) measures the attenuation of total internal reflection of the reflected light¹⁷⁹ and is better suited for aqueous-phase environments. Diffuse reflectance infrared Fourier transform spectroscopy (DRIFTS) measures the reflection of the IR light from the catalyst, making it more surface-sensitive than transmission FTIR. In addition, a related optical technique, ultraviolet–visible diffuse reflectance spectroscopy (UV–vis DRS), is a surface-sensitive spectroscopy

that is identical in theory to DRIFTS but uses wavelengths of light in the UV–vis range instead of in the IR range. The higher-energy radiation allows UV–vis DRS to probe the band gap of metals to obtain information regarding the oxidation state.¹⁸⁰

X-ray Absorption Spectroscopy. X-ray absorption spectroscopy (XAS) is a synchrotron-based technique used to characterize the local atomic and electronic structures^{181,182} of a catalyst under in situ conditions relevant to catalytic reactions. XAS measurements are performed by using a monochromatic X-ray beam and collecting the absorption coefficient, μ , as a function of X-ray energy. When the incident energy ($h\nu$) approaches the binding energy E_0 of a core level electron, a sharp jump in μ is observed, known as the absorption edge. The region of the scan that begins before the absorption edge and ranges to 50–100 eV above the edge is known as the X-ray absorption near-edge structure (XANES) region.^{183,184} The region beginning at 50–100 eV above the edge (after the XANES region) and extending up to 1000 eV past the edge is known as the extended X-ray absorption fine structure (EXAFS) region.¹⁸³ A critical feature in the XANES region is the “white line”, caused by a rapid increase in absorption. This feature is present in L-edges, due to the excitation of an electron from the p-orbitals into the higher energy, unoccupied d-states.¹⁸⁵ The main utility of the white line is to characterize the oxidation state of a metal during and after H_2 treatment, as well as during catalytic reactions. For example, a reduction in the white line intensity after treatment in H_2 indicates that the metal of interest is being reduced. With further analysis of the XANES region, information regarding coordination number can also be calculated.^{181,182}

The EXAFS region contains fine-structure information regarding the local coordination environment. The critical difference between the EXAFS and XANES regions is that in the EXAFS region the ejected photoelectron has sufficient energy to scatter from each of the surrounding atoms and then backscatter to the absorbing atom.¹⁸¹ Because the ejected photoelectron has wave-particle duality, the outgoing and backscattered electrons can constructively or destructively interfere with each other, making it possible to derive information about the local coordination environment of the catalyst particle. For example, the intensity of the oscillations increases with increasing coordination number, while the frequency of oscillations is inversely dependent on interatomic distances.¹⁸² Quantitative structural information can be obtained after data reduction and mathematical analysis of the EXAFS function, as described elsewhere.^{183,186,187} Quantitative analysis of EXAFS results are obtained by fitting the reduced data to phases and backscattering amplitudes constructed either from reference compounds or calculations using simulation software such as FEFF.^{187–189}

Additional information can be obtained by combining XAS with other techniques for in situ, time-resolved measurements. For example, combined XAS and XRD measurements are applied for investigations of catalysts under reaction conditions.¹⁹⁰ Several authors have further enhanced the combined measurements by adding complementary electronic and vibrational spectroscopy techniques, including ultraviolet-visible (UV–vis), infrared, and Raman, to the well-established XAS–XRD combination.^{191,192} Weckhuysen and others have combined the small- and wide-angle scattering (SAXS and WAXS) techniques with quick-scanning XAS to study in situ

processes.¹⁹³ More details about some of these advances can be found in a recent review by Bentrup.¹⁹⁴

2.2.3. Example: Characterization of Supported Pt–Ni Bimetallic Catalysts. Supported Pt–Ni bimetallic catalysts have been synthesized using various synthesis methods and characterized with many of the techniques described previously. For example, Figure 5 shows the proposed bimetallic particle in

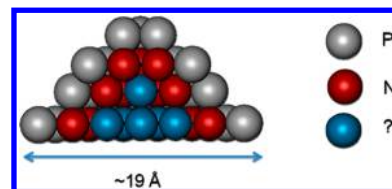


Figure 5. Proposed structure of a supported Pt–Ni bimetallic particle derived from TEM, FTIR, and EXAFS characterization.

Pt–Ni/ γ - Al_2O_3 after in situ reduction in H_2 .¹⁴³ The particle size was determined from a combination of TEM and CO chemisorption analysis. The Pt-termination of the catalyst particle was derived by comparing the vibrational frequencies of adsorbed CO on Pt–Ni/ γ - Al_2O_3 and the corresponding monometallic catalysts. The presence of fully reduced, metallic Pt and Ni was confirmed following the reduction of white line intensities in XANES during H_2 reduction. The intimate contact between Pt and Ni atoms was verified by the detection of the Pt–Ni nearest neighbor in the EXAFS measurements. Overall, the Pt-terminated bimetallic particle in Figure 5 is similar to the subsurface Pt–Ni–Pt(111) structure in Figure 3, responsible for the strong correlation between model surfaces and supported catalysts for hydrogenation reactions, as discussed later.

3. STABILITY OF PT-BASED BIMETALLIC SURFACES WITH DIFFERENT ADSORBATES

3.1. DFT Calculations of Thermodynamic Stability

One of the most critical questions in bimetallic catalysis is the stability of bimetallic surface structures under reaction conditions, which would in turn modify the catalytic properties. For example, as shown earlier in Figure 3, the monolayer surface Ni atoms diffuse into the subsurface region of Pt(111) upon annealing, indicating that the subsurface Pt–Ni–Pt(111) structure is thermodynamically more stable than the surface Ni–Pt–Pt(111) structure in vacuum, i.e., without adsorbates. Several other investigations of Pt–3d alloys in fuel cell applications have suggested that the alloy films used in these studies are covered by a Pt skin,^{195–197} again indicating the thermodynamic preference of Pt-terminated bimetallic surfaces.

Ruban et al.¹⁹⁸ have utilized DFT to calculate the segregation energy (E_{seg}) for transition metal alloys, which is the thermodynamic driving potential to move the subsurface admetal from the bulk to the surface of the host metal in vacuum. Alden et al.¹⁹⁹ have shown that the surface segregation energy in transition metal alloy depends strongly on the crystal structure and is essentially given by the difference in the surface energies of the pure alloy components. Ruban et al.¹⁹⁸ have performed DFT calculations of the values of E_{seg} for admetal atoms (M) on many host substrates (H), utilizing the linear-muffin-tin-orbitals coherent potential approximation. If E_{seg} is sufficiently negative, the admetal segregates to the surface to produce the M–H–H surface monolayer structure. If E_{seg} is

sufficiently positive, the surface layer is the host metal, leading to the formation of the H–M–H subsurface monolayer structure. Christensen et al.⁴³ have also utilized DFT to investigate surface alloy phases and their stability based on surface phase diagrams constructed from the surface energy as a function of the surface composition.

Greeley and Mavrikakis¹² performed segregation energy calculations by examining the effects of adsorbates on the stability of the surface and subsurface structures. It was found that the thermodynamic driving force of hydrogen-induced segregation was related to two terms: the value of E_{seg} and the difference between the hydrogen-binding energies on the surface and subsurface structures. Because hydrogen binds relatively weakly to most transition metals, only a few bimetallic surfaces experience a hydrogen-induced segregation of the subsurface admetals.

Besides hydrogen, it is also important to study the influence of adsorbates on surface segregation using a strong adsorbate, such as oxygen. Figure 6 shows the total energy difference,

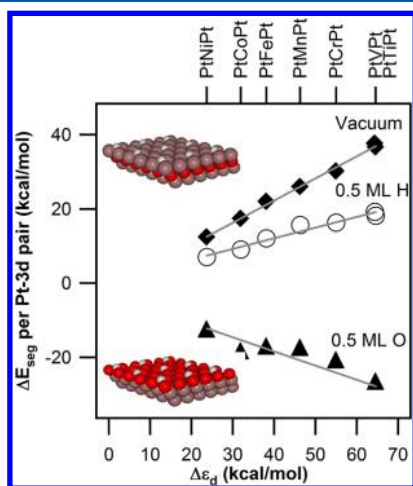


Figure 6. DFT calculations of thermodynamic stability of 3d/Pt(111) surfaces in vacuum and with 0.5 ML of atomic hydrogen and oxygen. Positive ΔE_{seg} values indicate that the subsurface Pt–3d–Pt(111) structures are thermodynamically stable.^{33,200}

ΔE_{seg} , defined as the difference between the formation energy of the subsurface and surface structures, as a function of the surface d-band center in the 3d–Pt–Pt(111) structure. The values of ΔE_{seg} are positive for all systems under vacuum, predicting that the Pt–3d–Pt(111) subsurface structures are thermodynamically more stable than the 3d–Pt–Pt(111) surface in vacuum. For comparison, the ΔE_{seg} values are also included in Figure 6 with 0.5 ML atomic hydrogen and oxygen.³³ The DFT results predict that the subsurface configuration remains thermodynamically preferred with adsorbed hydrogen. However, the subsurface structure is no longer stable in the presence of 0.5 ML atomic oxygen, indicating a thermodynamic driving potential for the subsurface 3d metals to segregate to the surface. Additional atomic adsorbates are studied by Menning and Chen²⁰⁰ to compare how the thermodynamic potential for segregation varies with adsorbate binding strength. An adsorbate with a weak Pauling electronegativity, such as H, S, Se, or C, binds weakly with both surface and subsurface configurations and provides only a small shift in the thermodynamic potential for interchanging the configuration. In contrast, an adsorbate with a strong Pauling

electronegativity, such as N or O, produces a large difference in binding energy between the two configurations. When the surface coverage of N or O is high enough, this difference outweighs the thermodynamic potential for retaining the subsurface configuration in vacuum.²⁰⁰

The results in Figure 6 indicate that the presence of atomic oxygen makes the 3d–Pt–Pt(111) surface structure more thermodynamically stable than Pt–3d–Pt(111). Menning and Chen have extended DFT calculations to the Pt(100) substrate to explore the effect of crystal structure on segregation. Although the values of the d-band center and ΔE_{seg} are different for 3d metals on Pt(111) and Pt(100), the general trend in the relative stability of the surface and subsurface structures remains the same.³³ The oxygen-induced surface segregation is also predicted for the (211) surfaces of Pt(shell)/M(core) and Pt₃M (M = Co, Ir) alloys by Callejas-Tovar and Balbuena.²⁰¹ Table 2 provides a list of DFT calculations and experimental studies of surface segregation of various bimetallic surfaces with several types of atomic and molecular adsorbates.

3.2. Experimental Verification of Surface Segregation

DFT results predict that the surface 3d–Pt–Pt(111) configuration is thermodynamically preferred with adsorbed oxygen. Parallel experimental measurements have been performed to verify the predicted segregation of subsurface 3d atoms in the presence of oxygen, as well as to quantify the activation barrier for the adsorbate-induced segregation. To verify the oxygen-induced segregation, high-resolution electron energy loss spectroscopy (HREELS) has been utilized to monitor the segregation of Ni and Co in the Pt–3d–Pt(111) subsurface configurations when exposed to oxygen.⁶⁴ The onset of the characteristic $\nu(\text{Ni–O})$ and $\nu(\text{Co–O})$ vibrational modes confirms the segregation of subsurface Ni and Co after exposing the subsurface Pt–3d–Pt(111) configuration to oxygen at different temperatures. In addition, AES measurements were performed to quantify the segregation kinetics. The AES intensity ratios of Co/Pt or Ni/Pt were used to monitor the interchange between the subsurface and surface structures after exposure to oxygen. Figure 7a shows that the normalized AES Ni/Pt ratio increases after exposing subsurface Pt–Ni–Pt(111) to increasing amounts of oxygen at various temperatures. The increase in the Ni/Pt AES ratio with higher oxygen exposures confirmed the oxygen-induced segregation of subsurface Ni atoms. Using an Arrhenius equation to analyze the data, such as that shown in Figure 7b, the activation barrier for the oxygen-induced segregation of Co and Ni is estimated to be 7 ± 1 and 15 ± 2 kcal/mol, respectively. This follows the trend predicted by DFT (Figure 6), where Ni is predicted to have the smaller driving potential for segregation compared to Co and should correspondingly have a higher activation barrier.

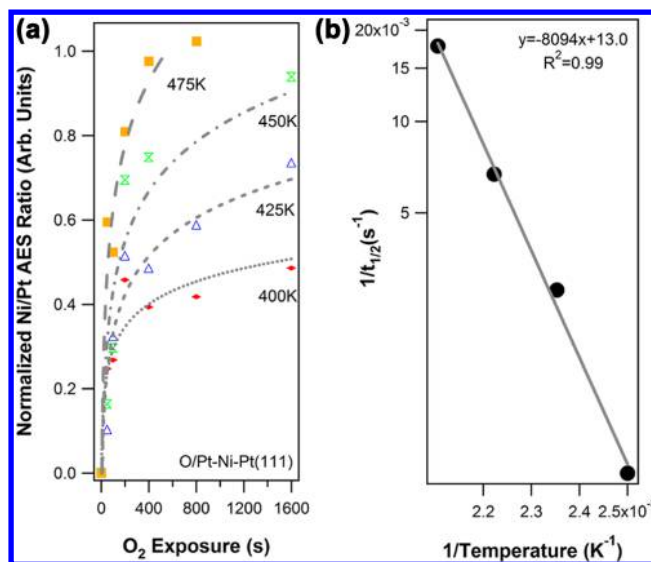
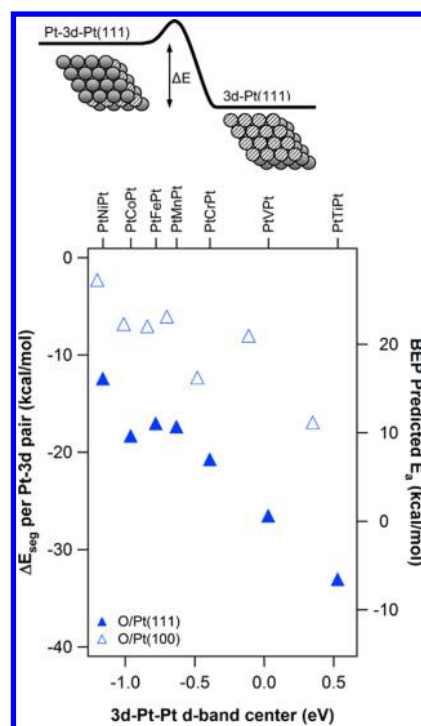
To capture the effect of the crystal facet on segregation, oxygen-induced segregation of subsurface Co and Ni has also been studied on polycrystalline Pt foil composed of nearly equal amounts of the two main crystal facets for fcc, (111) and (100).³³ Using a similar Arrhenius analysis procedure, an activation barrier is estimated to be 27 ± 1 kcal/mol for the segregation of subsurface Ni from the Pt(100) facet of the Pt foil, higher than the value of 15 ± 2 kcal/mol from Pt(111). This trend is consistent with the DFT prediction that the subsurface Pt–Ni–Pt configuration should be more stable on the (100) crystal facet than the (111) facet.³³

Experiments such as those shown in Figure 7 are extremely time-consuming to perform. Through the use of combined

Table 2. List of Studies of Surface Segregation with Different Adsorbates

adsorbate	surface	techniques
O	3d/Pt(111), 3d/Pt(100)	DFT ³³
O ₂	3d/Pt(111), 3d/Pt(100)	AES ³³
H, O, C, N, S, and Se	3d/Pt(111)	DFT ²⁰⁰
vacuum, H, O	3d/Pt(111), 3d/Pt(100)	DFT ²⁰²
O ₂	3d/Pt	HREELS, ²⁰² AES ²⁰²
vacuum	Ni/Pt(111)	MD, ²⁰³ DFT, ²⁰³ AES ²⁰³
vacuum	Re ₃ Pt polycrystalline	DFT, ²⁰⁴ XPS, ²⁰⁴ UPS ²⁰⁴
O	Pt ₃ Ti(111)	DFT, ²⁰⁵ MC ²⁰⁵
O, OH	Pt ₂ IrCo(111), Pt ₂ IrCr(111)	DFT ²⁰⁶
H ₂ , O ₂	Fe/Pt(111)	STM, ²⁰⁷ XPS ²⁰⁷
CO, O ₂	Fe/Pt(111)	DFT, ²⁰⁸ STM, ²⁰⁸ XPS, ²⁰⁸ HREELS ²⁰⁸
H ₂ , O ₂	Pt–Ni nanoparticles	XPS, ²⁰⁹ HRTEM ²⁰⁹
H ₂ , O ₂	Pt–Cu nanoparticles	XPS ²⁰⁹
H ₂ , O ₂	Pt–Co nanoparticles	XPS ²⁰⁹
CO	Cu/Pt, Ag/Pt	DFT, ²¹⁰ TPD, ²¹⁰ XPS, ²¹⁰ ISS, ²¹⁰ LEED, ²¹⁰ PM-IRAS ²¹⁰
O	Pt ₃ M (M=Fe, Co, Ni)	DFT ^{211,212}
vacuum	Pt ₃ M (M = Ag, Au, Co, Cr, Cu, Fe, Ir, Mn, Mo, Ni, Pd, Re, Rh, Ru, Ti, V)	DFT ²¹³
vacuum	Co/Pt(111), Au/Pt(111)	DFT ²¹⁴
O	Pt/Ir(core) and Pt ₃ Ir(211)	DFT ²⁰¹
O	Pt/Co(core) and Pt ₃ Co(211)	DFT ²⁰¹
O	Pt/Fe(001)	DFT ²¹⁵
H	Ti/Pt(111)	DFT ²¹⁶
vacuum	Pt/Pd(111), Pt/Pd(100), Pt/Pd(110)	MC ²¹⁷
H ₂ , O ₂	Pt–Ni nanoparticles	XPS, ²¹⁸ STM, ²¹⁸ XRD, ²¹⁸ XANES ²¹⁸
vacuum	Pt ₃ Ni(111)/M (M = V, Fe, Co, Mo, Tc, Ru, W, Re, Os, and Ir)	DFT ²¹⁹
H ₂ , O ₂	Pt/3d	DFT ²²⁰
OOH, OH and O	Pt/Pd	DFT ²²¹
vacuum	PtRu/Ru(0001)	STM, ²²² AES ²²²
CO, D ₂	PtRu/Ru(0001)	TPD, ²²³ IR ²²³
O	Pt ₂ Mo	DFT, ²²⁴
CO	Pt–Au/TiO ₂ (110)	STM, ²²⁵ LEIS, ²²⁵ TPD ²²⁵

theory and experiments, an estimation for the activation barriers of other Pt–3d–Pt systems can be achieved using a Brønsted–Evans–Polanyi (BEP) relationship.³³ The constants in the BEP relationship have been derived from the activation barriers for the Pt–Ni–Pt(111), Pt–Ni–Pt(100), and Pt–Co–Pt(111) surfaces. The results from this prediction are shown in Figure 8, where the left axis is the segregation energy and the right axis is scaled to show the corresponding BEP activation barrier for oxygen-induced segregation. All of the Pt–3d–Pt(100) structures are predicted to have a higher activation barrier for oxygen-induced segregation compared to the respective Pt–3d–Pt(111) configuration. Among Pt–3d bimetallic surfaces, the Pt–Ni–Pt system is predicted to be the most resistant to oxygen-induced segregation, having the highest activation barriers for the (111) and (100) crystal facets. At the other extreme, the Pt–Ti–Pt surface is predicted to be the most susceptible to oxygen-induced segregation,

**Figure 7.** (a) Normalized Ni/Pt Auger ratio as a function of oxygen exposure at various temperatures and (b) Arrhenius analysis of the activation barrier from Pt–Ni–Pt(111) to Ni–Pt–Pt(111) in oxygen environment.⁶⁴**Figure 8.** Left axis shows the DFT-predicted potential energy difference for segregation of Pt–3d systems with 0.5 ML O, and the right axis shows activation barriers derived using a Brønsted–Evans–Polanyi relationship.³³

having the lowest (100) activation barrier and an unactivated process on the (111) crystal facet.

In addition to segregation experiments performed under UHV conditions, the segregation of subsurface Co and Ni was also verified under ambient pressure using XANES²²⁶ under in situ conditions. Using a polycrystalline Pt foil as the substrate, the Co and Ni atoms were found to undergo inward diffusion upon exposure to H₂ and surface segregation after exposure to O₂. These experimental observations further confirm the DFT

prediction (Figure 6) that the Pt-terminated subsurface structure is stable with adsorbed hydrogen while the 3d-terminated surface structure is preferred with adsorbed oxygen.

Furthermore, such reversible behavior is extended to bimetallic nanoparticles. Mu et al.²⁰⁹ have observed the reversible structural changes at the surfaces of supported Pt–Ni nanoparticles treated in alternating O₂ and H₂ atmospheres. Figure 9 shows the XPS Ni2p intensity ratio, which oscillates

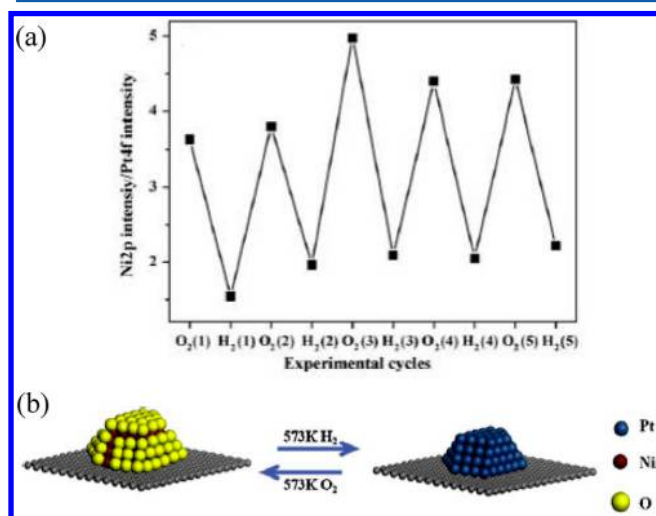


Figure 9. (a) Dependence of the ratio of XPS Ni2p intensity to XPS Pt 4f intensity and (b) reversible change in surface structure of Pt–Ni transition metal nanoparticles with the oxidation and reduction cycles.²⁰⁹ Reproduced with permission from ref 209. Copyright 2009 Elsevier.

with the oxidation–reduction cycles. The XPS results indicate that the Pt–Ni nanoparticles surface is NiO-rich in oxidizing gases and Pt-terminated in reducing gases, consistent with the DFT predictions in Figure 6. Overall, the strong correlation between DFT prediction and experimental measurements, on both model surfaces and nanoparticles, provides conclusive evidence that the bimetallic structures change under different reaction environments. Such structural changes in turn modify the catalytic performance of bimetallic catalysts for different types of reactions, such as hydrogenation and oxidation reactions, as discussed in the next section.

4. UTILIZATION OF PT-BASED BIMETALLIC CATALYSTS IN CATALYTIC REACTIONS

In this section we divide the catalytic reactions into several categories: hydrogenation, dehydrogenation, reforming, and oxidation reactions. Table 3 summarizes selected UHV studies of the adsorption and reaction of different molecules on model bimetallic surfaces. Tables summarizing reactor studies over supported bimetallic catalysts based on the types of reactions are provided in the corresponding subsections. The main focus of the review is to identify general trends on how bimetallic catalysts enhance the activity and selectivity for each type of reaction. Special attention is paid to correlate model surfaces with supported catalysts whenever possible.

4.1. Hydrogenation Reactions

Catalytic hydrogenations are among the most commonly practiced catalytic processes, ranging from common steps in organic synthesis to batch processes in pharmaceutical production, to stabilization of edible oils, and to petroleum

upgrading processes. Because hydrogenation reactions are typically exothermic, it is advantageous to carry out these reactions at low temperatures. In the current section we will first use the hydrogenation of cyclohexene to demonstrate the feasibility of increasing the low-temperature hydrogenation activity by reducing the binding energies of atomic hydrogen and cyclohexene, which can be achieved by designing bimetallic surfaces with specific surface structures. We will then discuss hydrogenation reactions of C=C, C=O, and N=O bonds to further illustrate the advantages of bimetallic catalysts in terms of both hydrogenation activity and selectivity. Hydrogenation studies under UHV conditions are summarized in Table 3; selected reactor studies of hydrogenation reactions over supported bimetallic catalysts are listed in Table 4

4.1.1. C=C Hydrogenation. **4.1.1.1. Example: Cyclohexene Hydrogenation on Pt–3d Catalysts.** Cyclohexene is used as a probe molecule to study hydrogenation because cyclic hydrocarbons are important reaction intermediates in many refinery and petrochemical processes, in addition to serving as building blocks for many chemicals produced in the chemical industry. Furthermore, cyclohexene has several competitive reaction pathways, including decomposition, dehydrogenation, disproportionation (self-hydrogenation), and hydrogenation. Comparative studies of these reaction pathways provide an opportunity to determine how the formation of bimetallic bonds affects the hydrogenation activity and selectivity.

DFT and UHV Studies on Single-Crystal 3d/Pt(111) Surfaces. To facilitate the low-temperature hydrogenation of cyclohexene, one hypothesis is that an effective catalyst should bond relatively weakly to atomic hydrogen and cyclohexene. Hammer and Nørskov³⁰² have shown that the binding strength of molecules on transition metals is dependent on the electronic structure of the surface, by using the surface d-band center with respect to the Fermi level to describe the surface electronic property. Chen et al.¹⁰ have summarized experimental and theoretical studies that identify a nearly linear relationship between the binding energies and the surface d-band center for many adsorbates on a wide range of bimetallic surfaces.

DFT calculations were performed to estimate the values of hydrogen-binding energy (HBE) on several 3d–Pt–Pt(111) and Pt–3d–Pt(111) surfaces. As shown in Figure 10a,²⁷ HBE is related to the position of the surface d-band center with respect to the Fermi level, in agreement with the trend observed in previous studies for other surfaces.¹⁰ In general, the addition of a 3d metal surface layer on Pt(111) moves the d-band center closer to the Fermi level compared to that of the bulk 3d metals. This is primarily due to the tensile strain induced by the Pt lattice because the ligand effect is weakest between late transition metal overlayers and the Pt(111) substrate.¹⁶ Conversely, the presence of subsurface 3d metals shifts the surface d-band center of Pt away from the Fermi level as compared to that of Pt(111), mainly due to the electronic interaction of Pt and the subsurface 3d atoms.¹⁶ The comparison in Figure 10a demonstrates that HBE typically follows the trend of 3d–Pt–Pt(111) > Pt(111) > Pt–3d–Pt(111). In addition, the nearly linear correlation between HBE and the surface d-band center should enable one to predict HBE on other bimetallic catalysts based on the extensive database of d-band center values for many bimetallic surfaces.

The binding energies of unsaturated hydrocarbons, such as cyclohexene, typically follow the same trend as HBE. As shown in Figure 10b, DFT calculations reveal that the Pt–3d–Pt(111)

Table 3. Summary of Selected Surface Science Studies of the Adsorption and Reaction of Molecules on Various Pt-Based Bimetallic Surfaces

surface	molecule	technique	surface	molecule	technique
hydrogenation			dehydrogenation		
Co/Pt(111)	acrolein	TPD ¹⁷	Sn/Pt(111)	1-hexene	TPD ²⁴⁹
Ni/Pt(111)	acrolein	TPD ¹⁷	Sn/Pt(111)	<i>n</i> -hexane	TPD ²⁴⁹
Fe/Pt(111)	aldehydes	DFT ²²⁷	Sn/Pt(111)	1,5-hexadiene	TPD ²⁴⁹
Ni/Pt(111)	benzene	TPD ²²⁸	Sn/Pt(111)	cyclopentene	HREELS, ²⁵⁰ TPD, ²⁵⁰ DFT, ²⁵⁰ LEED ²⁵⁰
Ni/Pt(111)	1-butene	TPD ²²⁸	Sn/Pt(111)	1,3-cyclohexadiene	DFT ²⁵¹
Pt ₈₀ Fe ₂₀ (111)	crotonaldehyde	GC ²²⁹	Ni/Pt(111)	ammonia	DFT, ^{14,252} TPD ^{14,252}
Sn/Pt(111)	crotonaldehyde	GC ²³⁰	metal/Pt(111)	ammonia	DFT, ²⁵³ TPD ²⁵³
Sn/Pt(111)	cyclohexanone	GC ¹¹⁵	Au/polycrystalline Pt	cyclohexene	TPD ²⁵⁴
Pt/Ni(111)	cyclohexene	TPD, ^{53,54} HREELS ⁵³	reforming		
Co/Pt(111)	cyclohexene	TPD ⁶⁰	Pt/Cu(100)	formic acid	TPD ⁴¹
Cu/Pt(111)	cyclohexene	TPD ²³¹	Sn/Pt(111)	ethanol	TPD ²⁵⁵
Fe/Pt(111)	cyclohexene	TPD ²³¹	Ni/Pt(111)	ethanol	DFT, ^{256–258} TPD, ^{256,258,259} HREELS ²⁵⁷
Ni/Pt(111)	cyclohexene	TPD, ^{54,89,232} HREELS, ^{15,89} NEXAFS ¹⁵	transition metal/ Pt(111)	ethanol	DFT, ²⁶⁰ TPD ²⁶⁰
Ni/Pt(111)	deuterium	TPD ⁸⁹	Ni/polycrystalline Pt	ethanol	DFT, ²⁶¹ TPD, ²⁶¹ HREELS ²⁶¹
Pt/Ni(100)	ethylene	TPD, ⁵² XPS, ⁵² LEED ⁵²	Ni/Pt(111)	ethylene glycol	DFT, ^{257,258} TPD, ^{256,258,259} HREELS ^{256,257}
Pt/Ni(110)	ethylene	TPD ⁵²	transition metal/ Pt(111)	ethylene glycol	DFT, ²⁶⁰ TPD ²⁶⁰
Pt/Ni(111)	ethylene	TPD ⁵⁴	Ni/polycrystalline Pt	ethylene glycol	TPD, ²⁶² HREELS ²⁶²
Co/Pt(111)	ethylene	TPD ⁶⁰	Ni/Pt(111)	glycerol	TPD ^{256,259}
Fe/Pt(111)	ethylene	DFT ²³³	Ni/Pt(111)	glycolaldehyde	DFT, ²³ TPD, ²³ HREELS ²³
Ni/Pt(111)	ethylene	TPD, ^{54,89,232} HREELS ^{54,89}	Pt/Ni(111)	methanol	XPS ²⁶³
metal/Pt(111)	ethylene	DFT ⁹²	Co/Pt(111)	methanol	DFT, ²⁶⁴ HREELS ²⁶⁴
Pt/W(110)	ethylene	TPD, ¹²⁷ HREELS ¹²⁷	Au/Pt(111)	methanol	DFT ²⁶⁵
Sn/Pt(111)	ethylene	TPD ^{110,234}	Ni/Pt(111)	methanol	DFT, ^{256,264} TPD, ^{256,262} HREELS ^{262,264}
Fe/Pt(111)	formaldehyde	DFT ²³³	Ni/polycrystalline Pt	methanol	TPD, ²⁶² HREELS ²⁶²
Ni/Pt(111)	1-hexene	TPD ²²⁸	Pt/W(110)	methanol	DFT, ²⁶⁶ TPD, ²⁶⁶ HREELS ²⁶⁶
Sn/Pt(111)	methylacetylene	TPD ²³⁵	Au/Pt(111)	NO	DFT ²⁶⁵
Sn/Pt(111)	1,3-butadiene	DFT, ²³⁶ TPD ²³⁶	Pt/Au(100)	NO	KMCS ²⁶⁷
Sn/Pt(111)	1,3-butadiene	DFT ²³⁷	Sn/Pt(111)	cyclohexanone	TPD, ²⁶⁸ HREELS, ²⁶⁸ AES, ²⁶⁸ LEED, ²⁶⁸ DFT ²⁶⁸
metal/Pt(111)	1,3-butadiene	DFT ²³⁸	Sn/Pt(111)	ethylene oxide	TPD, ²⁶⁹ HREELS, ²⁶⁹ UPS, ²⁶⁹ DFT ²⁶⁹
metal/Pt(111)	cyclohexene	DFT, ²⁷ TPD ²⁷	oxidation		
Ni/polycrystalline Pt	cyclohexene	DFT, ²³⁹ TPD, ²³⁹ HREELS ²³⁹	Pt/Ru(0001)	CO	STM, ¹²⁴ TPD/TPR ¹²⁴
Ni/Pt(111)	acrolein	TPD, ²⁴⁰ HREELS ²⁴⁰	Pt/Ru(111)	CO	DFT ²⁷⁰
metal/Pt(111)	acrolein	DFT, ^{241,242} TPD, ²⁴¹ HREELS ²⁴¹	Pt ₃ Ni(111)	CO	DFT ²⁷¹
metal/Pt(111)	1,4-cyclohexadiene	DFT ²⁴³	Pt ₂ Ni ₂ (111)	CO	DFT ²⁷¹
Ni/Pt(111)	1,3-cyclohexadiene	DFT ²⁴⁴	PtNi ₃ (111)	CO	DFT ²⁷¹
Ni/Pt(111)	propanal	DFT, ²⁴⁵ TPD ²⁴⁵	Fe/Pt(111)	CO	DFT, ²⁰⁸ TEM, ²⁰⁸ UPS, ²⁰⁸ HREELS, ²⁰⁸ XPS ²⁰⁸
Co/Pt(111)	acetaldehyde	DFT ²⁴⁶	FeO _{1-x} /Pt(111)	CO	TEM, ²⁷² DFT, ²⁷² XPS, ²⁷² UPS ²⁷²
Co/Pt(111)	acetone	DFT ²⁴⁶	NiO _{1-x} /Pt(111)	CO	TEM, ²⁷³ DFT, ²⁷³ XPS, ²⁷³ UPS ²⁷³
metal/Pt(111)	acetone	DFT ²⁴⁷	Pt/Ru(0001)	methanol	FTIRAS, ²⁷⁴ TPD ²⁷⁴
dehydrogenation			hydrodesulfurization		
metal/Pt(111)	ethyl	DFT ⁹²	Ni/Pt(111)	thiophene	TPD ⁸⁸
metal/Pt(111)	vinyl	DFT ⁹²	sulfidation		
Sn/Pt(111)	methylacetylene	TPD ²³⁵	Cu/Pt(111)	S ₂	XPS, ²⁷⁵ XAES, ²⁷⁵ TDS ²⁷⁵
Sn/Pt(111)	ethylene	TPD ²⁴⁸	Sn/Pt(111)	S ₂	TDS, ¹¹⁶ PES ¹¹⁶
Sn/Pt(111)	propylene	TPD ²⁴⁸	Zn/Pt(111)	S ₂	XPS, ²⁷⁵ XAES, ²⁷⁵ TDS ²⁷⁵
Sn/Pt(111)	isobutylene	TPD ²⁴⁸			

subsurface structures bond to cyclohexene more weakly than Pt(111) and the corresponding 3d–Pt–Pt(111) surface structures. For example, DFT results indicate that both cyclohexene and atomic hydrogen are more weakly bonded on Pt–Ni–Pt(111) than on Ni–Pt–Pt(111), Pt(111), and

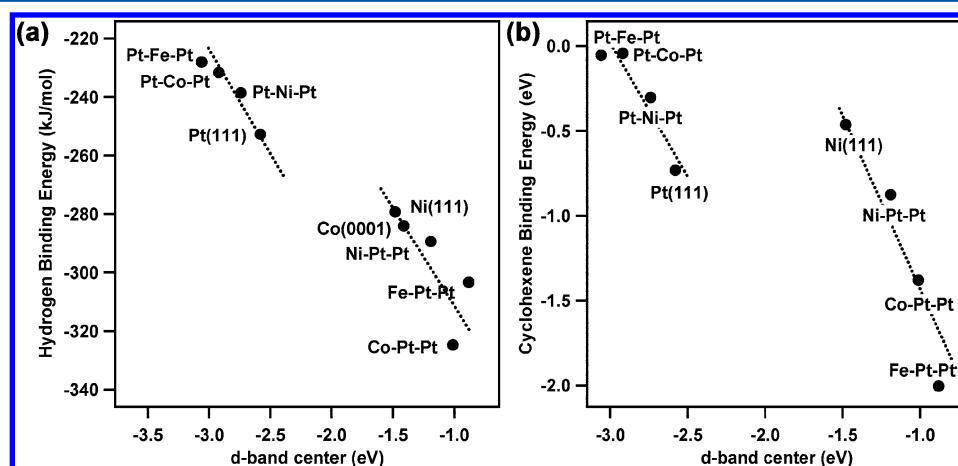
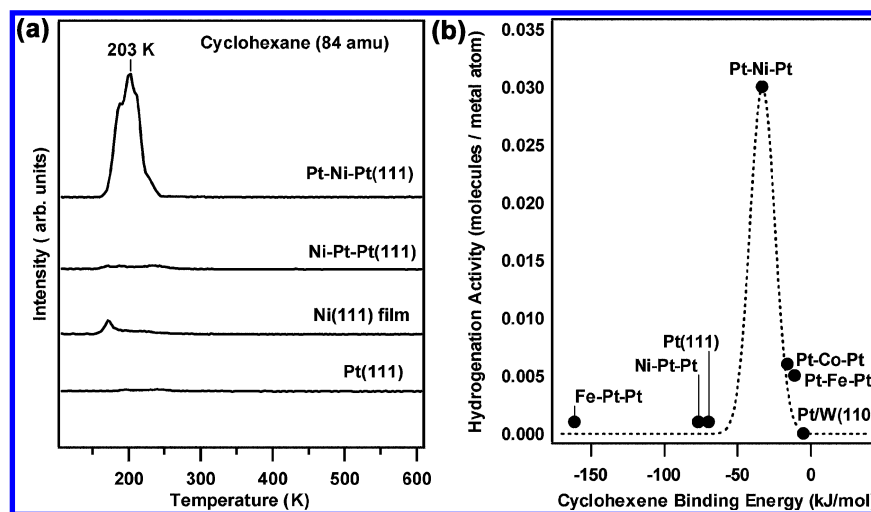
Ni(111), suggesting that the subsurface Pt–Ni–Pt(111) structure should be more effective for the low-temperature hydrogenation of cyclohexene than the other three surfaces. This has been confirmed experimentally by comparing the hydrogenation activity of cyclohexene on these four surfaces

Table 4. Summary of Selected Hydrogenation Reactions over Pt-Based Bimetallic Catalysts

bimetallic catalyst	support	synthesis method	reactants	reactor	temperature	characterization techniques
Pt–Ni Pt–Co Pt–Cu ^{143,238,243,244,247,276} Pt–Co ²⁷⁷	γ -Al ₂ O ₃ α -Al ₂ O ₃ ZrO ₂ AC SiO ₂ γ -Al ₂ O ₃ TiO ₂	impregnation impregnation	1,3-cyclo-hexadiene, 1,3-butadiene, 1,4-cyclo-hexadiene, benzene benzene	batch flow flow	308 K 343 K	XAS, TEM, CO chemisorption, XRD, FTIR XAS, TEM, CO chemisorption, TPR
Pt–Ni ²⁷⁸	SiO ₂ SiO ₂ – TiO ₂ mixed oxides	impregnation	toluene	flow	353–573 K	N ₂ adsorption, ICP, TPR, XRD, TOF-SIMS
Pt–Co ^{279,280}	γ -Al ₂ O ₃	impregnation	cyclohexene	batch flow	303 K 273 K	XAS, FTIR, CO chemisorption
Pt–Co ^{279,280}	γ -Al ₂ O ₃	impregnation	benzene	batch flow	303 K 343 K	XAS, FTIR, TPR, CO chemisorption, H ₂ chemisorption
Pt–Ni ²⁸⁰	γ -Al ₂ O ₃	impregnation	cyclohexene	batch flow	303 K 273 K	FTIR, TPR, H ₂ chemisorption
Pt–Ni ²⁸⁰	γ -Al ₂ O ₃	impregnation	benzene	batch flow	373 K 343 K	FTIR, TPR, H ₂ chemisorption
Pt–Pd ¹³⁸	Mg–Al oxides	impregnation	naphthalene	flow	533–613 K	XRD, CO FTIR, SEM
Pt–Pd ¹⁶⁸	γ -Al ₂ O ₃	laser vaporization	toluene	flow	333–500 K	TEM, EDS
Pt–Cu Pt–Au ¹⁴⁷ Pt–Pd ¹³⁹	SiO ₂ γ -Al ₂ O ₃	organic clusters, impregnation impregnation	hexane tetralin naphthalene phenanthrene	flow flow flow	673 K 573 K	DRIFTS, TEM, EDS, CO chemisorption N ₂ adsorption, CO chemisorption, XPS, TPD, TPO, XAS
Pt–Au ²⁸¹ Pt–Rh ²⁸²	SiO ₂ AC	deposition colloid	cinnamaldehyde butyronitrile	batch batch (liq. phase)	423 K 313 K	ICP-AES, TEM, H ₂ -TPD XAS, FTIR, CO chemisorption
Pt–Zn ²⁸³	TiO ₂	impregnation	toluene crotonaldehyde	flow	333 K	FTIR, XPS, XRD, CO chemisorption, H ₂ chemisorption
Pt–Ge ¹⁵²	TiO ₂	reductive deposition precipitation	citral	batch (liq. phase)	343 K	TPR
Pt–Ni ²⁴⁷	SiO ₂ γ -Al ₂ O ₃ TiO _x	impregnation	acetone	batch	308 K	XAS, TEM, CO chemisorption, FTIR
Pt–Sn ¹⁵⁰	SiO ₂	reductive deposition precipitation	crotonaldehyde cinnamaldehyde	flow (liq. phase)	333–353 K 313–353 K	TPR
Pt–Sn Pt–Ga ¹⁴⁰	CNF	reductive deposition precipitation, impregnation	cinnamaldehyde	batch flow	313 K	ICP-OES, EDS, TEM, XAS, H ₂ chemisorption, N ₂ adsorption
Pt–Sn ²⁸⁴ Pt–Sn ²⁸⁵	MgO C	impregnation impregnation	crotonaldehyde citral	flow flow (liq. phase)	333 K 473 K 773 K	XRD, TEM, XPS N ₂ adsorption, XRD, TEM, TPR, CO chemisorption
Pt–Fe ²⁸⁶	SiO ₂	impregnation	cyclohexane citral	flow (liq. phase)	543 K 343 K	FTIR, TEM, XAS, H ₂ chemisorption
Pt–Fe ²⁸⁷ Pt–Fe ²⁸⁸ Pt–Pd ²⁸⁹ Pt–Re ²⁹⁰	SiO ₂ γ -Al ₂ O ₃ none TiO ₂	impregnation organic clusters colloid impregnation	acetic acid 1,3-butadiene acrolein N-methyl-pyrrolidin-2-one	flow flow batch flow	463–513 K 298 K 293–473 K 393 K	DRIFTS, H ₂ chemisorption H ₂ adsorption, TEM, EDS, TPR XPS, TEM, EDS N ₂ adsorption, XRD, ICP-OES, TPR
Pt–Ni ¹⁶²	γ -Al ₂ O ₃	reverse micelle	1,3-butadiene	batch	308 K	TEM, AAS, XAS, FTIR, CO chemisorption
Pt–Sn ²⁹¹	NaY zeolite	impregnation, reductive deposition precipitation	furfural	flow	423 K	FTIR, ICP, XRD, XPS, TPD, N ₂ adsorption
Pt–Sn ¹⁴²	SiO ₂	organic clusters	furfural	flow (liq. phase)	363 K 393 K	TPR, TEM, N ₂ adsorption, CO chemisorption
Pt–Ni ^{292,293} Pt–Co ¹⁵⁵	γ -Al ₂ O ₃ MCF-17	impregnation colloid, impregnation	maleic anhydride CO ₂	flow flow	313–423 K 473–573 K	XRD, TPR TEM, XPS, XAS

Table 4. continued

bimetallic catalyst	support	synthesis method	reactants	reactor	temperature	characterization techniques
Pt–Co ^{294,295}	NaY γ -Al ₂ O ₃	impregnation	CO	flow	473–533 K	XAS, TPR, XPS, XRD
Pt–Mo ²⁹⁶	γ -Al ₂ O ₃	impregnation	CO	flow	573 K	XAS, CO chemisorption
Pt–Sn ²⁹⁷	TiO ₂	impregnation	citral	flow (liq. phase)	343 K	EDS, XRD, TEM, N ₂ adsorption
Pt–Co ²⁹⁸	C	colloid, impregnation	unsaturated aldehydes	N/A	N/A	XRD, TEM, EDS, ICP, ATR-IR, XPS
Pt–Zn ¹⁴¹	SiO ₂ AC	impregnation	crotonaldehyde	flow	353 K	XPS, AES, TPR, CO chemisorption
Pt–Sn ²⁹⁹	SiO ₂ α -Al ₂ O ₃	impregnation	crotonaldehyde	batch (liq. phase)	313 K	H ₂ chemisorption, CO chemisorption, TEM, TPR
Pt–Mn	CNT	microwave-assisted polyol reduction	cinnamaldehyde	flow (liq. phase)	333 K	ICP, XRD, XPS, TEM
Pt–Fe						
Pt–Cu						
Pt–Ni						
Pt–Zn						
Pt–Sn						
Pt–Co ¹⁶⁶						
Pt–Ru ³⁰⁰	CNT	colloid, impregnation	cinnamaldehyde	batch (liq. phase)	343 K	FTIR, TEM,
Pt–Co	SiO ₂	impregnation	cinnamaldehyde	batch (liq. phase)	353 K	TPR, TEM, XAS, CO chemisorption
Pt–Cu ³⁰¹						

Figure 10. DFT calculations of binding energies of hydrogen and cyclohexene on Pt–3d–Pt(111) and 3d–Pt–Pt(111) surfaces.²⁷Figure 11. (a) TPD of hydrogenation of cyclohexene on Ni/Pt(111) monometallic and bimetallic surfaces; (b) volcano-type relationship between hydrogenation activity and surface d-band center value of 3d/Pt(111) surfaces.²⁷

using temperature-programmed desorption (TPD), as shown in Figure 11.²⁷ As illustrated in the TPD peak area of the cyclohexane product, the subsurface Pt–Ni–Pt(111) structure shows the highest hydrogenation yield, with the desorption peak centered at a very low temperature of 203 K. Similar Pt-terminated bimetallic surface structures can be produced by depositing one monolayer of Pt on a Ni(111) substrate, which also possesses the novel low-temperature pathway for cyclohexene hydrogenation.⁵³

The trend in the DFT calculations in Figure 10b also shows that the binding energies of cyclohexene on Pt–Co–Pt(111) and Pt–Fe–Pt(111) are even weaker than that on Pt–Ni–Pt(111). Although this might suggest that the former two surfaces would be more active toward hydrogenation than Pt–Ni–Pt(111); one should keep in mind that the adsorption of cyclohexene needs to be strong enough for the hydrogenation to take place. One would therefore expect to observe a volcano relationship for the hydrogenation activity as the d-band center moves further away from the Fermi level, i.e., when the adsorption of cyclohexene becomes too weak for hydrogenation to occur. This is verified experimentally in the results shown in Figure 11b. The hydrogenation yield from TPD measurements is the highest on Pt–Ni–Pt(111) but starts to decrease on the Pt–Co–Pt(111) and Pt–Fe–Pt(111) surfaces, where the binding of cyclohexene becomes too weak for hydrogenation to occur. On the other side of the volcano curve, the binding energies of cyclohexene on the 3d–Pt–Pt(111) surfaces are too strong, preventing the effective hydrogenation of cyclohexene.²⁷

Extension to Polycrystalline Ni/Pt Films. Polycrystalline bimetallic films provide a potential way to bridge the materials gap between single-crystal surfaces and supported catalysts. As illustrated earlier in Figure 4, it is possible to assume that the surface chemistry of a bimetallic nanoparticle should be dominated primarily by the first few atomic layers. It is also reasonable to assume that the chemistry of the individual crystal facets on the nanoparticle (primarily (111) and (100) for an fcc nanoparticle) can be approximated by their respective single-crystal extension.³³ This is verified by studying cyclohexene hydrogenation on Pt–Ni–Pt subsurface structures prepared on a polycrystalline Pt film consisting of mainly the (111) and (100) facets.²³⁹ Similar to Pt(111), monolayer Ni was deposited on a Pt foil at room temperature to produce the Ni–Pt–Pt surface structure, followed by annealing to higher temperatures to obtain the Pt–Ni–Pt subsurface structure.³³ Similar to the corresponding single-crystal surfaces, the subsurface Pt–Ni–Pt polycrystalline structure shows significantly higher hydrogenation activity than that from the polycrystalline Pt and Ni surfaces. These results confirm the assumption that the trend observed on single-crystal bimetallic surfaces can be extended to the polycrystalline counterparts.

Reactor Evaluation of Supported Ni/Pt Catalysts. Supported monometallic Pt and bimetallic Pt–Ni and Pt–Co catalysts have been synthesized on γ -Al₂O₃ using the incipient wetness method.^{280,303} Characterization of the catalysts by a variety of techniques, including EXAFS, confirms the formation of Pt–3d bimetallic bonds. As shown earlier in Figure 5, the Pt–Ni/ γ -Al₂O₃ catalyst is Pt-terminated and resembles the subsurface Pt–Ni–Pt structure. The Pt-terminated configuration is also consistent with results by Sedlacek et al. that the surfaces of Pt–Ni alloys are enriched in Pt when treated with H₂,³⁰⁴ as well as with findings reported by Arenas-Alatorre et al. for Pt–Ni catalysts supported on SiO₂³⁰⁵ and by Mu et al. for

Pt–Ni catalysts supported on graphite.²⁰⁹ Because the Pt-terminated structure is thermodynamically stable in the presence of hydrogen (Figure 6), one would expect that the Pt–Ni/ γ -Al₂O₃ catalyst should be very active for cyclohexene hydrogenation.

The supported catalysts were evaluated using both batch and flow reactors to determine the hydrogenation kinetics of cyclohexene at a low temperature of 303 K. The hydrogenation rate constants were determined to be 1.7, 21, and 24 min^{−1} for Pt/ γ -Al₂O₃, Pt–Co/ γ -Al₂O₃, and Pt–Ni/ γ -Al₂O₃, respectively.²⁸⁰ The trend observed in the rate constant for cyclohexene hydrogenation is consistent with that from the single-crystal surfaces for the same reaction, Pt–Ni–Pt(111) > Pt–Co–Pt(111) > Pt(111), as shown earlier in the volcano curve in Figure 11b. The similar trend between DFT predictions on single-crystal surfaces, UHV experimental studies on single-crystal and polycrystalline model surfaces, and reactor evaluation over supported catalysts provides an important demonstration of designing bimetallic catalysts from combined theoretical and experimental approaches.

4.1.1.2. Low-Temperature Hydrogenation of Olefins, Dienes, and Aromatics. Similar theoretical and experimental studies have been extended to the hydrogenation of C=C bonds in a variety of molecules over Pt–3d–Pt(111) subsurface structures and supported Pt–3d catalysts. Goda et al.³⁰⁶ performed DFT calculations of 1-butene and 1-hexene on 3d/Pt(111) surfaces and found that the subsurface Pt–3d–Pt(111) structure binds more weakly to 1-butene and 1-hexene than on Pt(111) and 3d–Pt–Pt(111) surfaces, similar to the trend observed for cyclohexene. Murillo et al.²²⁸ verified the DFT predictions with TPD measurement of facile low-temperature hydrogenation of 1-butene and 1-hexene on Pt–Ni–Pt(111). These results further suggest that DFT calculations of surface d-band center and adsorbate binding energy can be used as descriptors for catalysts with good hydrogenation activity. Similar DFT calculations have been performed for the binding energies of 1,3-butadiene,²³⁸ 1,3-cyclohexadiene,²⁴⁴ 1,4-cyclohexadiene,²⁴³ and benzene²⁷⁷ on 3d/Pt(111) surfaces. On the basis of the binding energies and subsurface Pt–3d–Pt(111) structures, correspondingly supported Pt–3d catalysts are predicted to show high hydrogenation activity for these molecules. These DFT predictions have been confirmed in reactor studies, as described below.

Hydrogenation of 1,3-Butadiene, 1,3-Cyclohexadiene, And 1,4-Cyclohexadiene. Bimetallic Pt–M (M = Co, Ni, Cu) are active toward the low-temperature hydrogenation of all three molecules when supported on γ -Al₂O₃.^{238,243} Pt–Ni and Pt–Co bimetallic catalysts both show higher hydrogenation rates than monometallic Pt. The Pt–Cu/ γ -Al₂O₃ catalyst shows lower activity than Pt/ γ -Al₂O₃ in batch and flow reactor studies; however, Pt–Cu/ γ -Al₂O₃ shows higher selectivity toward cyclohexene and butenes than the other catalysts, indicating that it is a promising catalyst for partial hydrogenation reactions.^{238,243} Similarly to the Pt–Ni bimetallic catalyst, the surface structure of the Pt–Cu catalyst has been shown to be influenced by the surrounding atmosphere.³⁰⁷ The Pt–Fe/ γ -Al₂O₃ bimetallic catalyst also shows higher selectivity toward 1-butene rather than full hydrogenation to *n*-butane.²⁸⁸

The hydrogenation of 1,3-butadiene has also been used as a probe reaction to further understand the catalytic properties of supported Pt–Ni catalysts. Combined EXAFS characterization and reactor studies compare Pt–Ni catalysts prepared using either sequential or coimpregnation methods. The results reveal

that coimpregnation leads to higher hydrogenation activity and that the hydrogenation activity is directly related to the extent of Pt–Ni bimetallic bond formation.¹⁴³ Furthermore, by comparing the hydrogenation activity of Pt–Ni supported over low- and high-surface-area alumina and zirconia, it is revealed that the surface area of the oxide supports also plays a role in controlling the hydrogenation rate of 1,3-butadiene.²⁷⁶

Selective Hydrogenation of Acetylene in Ethylene. The selective hydrogenation of acetylene in the presence of ethylene is an important reaction because acetylene poisons the catalysts in ethylene polymerization reactions.³⁰⁸ The Pt–Ni/ γ -Al₂O₃ bimetallic catalysts show a higher selectivity for acetylene hydrogenation in the presence of excess ethylene than the monometallic Pt and Ni catalysts.³⁰³ The selective hydrogenation of acetylene is also a probe reaction to determine the effect of impregnation sequence of the Pt and Ni metal precursors. By impregnating Pt first, the bimetallic catalyst is much more active for acetylene hydrogenation. EXAFS measurements confirm bimetallic bond formation in the Pt-first catalyst but not in the Ni-first catalyst, likely due to the possible diffusion of Ni²⁺ into the cavities of the γ -Al₂O₃ support to produce Ni aluminate. However, at higher Ni loadings the impregnation sequence does not seem to play an important role.³⁰³

Hydrogenation of Aromatics. The hydrogenation of benzene to cyclohexane is of significant importance in the petroleum industry and for environmental protection. The process of benzene hydrogenation has been utilized commercially for the production of cyclohexane, which is one of the key intermediates in the synthesis of Nylon-6 and Nylon-66.³⁰⁹ DFT calculations identified Pt–Co bimetallic catalysts as promising materials for the hydrogenation of benzene, which were confirmed experimentally over supported Pt–Co/ γ -Al₂O₃ at a relatively low temperature of 343 K.^{280,310} The hydrogenation rate over Pt–Co/ γ -Al₂O₃ was significantly higher than that over Co/ γ -Al₂O₃ or Pt/ γ -Al₂O₃.^{279,280} Comparative studies have also been performed on different supports that reveal that hydrogenation of benzene at 343 K over Pt–Co bimetallic catalysts follows the activity trend of activated carbon (AC) \gg SiO₂ $>$ γ -Al₂O₃ $>$ TiO₂. The AC support exhibits the highest activity and performance due to the greatest extent of Pt–Co bimetallic formation from the EXAFS measurements.²⁷⁷ Another feature of Pt–Co supported catalysts is that almost all Pt atoms in these catalysts exist in the form of Pt–Co, and the remaining Co forms a Co phase on the metal oxide support.²⁹⁵

In addition to bimetallic bond formation, Pt-based bimetallic catalysts improve performance by increasing the reducibility of alloyed metals.^{171,311} For example, Pt–Ni, Pt, and Ni supported on SiO₂ and mixed TiO₂ + SiO₂ oxides were tested for the hydrogenation of toluene to methylcyclohexane for the production of cleaner-burning fuels. TPR experiments indicated that Pt promoted the reducibility of NiO, partially explaining the increased activity of the bimetallic Pt–Ni catalyst compared with either monometallic catalyst.²⁷⁸

Reports of hydrogenation activity on Pt–Pd catalysts have been conflicting. Pt–Pd catalysts supported on mixed magnesium and aluminum oxides are active for the removal of aromatics from diesel fuel to lower emissions. A higher Pd/Pt ratio leads to higher hydrogenation of naphthalene.¹³⁸ However, the activity of Pt–Pd/ γ -Al₂O₃ for the hydrogenation of toluene does not show any synergistic activity, with the activity of the bimetallic catalyst being simply the sum of the

activity of each monometallic catalyst.¹⁶⁸ The difference in reports seen on Pt–Pd may be due to different preparation techniques because different techniques have been shown to strongly influence the degree of bimetallic bond formation.³¹²

Pt–Pd catalysts have exhibited a stronger bimetallic effect and greater sulfur tolerance when promoted with fluorine. Pt–Pd/ γ -Al₂O₃ catalysts with and without fluorine were prepared by incipient wetness impregnation for hydrogenation of polyaromatic hydrocarbons. Pt–Pd catalysts promoted with F showed higher activity than the unpromoted Pt–Pd catalyst. EXAFS analysis showed that the Pt–Pd alloy was disrupted at high conversions of reactants, but the catalysts synthesized with F did not exhibit a disruption of the Pt–Pd bonds.¹³⁹ Babu et al. have shown that the interaction of Pt with Pd led to a reduction in the Fermi level local density of states at the Pd sites. This electronic modification may be the cause of improved catalytic performance of Pt–Pd catalysts with high coordination numbers for bimetallic Pt–Pd bonds.³¹³

Hydrogenation of *m*-Cresol. The hydrodeoxygenation (HDO) of *m*-cresol was performed over Pt–Co/ γ -Al₂O₃ and Pt–Ni/ γ -Al₂O₃ to determine the role of hydrogenation for HDO.³¹⁴ The bimetallic catalysts were found to be very active toward the saturation of the aromatic ring, leading to a facile HDO rate in combination with the dehydration function of the γ -Al₂O₃ support. Because of the importance of HDO in converting biomass-derived oxygenates to fuels and chemicals, it is anticipated that the low-temperature hydrogenation activity of Pt–3d bimetallic catalysts should play a significant role in HDO catalysis.

4.1.2. C=O Hydrogenation. Catalytic hydrogenation of the C=O bond is an important industrial reaction for organic synthesis.^{315,316} The selective hydrogenation of the C=O bond in α,β -unsaturated aldehydes has been of growing interest for the production of fine chemicals and pharmaceutical precursors.^{315,317} More recently, C=O bond hydrogenation has been considered as an important initial step in catalytic conversion of cellulosic biomass.^{318,319} In this section we will first use the hydrogenation of propanal over Pt–Ni bimetallic catalysts as an example to demonstrate the correlation between DFT calculations of binding energies, UHV studies of low-temperature hydrogenation, and batch and flow reactor evaluation. The rest of the section will focus on using bimetallic surfaces and catalysts to promote the selective C=O bond hydrogenation in unsaturated aldehydes.

4.1.2.1. Example: Hydrogenation of Propanal. The hydrogenation of propanal is used as a probe reaction to correlate the activity of C=O bond hydrogenation over Pt–Ni bimetallic surfaces and catalysts.²⁴⁵ DFT calculations predict that propanal is more weakly bound to the Pt–Ni–Pt(111) subsurface structure than on either Ni or Pt, suggesting a possible low-temperature C=O hydrogenation pathway based on trends observed for C=C hydrogenation. UHV studies using TPD on Ni-modified polycrystalline Pt foil verify that different bimetallic surface structures exhibit distinct C=O hydrogenation activity, with the Pt–Ni–Pt subsurface structure demonstrating much higher activity for propanal hydrogenation than Pt, Ni, and the Ni–Pt–Pt surface structure. The UHV results are extended to supported Pt–Ni/ γ -Al₂O₃ bimetallic catalysts. In the gas-phase hydrogenation of propanal, batch and flow reactor studies show that the Pt–Ni/ γ -Al₂O₃ bimetallic catalyst exhibits a higher C=O hydrogenation rate and a lower activation barrier than the corresponding monometallic catalysts.²⁴⁵ The excellent correlation between DFT predic-

tions, UHV studies on model surfaces, and catalytic evaluation of supported catalysts demonstrates the feasibility to predict bimetallic catalysts with enhanced C=O hydrogenation activity.

Using similar approaches, DFT calculations and reactor evaluations were performed for C=O bond hydrogenation of acetaldehyde²⁴⁶ and acetone^{246,247} over supported Pt–3d bimetallic catalysts. Pt–Co/ γ -Al₂O₃ bimetallic catalysts showed significantly higher hydrogenation rates for acetaldehyde and acetone than the monometallic Pt and Co catalysts.²⁴⁶ Acetone hydrogenation was used as a probe reaction to determine the effect of oxide supports over Pt–Ni supported on SiO₂, γ -Al₂O₃, and TiO₂ at 308 K.²⁴⁷ It was found that Pt–Ni/SiO₂ exhibited significantly higher hydrogenation activity than the other supports. These hydrogenation results correlate well with EXAFS data showing the extent of Pt–Ni bond formation of SiO₂ > γ -Al₂O₃ > TiO₂.²⁴⁷

4.1.2.2. Selective Hydrogenation of C=O in Unsaturated Aldehydes. The selective hydrogenation of acrolein, the smallest α,β -unsaturated aldehyde, has been investigated on several 3d/Pt(111) surfaces.^{17,241} DFT binding energies of acrolein on H/Pt–Ni–Pt(111), H/Ni–Pt–Pt(111), and H/Pt(111) surfaces are calculated using di- σ -C–C, di- σ -C–O, and η^4 (C,C,C,O) adsorption configurations, as shown in Figure 12a.¹⁷ Figure 12b shows the hydrogen and acrolein binding

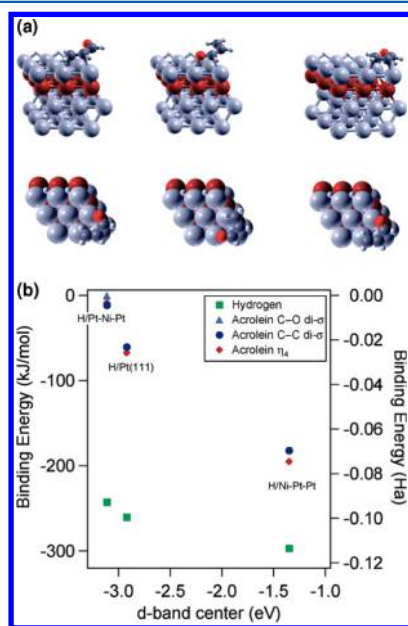


Figure 12. (a) Side view and top view of configurations of adsorbed acrolein through di- σ -C–C, di- σ -C–O, and η^4 (C,C,C,O) on the Pt–Ni–Pt(111) surface. (b) DFT calculations of acrolein and hydrogen binding energies versus the surface d-band center for H/Pt–Ni–Pt(111), H/Pt(111), and H/Ni–Pt–Pt(111) surfaces.¹⁷

energies on the three surfaces. The DFT results show that the binding energies of acrolein are in the order of H/Pt–Ni–Pt(111) < H/Pt(111) < H/Ni–Pt–Pt(111).¹⁷ On the H/Pt(111) and H/Ni–Pt–Pt(111) surfaces, acrolein tends to be adsorbed through the di- σ -C–C mode, whereas on the H/Pt–Ni–Pt(111) surface, the similar binding energies will lead acrolein to be adsorbed through both the C=O and C=C moieties. The direct interaction of the C=O group in the latter bonding configuration at least partially contributes to the experimentally observed hydrogenation of the C=O bond on

the H/Pt–Ni–Pt(111) surface. In comparison, bonding of acrolein occurs through the C=C moiety over H/Pt and H/Ni–Pt–Pt(111) surfaces, preventing the selective hydrogenation of the C=O bonds.^{17,241} The presence of the di- σ -C–O configuration has also been proposed for the adsorption of α,β -unsaturated aldehydes on Pt–Fe/SiO₂, responsible for the selective hydrogenation of the C=O bond for the formation of α,β -unsaturated alcohols.²⁸⁶

The selective hydrogenation of acrolein has been extensively investigated over many Pt-based bimetallic catalysts. On unsupported Pt–Pd catalysts, it was found that the metal ratios strongly affected the hydrogenation products. For acrolein hydrogenation at temperatures from 293 to 473 K, it was found that propanal was the primary product for all catalysts. However, for the secondary products, dipropyl ether was formed primarily over Pd, whereas propane and propanol were formed over Pt. As the surface of the bimetallic catalyst increased in Pt atoms, the catalyst behaved more like the monometallic Pt catalyst.²⁸⁹

Although Au is typically regarded as an inactive metal for hydrogenation reactions, combining Au with Pt can greatly increase its activity.²⁸¹ Au is a poor hydrogenation metal because it does not dissociatively adsorb H₂.³²⁰ UHV studies have shown that CO binds to the surface of Pt on top of Au(111) more strongly than to clean Pt because the Au substrate increases the activity of the Pt overlayer, with the change in the CO binding energy being proportional to the shift of the d-band center of the Pt metal.^{320,321} Such a modification effect on model surfaces has also been observed in supported Pt–Au catalysts. Pt–Au/SiO₂ catalysts were found to be highly active for the hydrogenation of α,β -unsaturated compounds because of the synergism between the Pt and Au metals.^{281,322} The high hydrogenation activity of Pt–Au could be a result of the rapid H₂ dissociation on Pt and Pt–Au nanoparticles supported on SiO₂ and TiO₂. H₂ dissociation on Pt–Au and Pt is considerably faster than H₂ dissociation on Au, because H₂ adsorption on Pt atoms is dissociative and no activation barriers are involved.³²⁰ In addition to greater hydrogenation activity, Pt–Au shows enhanced resistance to deactivation when compared with a monometallic Pt catalyst.¹⁴⁷

In general, the hydrogenation of α,β -unsaturated aldehydes over Pt-based catalysts usually yields the saturated aldehydes as the dominant products because of defect sites present in the metallic structure. Defects on metal surfaces favor interactions with the C=C moiety, which account for the undesired aldehyde products. It is hypothesized that 100% selectivity can be achieved through careful control of the size and shape of metallic active sites.²⁹⁸ Tsang et al. confirmed that, at larger crystal sizes, Pt nanoparticles were more active for selective hydrogenation of the C=O bond in cinnamaldehyde. This is because the fraction of defect sites on Pt nanoparticles decreases with increasing Pt crystal size. Hydrogenation of the C=O bond in crotonaldehyde over Pt–Sn supported on SiO₂ and α -Al₂O₃ demonstrated that the particle-size effect was not as important on bimetallic catalysts as it was on monometallic catalysts. This was because the addition of Sn had a greater effect on the selectivity to the unsaturated alcohol than the change in particle size.²⁹⁹ Therefore, to increase the selectivity toward hydrogenation of the carbonyl bond with smaller metallic nanoparticles, it is necessary to add a second metal. This can be achieved by the addition of a more

electropositive metal such as Co,^{166,298} Ge,¹⁵⁰ Fe,^{150,284} Ga,¹⁴⁰ Ni,²⁸⁴ or Sn.²⁸⁴

For the hydrogenation of cinnamaldehyde, the addition of Co to Pt nanoparticles produces cinnamyl alcohol as the primary product with a selectivity of 99.6%.²⁹⁸ Pt–Co nanoparticles were prepared within a critical size range of 4.0–6.1 nm by colloid chemistry and then were applied to carbon supports. It was found that the Pt–Co/C catalysts hydrogenated the terminal C=O bond with high activity, while the catalyst was inactive toward the C=C bond.²⁹⁸ These results were confirmed by Zheng et al., who showed that Pt–Co/SiO₂ was much more selective toward the hydrogenation of the C=O bond than of C=C in cinnamaldehyde.³⁰¹

Pt–Sn catalysts have also been shown to be active for selective hydrogenation reactions, with the hydrogenation activity and selectivity to unsaturated alcohols being highly dependent on the Sn/Pt ratio. It is suggested that the carbonyl group of α,β -unsaturated aldehydes is activated by a Sn species interacting with the oxygen atom, while dilution of Pt atoms by metallic Sn hinders the hydrogenation of the C=C bond and suppresses the readsorption of the unsaturated alcohol.^{150,285} Catalysts with Pt and Sn in close contact are more selective in the hydrogenation of cinnamaldehyde to cinnamyl alcohol as compared with catalysts with a lesser interaction.¹⁴⁰ The interaction of Sn and Pt in Pt–Sn nanoparticles is known to be affected by the catalyst-preparation method and impregnation sequence. Co-impregnation of the fumed Al₂O₃ support with Pt and small amounts of Sn facilitates the formation of high Pt dispersion; however, sequential impregnation of the fumed Al₂O₃ support with Sn first, followed by Pt, leads to low Pt dispersion.³²³

In addition to the metal affecting selectivity, the support has been found to play a major role in Pt–Sn catalysts. A carbon nanotube (CNT) support can be useful to concentrate reactants in an area close to the active metal,³⁰⁰ whereas supports that exchange oxygen with the reactants, such as TiO₂,²⁹⁷ ZnO,³²⁴ or CeO₂,³²⁴ have been shown to dramatically affect reaction chemistry. The addition of Sn to a Pt catalyst on a reducible support can influence the ability of the support to remove surface carbon through oxygen exchange³²⁴ and help to maintain Sn in a fully reduced state.³²⁵ The removal of surface carbon is critical to prevent deactivation of the catalyst. For example, on TiO₂, selective hydrogenation of crotonaldehyde was performed over Pt/TiO₂ and Pt–Sn/TiO₂ catalysts after reduction at 473 and 773 K. The bimetallic catalyst reduced at high temperature was much more active for crotonaldehyde hydrogenation. The C=O bond was selectively hydrogenated because partially reduced TiO_x species contain oxygen vacancies that interact with the oxygen atom of the carbonyl group and participate in the hydrogenation.²⁸³ In another example, a Pt–Ge/TiO₂ catalyst hydrogenated citral into unsaturated alcohols where both oxidized Ge and TiO₂ species participated in the activation of the C=O bond, indicating there was a strong metal–support interaction (SMSI), but at higher metal loadings the bimetallic effect was dominant.¹⁵²

Pt–Sn catalysts have been found to be active for the partial hydrogenation of furfural when supported on NaY zeolites and SiO₂.^{142,291} Pt–Sn/SiO₂ catalysts were synthesized with varying amounts of Sn, and all catalysts produced furfuryl alcohol from furfural with selectivities greater than 95%. Bimetallic catalysts were more active than the monometallics but exhibited some degree of deactivation. The Pt–Sn catalyst synthesized with a ratio of 1:0.3 Pt/Sn deactivated at the lowest rate.¹⁴² High

hydrogenation activity is favored in large Pt–Sn particles because of the presence of a higher amount of oxidized Sn on the surface of the particles.^{284,311}

4.1.2.3. Hydrogenation of C=O in Other Molecules. The hydrogenation of maleic anhydride can produce many different products, but only some of the products are valuable in industry. Supported Pt–Ni bimetallic catalysts showed higher hydrogenation activity than the corresponding monometallic catalysts. Pt–Ni catalyzed the reaction for the production of succinic acid with 100% conversion and high selectivity to succinic anhydride.^{292,293}

The Pt–Fe/SiO₂ catalyst has been used for the partial hydrogenation of acetic acid. Adding small amounts of Pt to Fe/SiO₂ catalysts increased Fe reducibility, increased activity by 10 times, lowered the apparent activation energy, and maintained the selectivity to acetaldehyde at >70%. On carbon-supported catalysts, the addition of Pt to Fe/C prevented deactivation associated with iron carbide formation.²⁸⁷

Amines are important compounds for manufacturing dyes, solvents, detergents, and drugs. A simple method to form amines is by the reduction of amides, but amides are considered difficult to reduce. Burch et al. found that Pt–Re/TiO₂ supported catalysts, synthesized by impregnation, were able to selectively hydrogenate the C=O bond in *N*-methylpyrrolidin-2-one to form *N*-methylpyrrolidine, an amine. Figure 13

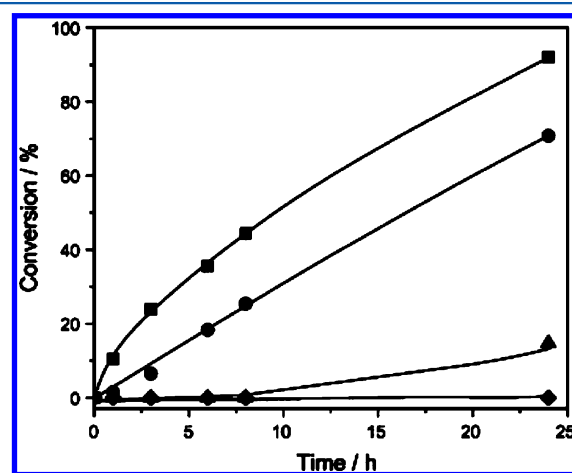


Figure 13. Variation of amide conversion as a function of time for the hydrogenation of *N*-methylpyrrolidin-2-one at 120 °C, 20 bar H₂, stirred at 1500 rpm in hexane using (■) 4 wt % Pt–4 wt % Re/TiO₂, (●) 4 wt % Re–4 wt % Pt/TiO₂, (▲) 4 wt % Pt/TiO₂, and (◆) 4 wt % Re/TiO₂.²⁹⁰ Reproduced with permission from ref 290. Copyright 2011 Elsevier.

shows that both Pt impregnated onto a Re/TiO₂ catalyst and Re impregnated onto a Pt/TiO₂ catalyst showed conversions over 80%, much greater than those of either monometallic catalyst. γ -Al₂O₃ and CeZrO₄ supported catalysts were also effective for hydrogenation of *N*-methylpyrrolidin-2-one, but the TiO₂-based catalysts exhibited increased activity over the other supports due to the presence of oxygen vacancies. DFT studies showed that Re sites activated the C=O bond while Pt aided in the reduction of Re–O groups. The parent monometallic catalysts were not active in this reaction, indicating that close interaction between Re and Pt was critical in providing an active catalyst.²⁹⁰

Table 5. Summary of Selected Dehydrogenation Reactions over Pt-Based Bimetallic Catalysts

bimetallic catalyst	support	synthesis method	reactants	reactor	temperature	characterization techniques
Pt–Sn ³³²	γ -Al ₂ O ₃ / Spinel-Al ₂ O ₃ SiO ₂ Zn–Al– O	impregnation	propane	flow	773 K	N ₂ adsorption, TEM, XRD, TPR, TPO, H ₂ chemisorption
Pt–Cu Pt–Sn Pt–Zn Pt–In ³³³	ZnAl ₂ O ₄ MgAl ₂ O ₄	impregnation	paraffins	flow	855 K	TEM
Pt–Ni ³³⁴	none	impregnation	hydrazine	batch	298 K	TEM, SEM, EDS, XPS, ICP
Pt–Zn ¹⁴¹	SiO ₂ AC	impregnation	isobutane	flow	773 K	XPS, AES, TPR, CO chemisorption
Pt–Sn ³³⁵	SiO ₂	impregnation	cyclohexane	flow	543 K	TEM, FTIR, XAS, H ₂ chemisorption
Pt–Ni ²⁴⁴	γ -Al ₂ O ₃	impregnation	1,3-cyclohexadiene	batch	308 K	FTIR, CO chemisorption
Pt–Ni ³³⁶	AC cloth	impregnation	cyclohexane	flow	523–598 K	XRD, TEM, H ₂ chemisorption
Pt–Sn ³³⁷	γ -Al ₂ O ₃ MgO MgAlO	impregnation	propane	flow	873 K	TEM, EDS, CO chemisorption
Pt–Sn ³³⁸	MgAl ₂ O ₄	impregnation, sol–gel	propane	flow	823 K	N ₂ adsorption, TPD, TPR
Pt–Fe ²⁸⁶	SiO ₂	impregnation	cyclohexane	flow	543 K	FTIR, XAS, TEM, CO chemisorption
Pt–Re ³³⁹	γ -Al ₂ O ₃	impregnation	naphtha	flow	766, 769 K	ICP, TPO, FTIR, N ₂ adsorption, TEM, CO chemisorption
Pt–Bi ³⁴⁰	Al ₂ O ₃ (not specified)	reductive desposition impregnation	1-phenylethano-1, trans-cinnamyl alcohol, 2-octanol	batch (liq. phase)	328, 338, 358 K	XPS, XAS, TEM

Other Pt-based bimetallic catalysts have also shown increased hydrogenation activity such as Ti,³²² Zr,³²² Hf,³²² and Zn²⁸³ for C=O and C=C hydrogenation, Ag³²⁶ for C=C hydrogenation, and Mo²⁹⁶ for CO hydrogenation. For CO hydrogenation, Pt–Mo/ γ -Al₂O₃ bimetallic catalysts were much more active than the monometallic catalysts because Pt aided in the reduction of Mo. Mo segregated to the surface of the supported nanoparticles, and the segregation was unaffected by the sequence of the metal addition. EXAFS results showed that Mo–Mo bond lengths were near that of Pt with Mo on the surface of the metallic nanoparticles.²⁹⁶

4.1.3. N=O and C≡N Hydrogenation. Catalytic hydrogenation of nitriles is an important industrial process to manufacture the nylon monomer, hexamethylenediamine, from adiponitrile. Butyronitrile has been used as a model compound for C≡N hydrogenation because it only contains one nitrile group. In liquid-phase experiments, Siepen et al. found that Pt–Rh/AC catalysts synthesized by a colloid method were active for hydrogenation of the C≡N bond in butyronitrile. EXAFS measurements indicated that Rh atoms were concentrated at the surface of the bimetallic nanoparticles. This finding was confirmed by CO FTIR, which showed a characteristic Rh–dicarbonyl species bound to the catalyst. It was hypothesized that the Pt core atoms draw electrons from the Rh surface atoms, possibly explaining the enhanced hydrogenation activity of the bimetallic catalyst. Enhanced activity was seen on Pt–Rh bimetallic catalysts prepared by sequential impregnation and not in catalysts synthesized with coimpregnation of both metals.²⁸²

Huang and Sachtler³²⁷ investigated the hydrogenation of acetonitrile and butyronitrile in the gas phase in a fixed-bed microreactor and in the liquid phase in an autoclave. They found that addition of Pt to Ni supported on NaY zeolite promotes the reduction of Ni²⁺ and increases the hydrogenation rate of butyronitrile in both the gas and liquid phases. Catalysts with Cu and Pt also supported on NaY zeolite show increased reduction of the metal alloyed with Pt, but the activity is lower for acetonitrile hydrogenation. Addition of Sn to Pt on

SiO₂ decreases the activity for acetonitrile hydrogenation but increases the selectivity to secondary amines.³²⁷

Synthesis of aromatic haloamines is important for the production of dyes, herbicides, and pesticides. Metal catalysts are preferred for the hydrogenation of halonitroaromatics to reduce the environmental impact of traditional hydrogenation with HCl. Liu et al. found that PVP-stabilized Pt–Ru colloids, prepared by a colloid-synthesis method, selectively hydrogenated the N=O bond of *o*-chloronitrobenzene to form *o*-chloroaniline. Catalysts were characterized by TEM, XPS, and XRD, and the reaction was performed in methanol at 303 K. The hydrogenation was most effective with particles composed of 20–90% Ru, with Co²⁺ added to the reaction vessel.³²⁸ Similar studies on Pt–Ru/ γ -Al₂O₃ for the hydrogenation of N=O in 2,5-dichloronitrobenzene also showed high activity and selectivity.³²⁹

Pt–Cu/ γ -Al₂O₃ catalysts can be used for the reduction of nitrates and nitrites into nitrogen for the treatment of drinking water. A bimetallic catalyst is advantageous for this process because copper can reduce nitrates and nitrites but deactivates rapidly in water, whereas monometallic platinum catalysts are inactive for nitrate reduction. By alloying Pt with Cu, the Cu is maintained in a metallic state while the reaction occurs in an aqueous environment. Monometallic catalysts were prepared by impregnation, and bimetallic catalysts were prepared by sequential impregnation or reductive deposition of the second metal. Catalysts were characterized with TEM to confirm nanoparticle size, and CO FTIR was used to confirm the accessibility of Pt on the catalytic support. Reactions performed in an aqueous-phase batch reactor at 283 K showed that nitrates were quickly reduced on the Pt–Cu bimetallic catalyst when both metals were in close contact. Although required for high activity, the addition of copper slightly lowered the selectivity to nitrogen and raised the selectivity to NH₄⁺.³³⁰ Pt–In supported on γ -Al₂O₃ and SiO₂, prepared by impregnation, were also active for the reduction of nitrates in drinking water. XPS and TPR results showed that the catalytic surfaces were enriched in In, but catalysts deactivated quickly due to segregation of the Pt and In.³³¹

4.2. Dehydrogenation Reactions

Selective dehydrogenation is important for the production of chemicals and fuels, as well as for hydrogen storage. Table 5 summarizes selected reactor studies of dehydrogenation of C–H and N–H bonds over supported catalysts, including the synthesis methods, characterization techniques, and dehydrogenation temperatures. Selected UHV studies of dehydrogenation reactions are listed in Table 3.

4.2.1. N–H Bond Scission. Ammonia is regarded as an important hydrogen-storage medium in a hydrogen economy due to its facile decomposition to produce hydrogen. However, the leading catalyst, Ru, is expensive and scarce, preventing it from large-scale commercial utilization. Hansgen et al.¹⁴ have used microkinetic modeling combined with DFT calculations to build a model to identify alternative bimetallic catalysts for ammonia decomposition. A volcano relationship is identified between the nitrogen-binding energy on the surface and the conversion of ammonia, in which the maximum activity is predicted to be with a nitrogen-binding energy of 134 kcal/mol,¹⁴ as shown in Figure 14. Table 6 shows a library of

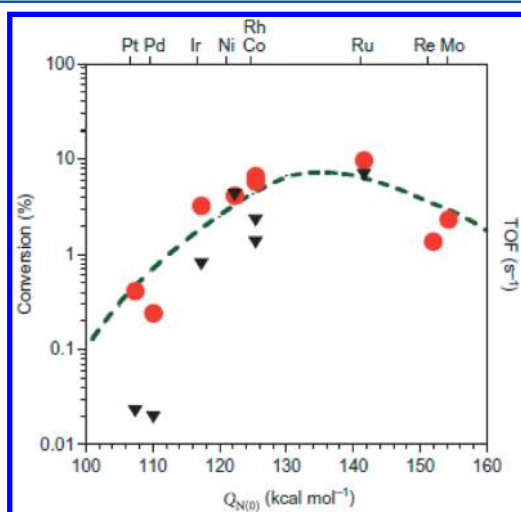
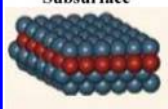

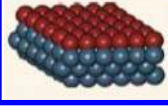


Figure 14. Ammonia decomposition volcano curve.¹⁴

Table 6. Library of DFT Binding Energies and Bond Lengths of Nitrogen Atoms at 1/9 ML Coverage on Various Monolayer Bimetallic Surfaces¹⁴

Configuration	Metal (111) Surface	Nitrogen Binding Energy (kcal/mol)	Bond Length d_{M-N} (Å)
	Pt–Ti–Pt	70.7	1.975
	Pt–V–Pt	81.0	1.975
	Pt–Cr–Pt	76.3	1.965
	Pt–Mn–Pt	77.6	1.968
	Pt–Fe–Pt	78.4	1.969
	Pt–Co–Pt	83.4	1.964
	Pt–Ni–Pt	87.5	1.941
	Pt	102.1	1.954
	Ni	113.8	1.770
	Ni–Pt–Pt	130.7	1.761
	Co–Pt–Pt	126.5	1.780
	Fe–Pt–Pt	134.1	1.864
	Mn–Pt–Pt	207.2	1.854
	Cr–Pt–Pt	188.3	1.894
	V–Pt–Pt	188.1	1.876
	Ti–Pt–Pt	176.1	1.918

nitrogen-binding energies on various bimetallic surfaces, in which the Ni–Pt–Pt(111) surface exhibits a nitrogen-binding energy of 130.7 kcal/mol,¹⁴ slightly lower than the optimal

value. Parallel TPD experiments of ammonia decomposition are performed to compare the activity of surface Ni–Pt–Pt(111), subsurface Pt–Ni–Pt(111), Ni(111), and Pt(111). Consistent with the DFT and microkinetic prediction, the Ni–Pt–Pt(111) surface shows high activity for ammonia decomposition whereas the other three surfaces are inactive.¹⁴ By comparing the desorption temperature of atomic nitrogen from the Ni–Pt–Pt(111) surface with that on Ru(0001),³⁴¹ the results show that the recombinative desorption temperature of nitrogen is lower on Ni–Pt–Pt(111), making it a potentially more active catalyst for NH₃ decomposition. Hansgen et al.²⁵³ have performed further investigations on the decomposition of ammonia on bimetallic surfaces prepared by the deposition of a monolayer of Fe, Co, or Cu on Pt(111) computationally and experimentally. The results reveal that the Fe–Pt–Pt(111) and Co–Pt–Pt(111) surfaces are active for ammonia decomposition whereas the Cu–Pt–Pt(111) surface is inactive for the reaction, consistent with the trend in nitrogen-binding energy in Table 6.

Although the dehydrogenation of NH₃ has not been extended to reactor studies of Pt-based bimetallic catalysts, the production of H₂ from NH₂NH₂ has been reported on supported Pt–Ni catalysts.³³⁴ Hydrazine monohydrate (NH₂–NH₂·H₂O) has been investigated as a potential hydrogen-storage material because it is a liquid at room temperature and has a hydrogen-storage capacity of 8.0 wt %, meeting the Department of Energy (DOE) requirements of hydrogen-storage materials. Singh and Xu have recently explored unsupported Pt–Ni nanocatalysts for the selective dehydrogenation of hydrazine to produce H₂ and N₂ in a liquid-phase batch reactor at room temperature. Their results demonstrate that catalysts with Pt content between 7 and 31 mol % exhibit 100% hydrogen selectivity, whereas the corresponding Ni and Pt monometallic catalysts show no activity.³³⁴

4.2.2. C–H Bond Scission. The dehydration of alkanes is an important part of industrial processes used to produce polymers, ethers, and gasoline. Another potential use of dehydrogenation is to store hydrogen in a chemical with a higher volumetric energy density than hydrogen and to subsequently dehydrogenate the chemical when hydrogen is needed. Current high-temperature dehydration processes lead to sintering and rapid deactivation of catalysts, but by modifying Pt catalysts with a second metal, the selectivity, activity, and stability of the catalyst are maintained.³³⁵ There is a general agreement that Pt is very active for dehydrogenation of hydrocarbons; however, Pt bonds too strongly to the unsaturated carbon intermediates, leading to the formation of coke and deactivation. Therefore, the strategy to improve the dehydrogenation activity is to alloy Pt with another metal to reduce the bonding of unsaturated hydrocarbons.

Such a hypothesis is verified in DFT calculations and UHV studies for the dehydrogenation of cyclohexene to benzene on Pt–Au surfaces.²⁵⁴ As shown in the TPD results in Figure 15a, the production of benzene is enhanced after depositing 0.5 ML Au on Pt, which shows higher benzene yield than on either Pt or Au/Pt surfaces with higher Au coverages. The corresponding AES measurements (Figure 15b) show significant carbon accumulation on unmodified Pt after the TPD experiments, confirming that the Pt bonds too strongly to cyclohexene and decomposes it to produce atomic carbon. In comparison, no carbon accumulation is detected on the 0.5 ML Au/Pt surface after the same experimental procedures. The TPD and AES results are consistent with DFT predictions that the Au/Pt

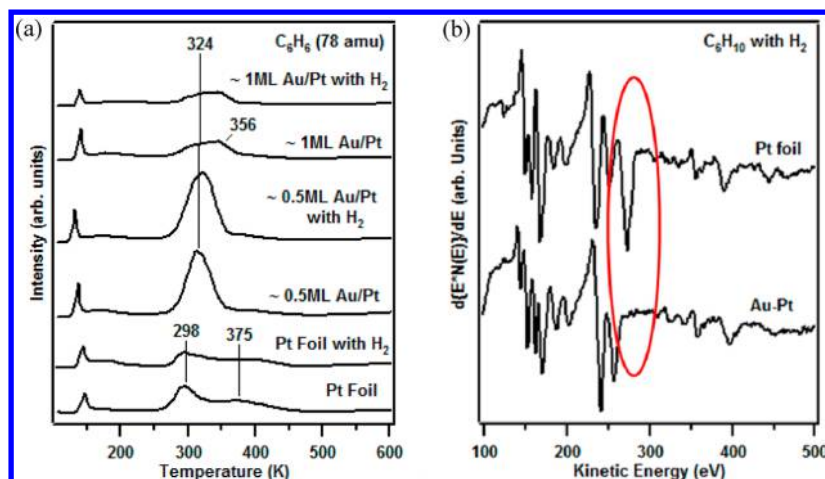


Figure 15. Selective dehydrogenation of cyclohexene on polycrystalline Pt–Au bimetallic surfaces.²⁵⁴

surfaces bind adsorbates more weakly than Pt,²⁵⁴ and the results in Figure 15 indicate that modification of Pt by Au results in a more coking-resistant, and therefore more active, dehydrogenation catalyst.

Similarly, as described in the previous sections, DFT calculations predict that subsurface Pt–Ni–Pt(111) also binds to unsaturated hydrocarbons more weakly than unmodified Pt(111). This is consistent with experimental observations that Pt–Ni–Pt(111) is more active for the dehydrogenation of cyclohexene than either of the parent metal surfaces.¹⁵ Because the Pt-terminated surface should be preferred under the reducing environment of dehydrogenation reactions, the DFT and UHV results suggest that supported Pt–Ni catalysts should be effective dehydrogenation catalysts. This is confirmed in reactor studies that show Pt–Ni/ γ - Al_2O_3 is more active for dehydrogenation of 1,3-cyclohexadiene than either monometallic catalyst.²⁴⁴ The effect of bimetallic catalysts on dehydrogenation is also found to be synergistic for cyclohexane dehydrogenation over Pt–Ni/AC. Hydrogen production on the bimetallic catalysts is enhanced by 1.5 times as compared to the 20 wt % Ni catalyst and by 60 times as compared to the 0.5 wt % Pt catalyst.³³⁶

In addition to Pt–Au and Pt–Ni, modification of Pt by Sn also enhances the resistance to carbon accumulation. Extensive UHV studies by Koel and co-workers have revealed that the addition of Sn on the Pt(111) surface decreases the binding energies of adsorbed molecules.^{235,248,249} The selective dehydrogenation of 1,3-cyclohexadiene is studied using DFT calculations,²⁵¹ which show that the presence of Sn on Pt(111) facilitates the first two dehydrogenation steps that produce benzene, prohibits further decomposition of benzene, and thus increases the selectivity of the dehydrogenation of 1,3-cyclohexadiene to gas-phase benzene. Other DFT and experimental studies of alkenes, such as ethylene,²⁴⁸ propylene,²⁴⁸ isobutylene,²⁴⁸ cyclopentene,²⁵⁰ and a number of C6 hydrocarbons,²⁴⁹ on Sn/Pt alloys also demonstrate that the presence of surface Sn increases the dehydrogenation selectivity. Reactor studies also show that adding only a small amount of Sn to Pt catalysts improves the dehydrogenation selectivity and reduces the deactivation rate.

Addition of Sn to Pt catalysts supported on Zn–Al–O and mixed spinel Al_2O_3/γ - Al_2O_3 has been shown to increase the selectivity to propylene for propane dehydrogenation and decrease the deactivation rate of the catalyst.³³² Similar results

are observed for isobutane dehydrogenation over Pt–Sn/ γ - Al_2O_3 . The selectivity to butenes increases from 53% for the Pt/ γ - Al_2O_3 catalyst up to 85–90% for the Pt–Sn/ γ - Al_2O_3 catalyst.³³⁵ The lower deactivation rate is due to a decrease in the binding energy of unsaturated hydrocarbons on the bimetallic particles, thereby lowering carbon deposits on the bimetallic catalyst.²⁸³ Catalytic activity over Pt–Sn improves by pretreating the catalysts with H_2 and O_2 prior to reaction because of increased metal dispersion on the support.³³⁸

Other metals that promote dehydrogenation reactions when alloyed with Pt are Bi,³⁴⁰ Re,³³⁹ Pd,^{342,343} In,³³³ and Fe.²⁸⁶ Pt supported on spinel Al_2O_3 synthesized with Sn, Cu, and In are active for the dehydrogenation of lower alkanes because these catalysts can withstand harsh reducing and oxidizing conditions.³³³ Over Pt–Fe/ SiO_2 , dehydrogenation activity is enhanced because Pt aids in the reduction of Fe as confirmed by FTIR. Although small amounts of Fe improve catalytic performance, large amounts of Fe lead to rapid deactivation due to the formation of an iron oxide phase.²⁸⁶

Dwindling crude oil reserves and strict air pollution regulations have made reforming of low-octane naphtha into high-octane gasoline an attractive economic opportunity. Liu et al. recently utilized a template synthesis procedure to formulate Pt–Re/ γ - Al_2O_3 with high activity for naphtha dehydrogenation.³³⁹ The synthesis method involved a poly(acrylic acid) (PAA) template to control the morphology of Pt nanoparticles on the surface of the support. TEM and CO chemisorption studies showed similar particle sizes between catalysts synthesized with PAA and catalysts synthesized by traditional impregnation methods. FTIR results of CO adsorption indicated that less bridged CO was present in the catalyst synthesized with PAA, suggesting a lower surface Pt coordination number. Reaction studies performed at 766 and 769 K showed that catalysts prepared with PAA exhibited a 1.4–2.4% higher yield and a longer projected lifetime over commercial Pt–Re catalysts prepared by traditional impregnation. Although small, a 1% increase in yield represents a significant economic prospect in an industry that produces 11 million barrels of reformate from naphtha per day.³³⁹ Another study of naphtha dehydrogenation was performed over Pt–Re/ γ - Al_2O_3 .³⁴⁴ The bimetallic interactions were analyzed using EXAFS and both the Pt L_{III} and Re L_{III} edges were analyzed. If the catalysts were dried in air at temperatures ≤ 773 K prior to reduction, bimetallic bonds were formed. However, if the

Table 7. Summary of Selected Reforming Reactions over Pt-Based Bimetallic Catalysts

bimetallic catalyst	support	synthesis method	reactants	reactor	temperature	characterization techniques
Pt–Re ³⁴⁸	C	impregnation	glycerol, H ₂ O	flow (liq. phase)	483–523 K	CO chemisorption, TPD, XAS, TEM
Pt–Ni Pt–Co Pt–Fe ³⁴⁹	γ -Al ₂ O ₃	impregnation	ethylene glycol, H ₂ O	flow (liq. phase)	453–498 K	CO chemisorption, AAS, ICP
Pt–Ni ³⁵⁰	δ -Al ₂ O ₃	impregnation	<i>n</i> -butane, H ₂ O	flow	578–678 K	none
Pt–Ni ³⁵¹	nanofiber Al ₂ O ₃	impregnation	sorbitol, H ₂ O	flow	N/A	TEM, EDS, ICP/AES, TPR, TPO, TPD, CO chemisorption
Pt–Ni ³⁵²	nanofiber Al ₂ O ₃ ZrO ₂ CeO ₂ SiO ₂ mixed oxides	impregnation	sorbitol, H ₂ O	flow	N/A	ICP/AES, XRD, N ₂ adsorption, TPR, TEM, EDS
Pt–Au Pt–Pd Pt–Ru Pt–Fe ³⁵³	ZrO ₂	reverse micelle	methanol	flow	373–493 K	XPS, AFM, TEM, EDS
Pt–Ru ³⁵⁴	SiO ₂ TiO ₂ Al ₂ O ₃ (not specified) MgO CeO ₂ ZrO ₂	impregnation	methanol, H ₂ O	flow (liq. phase)	353 K	TEM, XPS, H ₂ chemisorption, CO chemisorption
Pt–Ru ¹⁴⁹	γ -Al ₂ O ₃	organic clusters, impregnation	ethanol, H ₂ O	flow	423 K	TEM, XPS, TPR, TPD
Pt–Re Pt–Os Pt–Fe Pt–Cu Pt–Sn Pt–Ir Pt–Co Pt–Rh Pt–Ni ³⁵⁵	C	impregnation	glycerol, H ₂ O	flow	548–573 K	CO chemisorption
Pt–Au ³⁵⁶	C	reverse micelle	glycerol, O ₂	flow	303–323 K	ICP, XRD, XPS
Pt–Ni ^{171,357}	ZSM-5 zeolite	colloid, impregnation	CH ₄ , CO ₂	flow	773 K	N ₂ adsorption, XRD, FTIR, XPS, TPR, TGA/DTA, DRIFTS, CO chemisorption
Pt–Ni ³⁵⁸	γ -Al ₂ O ₃	impregnation	CH ₄ , H ₂ O, O ₂	flow	1073 K	FTIR, XAS, CO chemisorption
Pt–Ni ³⁵⁹	zeolites	impregnation	CH ₄ , CO ₂	flow	913 K	XRD, EDS, XPS, N ₂ adsorption, TGA, TPR, SEM, TEM
Pt–Ni ¹⁷²	δ -Al ₂ O ₃	impregnation	CH ₄ , CO ₂ , H ₂ O, O ₂	flow	923 K	XRD, XPS, EDS, TGA/DTA, SEM
Pt–Ni ^{360–362}	γ -Al ₂ O ₃	reverse micelle	CH ₄ , CO ₂	flow	623–1023 K	XRD, XPS, TPR, N ₂ adsorption, TEM
Pt–Co ³⁶³	α -Al ₂ O ₃	impregnation	CH ₄ , CO ₂	flow	873–1023 K	XRD, TPR, XPS, FTIR, CO chemisorption
Pt–Rh ³⁴⁵	Ceramic monolith	impregnation	ethanol, gasoline	flow	923 K	CO chemisorption, XPS, TPO, ICP
Pt–Rh ^{346,364}	ZrO ₂	impregnation	gasoline, diesel	flow	673–1173 K	ICP-AES, TPR, N ₂ adsorption, DRIFTS, XRD, XPS, SEM, EDS, CO chemisorption
Pt–Rh ^{342,343}	γ -Al ₂ O ₃ CeO ₂	impregnation	diesel	flow (liq. phase)	673 K	N ₂ adsorption, TPD, TPR, XPS
Pt–Rh ³⁶⁵	ZrO ₂	impregnation	ethanol	flow	973 K	DRIFTS, FTIR, EDS, CO chemisorption
Pt–Ru ³⁶⁶	γ -Al ₂ O ₃	organic clusters	ethanol	flow	673–823 K	none
Pt–Ni ³⁶⁷	δ -Al ₂ O ₃	impregnation	ethanol	flow	673–823 K	none
Pt–Ni ³⁶⁸	γ -Al ₂ O ₃ La ₂ O ₃ -modified γ -Al ₂ O ₃	impregnation	glycerol	flow (liq. phase)	623 K 973 K	TPR, XPS, XRD, ICP-AES, TPO, N ₂ adsorption

catalysts were dried at higher temperatures, the transport of Re was inhibited and there were fewer bimetallic interactions, leading to lower activity.³⁴⁴

The reforming of gasoline and diesel fuels has been proposed as a short-term option of H₂ storage. Gasoline and diesel are

both currently available, and using them as a hydrogen carrier instead of direct fuels could achieve some immediate reduction in greenhouse gas emissions.³⁴⁵ Bimetallic Pt–Ni and Pt–Pd catalysts supported on alumina or ceria have been shown to be active for diesel dehydrogenation. Both bimetallic catalysts not

only improved the activity but also increased resistance to sulfur poisoning for diesel reforming. The enhanced stability of the bimetallic catalysts is due to strong metal–metal and metal–support interactions that change the electronic properties of the metals. These changes in electronic properties improve sulfur tolerance and overall catalytic performance.^{342,343}

Pt–Rh is another active bimetallic catalyst for gasoline dehydrogenation. Pt–Rh supported on a ceramic monolith was used for E85 dehydrogenation with 100% conversion at low flow rates without deactivation. At higher flow rates, the catalyst was unstable, and adding small amounts of sulfur to the feed led to irreversible deactivation due to coking. XPS studies revealed that the catalyst had a change in oxidation state after continuous time-on-stream.³⁴⁵ Pt–Rh supported on ZrO₂ was superior to both monometallic catalysts in terms of activity, selectivity, and deactivation rate for gasoline dehydrogenation. The addition of a small amount Rh to the Pt catalyst increased conversion from ~30% to ~70%.³⁴⁶

4.3. Reforming of Oxygenates

Selective reforming of oxygenates is a promising way to produce hydrogen for use in fuel cells, and syngas for production of chemicals and fuels, and in upgrading of feedstocks.^{256,258,260,347,348}

If the oxygenates are derived from renewable biomass, the reforming process is potentially CO₂ neutral, as the CO₂ byproduct can be consumed by future biomass growth. Other advantages of oxygenate reforming include low toxicity and low reactivity of the reactants, which are compatible with the current infrastructure for transportation and storage. Table 7 summarizes selected reactor studies of oxygenate reforming over supported catalysts; selected UHV studies of reforming over bimetallic surfaces are listed in Table 3.

4.3.1. Reforming of Alcohols and Polyols. **4.3.1.1. Pt–3d Bimetallic Surfaces and Catalysts.** Small oxygenates, such as methanol, ethanol, ethylene glycol, and glycerol, have been studied on 3d/Pt(111) bimetallic surfaces to determine the bond scission sequence of oxygenate molecules. The desirable reaction pathway is selective C–C bond scission, to produce H₂ and CO. DFT calculations were carried out to study the trend in the binding energies of oxygenates on bimetallic surfaces. Figure 16 shows the binding energies of methanol, methoxy, ethanol, and ethoxy on Pt(111), Ni(111), Pt–Ni–Pt(111), and Ni–Pt–Pt(111) surfaces.²⁶⁴ A nearly linear correlation between binding energy and the surface d-band center was observed, consistent with the theory of chemisorption by Hammer and Nørskov³⁰² and with the trends observed for other adsorbates in previous sections. The binding energies increase as the surface d-band center shifts closer to the Fermi level, with the Ni–Pt–Pt(111) surface showing the highest binding energies. The binding energies of molecular oxygenate species are low on all surfaces, between 3 and 12 kcal/mol. After removing the first hydrogen, the methoxy and ethoxy species adsorb more strongly to the surface, with binding energies ranging from 30 to 55 kcal/mol.

TPD measurements were carried out to monitor the reaction pathways of oxygenates on various Ni/Pt(111) bimetallic surfaces. The oxygenate molecules studied included methanol, ethanol, ethylene glycol, and glycerol.^{258,264,259} H₂ and CO were detected from TPD experiments as the main products from the four oxygenate molecules. No other product was observed with the exception of methane, which was produced after adsorption of ethanol.^{258,264} On Pt(111), methanol

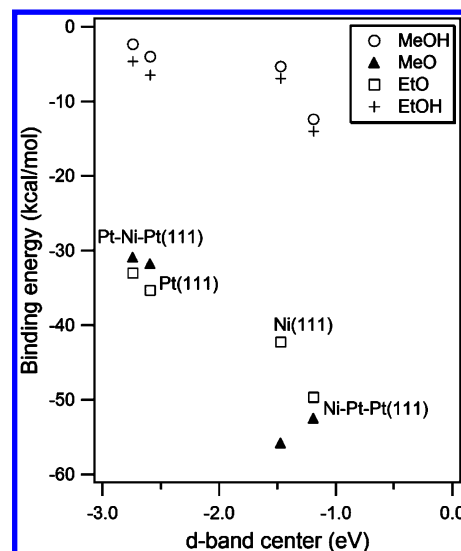


Figure 16. DFT results for binding energies of methanol, methoxy, ethanol, and ethoxy on Ni/Pt(111) bimetallic surfaces.²⁵⁶ Reproduced with permission from ref 256. Copyright 2008 Springer.

adsorbed reversibly on the surface without undergoing decomposition, consistent with previous studies.^{255,369–371} In contrast, significant amounts of H₂ and CO were produced from methanol reforming on the Ni–Pt–Pt(111) surface. On the basis of the H₂ and CO yields, the reforming activity follows the order of Pt–Ni–Pt(111) < Pt(111) < Ni(111) < Ni–Pt–Pt(111).

Similar trends in the reforming yields are observed for ethanol, ethylene glycol, and glycerol. The oxygenate reforming yields obtained experimentally are correlated with the surface d-band center in Figure 17.^{257–259} In general, the oxygenate reforming yield displays a somewhat linear correlation and increases as the surface d-band center is shifted closer to the Fermi level. It is important to point out that the trend is opposite of that observed for hydrogenation reactions on Ni/Pt(111) surfaces (Figure 11). The comparison indicates that surfaces that bind adsorbates more strongly, such as Ni–Pt–

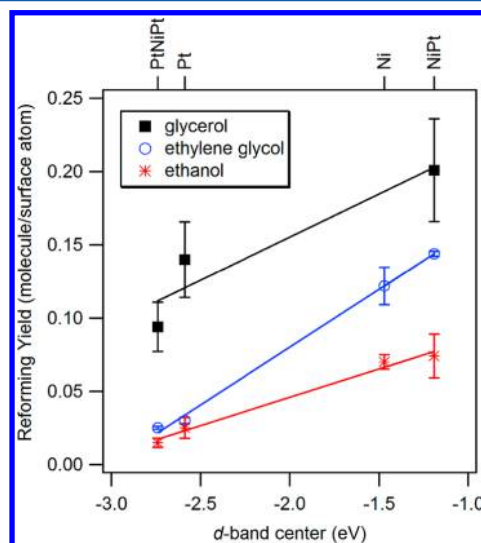


Figure 17. Reforming yields of ethanol, ethylene glycol, and glycerol versus the surface d-band center.²⁵⁶ Reproduced with permission from ref 256. Copyright 2008 Springer.

Pt(111), promote reforming reactions. One would also predict that at sufficiently high binding energies oxygenates would undergo complete decomposition instead of reforming. This is confirmed experimentally by comparing the reforming of ethanol and ethylene glycol²⁵⁷ on Fe/Pt(111), Ti/Pt(111), and Ni/Pt(111) bimetallic surfaces, where a volcano relationship is observed between reforming yield and binding energies. For example, on the Ti–Pt–Pt(111) surface the binding energies become too strong, leading to a large fraction of oxygenates undergoing complete decomposition to produce atomic carbon and oxygen instead of CO.²⁵⁷

Using reforming of methanol and ethylene glycol as probe reactions, a similar trend in reforming activity is observed on Pt–Ni surfaces prepared on a polycrystalline Pt substrate.²⁶² On both substrates the Ni–Pt–Pt bimetallic surface shows higher reforming yield than Pt–Ni–Pt, Pt, and Ni surfaces, demonstrating the possibility to bridge the materials gap between single-crystal and polycrystalline materials for reforming reactions.

Reactor studies of aqueous-phase reforming of ethylene glycol show that supported bimetallic Pt–Ni, Pt–Co, and Pt–Fe catalysts are significantly more active per gram of catalyst and have higher turnover frequencies (TOFs) for hydrogen production than monometallic Pt catalysts.³⁴⁹ As shown in Figure 18, the bimetallic catalyst with a 1:1 Pt/Ni ratio shows

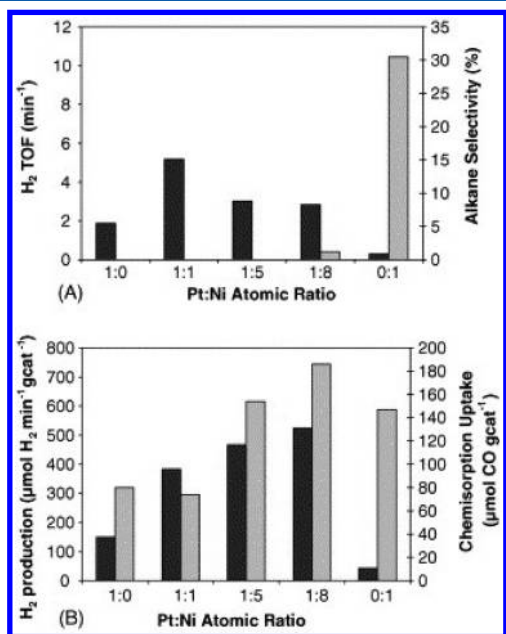


Figure 18. Fixed-bed reactor results for APR of 10 wt % ethylene glycol solutions at 483 K and 25.4 bar over Pt–Ni bimetallic catalysts. (a) TOF– H_2 (black) and alkane selectivity (gray); (b) specific H_2 production rate (black) and irreversible CO chemisorption uptake (gray).³⁴⁹ Reproduced with permission from ref 349. Copyright 2006 Springer.

the higher TOF for H_2 production. On the basis of the DFT and UHV results in Figure 17, the enhanced reforming activity observed on the Pt–Ni bimetallic catalyst can be explained by two somewhat conflicting possibilities. (1) If the structure of the supported catalyst is Pt-terminated, i.e., similar to the Pt–Ni–Pt subsurface structure, the binding of CO and hydrogen would be weaker on the Pt–Ni bimetallic catalyst than on the Pt monometallic catalyst (Figure 10a), thereby increasing the

fraction of surface sites available for reaction with ethylene glycol.³⁴⁹ (2) If the structure of the supported catalyst is transformed to Ni-terminated due to the adsorption of oxygenates, the higher reforming activity would be consistent with the UHV results of Ni–Pt–Pt(111) being more active than Pt(111) for reforming reactions (Figure 17). The exact origin of the bimetallic enhancement can only be determined by in situ measurement of the surface termination of supported Pt–Ni catalysts, such as by EXAFS under aqueous-phase reforming conditions.

Supported Pt–Ni/ γ - Al_2O_3 catalysts were also found to be effective for ethanol reforming. The catalyst was resistant to coke deposition at a ratio of water to ethanol as low as 3.0. As the amount of water was increased, the conversion and H_2 production also increased.³⁶⁶ Soyalt-Baltacıoğlu et al. agreed with these findings and found that the optimum metal loading for a Pt–Ni catalyst supported on γ - Al_2O_3 was 0.3 wt % Pt and 15 wt % Ni.³⁶⁷

4.3.1.2. Other Pt-Based Bimetallic Catalysts. Pt-based catalysts have shown activity for reforming reactions when alloyed with Ni,^{349–352} Co,³⁴⁹ Sn,³²³ Fe,^{349,353} Pd,³⁵³ Ru,^{149,348,353,354} Re,^{355,372} Au,^{353,356} and Rh.^{373,374} Selective and facile methanol reforming offers a potential option for the production of hydrogen on board vehicles powered by fuel cells. Production of on-board hydrogen is an attractive option because it allows hydrogen-containing fuels to be stored and transported in liquid form, for which there is an existing infrastructure.³⁷⁵ Methanol-reforming studies have been performed over a series of bimetallic Pt–M (M = Au, Pd, Ru, Fe) catalysts supported on ZrO_2 .³⁵³ In these studies, catalysts are prepared by micelle synthesis to mitigate the difference of size and shape, thereby attributing variations in activity to the bimetallic effect. Bimetallic catalysts outperform monometallic Pt for methanol reforming in the order of Pt–Fe > Pt–Ru > Pt–Pd > Pt–Au > Pt.³⁵³ High activity on the Pt–Fe catalysts is attributed to segregation of Fe to the surface of the nanoparticles during calcination due to the high affinity of Fe for oxygen.³⁵³ The support also plays an important role for methanol reforming. Findings by Miyao et al. show that basic oxide supports improve the selectivity of methanol reforming to CO_2 (maximizing H_2 production) whereas acidic supports suppress the catalytic activity and selectivity. The highest activity and selectivity to CO_2 are achieved over TiO_2 .³⁵⁴

Pt–Ru catalysts have been found to be more active for ethanol steam reforming than either parent metal; however, catalysts derived from organic clusters are more active than those derived from inorganic salts.¹⁴⁹ Pt–Rh bimetallic catalysts are also effective for ethanol reforming when supported on CeO_2 . Pt–Rh/ CeO_2 breaks C–H bonds before C–C bonds in ethanol;³⁷⁴ therefore, Pt–Rh could enhance H_2 production over alkane formation in ethanol reforming.³⁷³ This hypothesis has been confirmed with studies on Pt–Rh/ ZrO_2 showing that the bimetallic catalyst reaches a conversion of 100% at temperatures above 973 K, with high selectivity for H_2 formation. The bimetallic catalyst also shows improved stability over the monometallic Rh/ ZrO_2 catalyst due to less coke formation.³⁶⁵

Another option for reforming is to use glycerol, a waste product from biodiesel production. Reforming of glycerol into syngas in a flow reactor at 548 K shows an increase in H_2 , CO, CO_2 , and CH_4 concentrations upon adding Re to Pt/C catalysts.³⁴⁸ Re promotes the overall rate of glycerol reforming by reducing the binding energy of CO to Pt, which makes

surface sites more available to participate in reforming.³⁴⁸ Supported Pt–Re catalysts are also more tolerant to carbonaceous residues than supported Pt and, therefore, are less likely to deactivate rapidly.³²² The addition of Ru and Os to Pt/C catalysts has also shown to significantly increase the catalytic activity for glycerol reforming at low temperatures (548–573 K).³⁵⁵

4.3.2. Reforming of Other Oxygenates. Different from the small alcohols and polyols, the C=O functional group is also present in the ring-opened structures of C5 and C6 sugars. Glycolaldehyde,²³ the smallest molecule with both C–OH and C=O bonds as well as the same C/O ratio as the larger sugar molecules, is a good probe molecule to determine how the presence of the C=O functional group affects the reforming reaction mechanism. In the DFT study, glycolaldehyde is adsorbed on the atop sites of adjacent metal atoms. The optimized geometry on the Ni–Pt–Pt(111) surface is shown in parts a and b of Figure 19. As shown in Figure 19c,

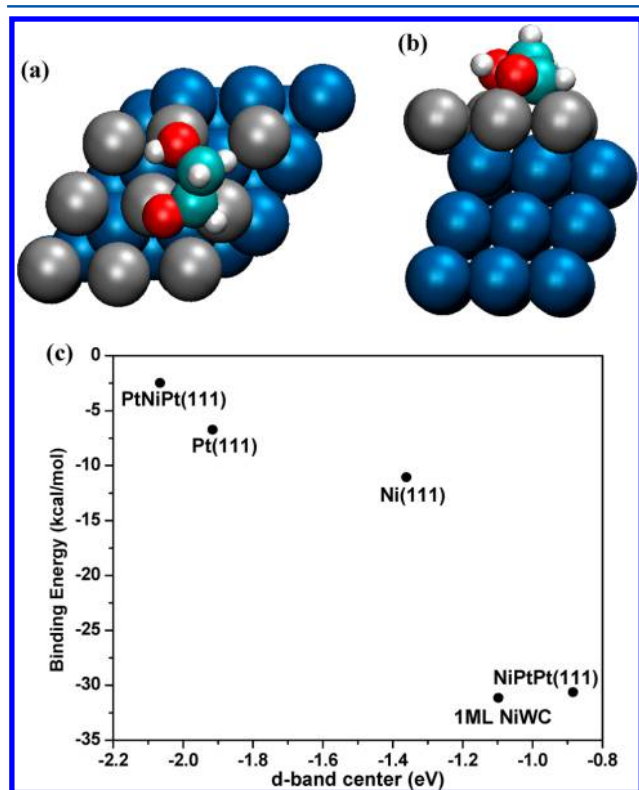


Figure 19. Top and side views of adsorption geometry of glycolaldehyde on Ni–Pt–Pt(111) and the correlation between the surface d-band center and glycolaldehyde binding energy on different surfaces²³ (Pt, blue; Ni, gray; C, aqua; O, red; H, white).

glycolaldehyde-binding energy²³ is found to increase as the surface d-band center moves closer to the Fermi level, consistent with the trend observed with small alcohols and polyols. According to glycolaldehyde TPD experiments,²³ Ni–Pt–Pt(111) shows the highest reforming activity and total activity among the Ni/Pt(111) surfaces. The activity trend found in experiments is consistent with the DFT prediction based on binding energy and surface d-band center values. On the basis of the comparison of the activity and reaction intermediates of ethylene glycol and glycolaldehyde, the presence of the C=O functionality enhances the activity on the Pt(111) surface. In contrast, for surfaces with high activity

toward O–H bond cleavage, such as the Ni–Pt–Pt(111) surface, the presence of C=O does not significantly affect the activity or reaction pathway of C2 oxygenates.²³

Figure 19c also includes the glycolaldehyde binding energy and d-band center values on monolayer Ni supported on a tungsten monocarbide (WC) surface. The similar values between the Ni–Pt–Pt(111) and Ni/WC surfaces suggest similar reforming activity for the two surfaces, which is confirmed experimentally.²³ Such a comparison points out the possibility of using WC to replace Pt in Pt-based bimetallic catalysts. More about this subject will be discussed in future research opportunities in section 5.

4.4. Other Important Catalytic Reactions

In this section we will provide an overview of several types of reactions that utilize bimetallic catalysts: CO oxidation, water gas shift (WGS) reaction, and methane conversions. At present there are few UHV studies of these reactions on Pt-based bimetallic surfaces. The overview will therefore focus primarily on reactor studies, with the anticipation that the intriguing properties of these catalysts would inspire future UHV studies to correlate model surfaces with supported catalysts. Table 8 lists selected reactor studies for each of the three reactions.

4.4.1. CO Oxidation. Preferential oxidation (PROX) of CO has received significant attention due to the demand of CO-free hydrogen for proton-exchange membrane fuel cells (PEMFCs). Su et al.²⁷¹ have performed DFT calculations of CO oxidation on surfaces of bulk Pt–Ni alloys and Pt(111). On the basis of the binding energies of adsorbed CO, O, and H, as well as the activation barriers for elemental reaction steps of CO and H oxidation, Pt-terminated Pt₃Ni(111) is identified as an optimum catalyst for CO PROX in excess of hydrogen.²⁷¹

The oxidation of CO is also studied on Fe/Pt(111), with the bimetallic surface structures being reversibly controlled between FeO/Pt(111) and subsurface Pt–Fe–Pt(111) via alternating oxidation and reduction treatments.^{207,208} The reversibility between these two structures leads to the tunability of the surface PROX activity on Fe/Pt(111).²⁰⁸ The bimetallic surface transformation study is also carried out over supported Pt–3d transition metal (3d = Co, Ni, and Cu) nanoparticles treated at alternating oxidation and reduction atmospheres, and the reversible structural changes are also observed.²⁰⁹

Guided by the formation of FeO/Pt(111) surface after the oxidation treatment of Fe/Pt(111) and its importance in controlling PROX, Yao et al.³⁹⁶ have prepared two-dimensional (2D) FeO nanoislands supported on Pt(111) surface with a well-controlled size, density, and surface structure using a two-step process. The FeO nanoislands are characterized using STM, XPS, and HREELS and are found to exhibit distinct atomic structures and electronic states from the strong interaction between FeO and the Pt(111) substrate. The coordinatively unsaturated ferrous (CUF) sites confined by crystalline matrix and on highly diluted samples are proposed to have high reactivity and stability in oxidation reactions.³⁹⁷ The confinement effect at the interface between FeO nanoislands and Pt(111) is studied by Fu et al.²⁷² for CO oxidation. An oxygen-deficient FeO_{1-x}/Pt(111) surface shows higher CO oxidation reactivity than Pt(111) and other Fe oxide overlayers, i.e., FeO_{1+x}/Pt(111) surfaces. Attempts are made to prepare the CUF active sites over supported catalysts. The Pt–Fe/SiO₂ catalyst shows significantly higher CO PROX activity than Pt/SiO₂, with the bimetallic catalyst showing CO oxidation at temperatures as low as 200 K and achieving 100% CO

Table 8. Summary of Selected Reactions over Pt-Based Bimetallic Catalysts

Oxidation Reactions						
Bimetallic Catalyst	Support	Synthesis Method	Reactants	Reactor	Temperature	Characterization Techniques
Pt-Ni ³⁷⁶	γ -Al ₂ O ₃	Impregnation	CO, O ₂ , H ₂	Flow	313 - 473 K	XRD, TPR, TPO, CO Chemisorption
Pt-Fe ²⁸⁶	SiO ₂	Impregnation	CO, Air	Flow	298 - 573 K	FTIR, XAS, TEM, H ₂ Chemisorption
Pt-Cr						
Pt-Mn						
Pt-Fe	γ -Al ₂ O ₃	Impregnation	CO, O ₂ , H ₂	Flow	350 - 500 K	XRD, TPR, TEM, CO Chemisorption, N ₂ Adsorption EDS
Pt-Co	TiO ₂					
Pt-Ni	ZrO ₂					
Pt-Cu						
Pt-Zn						
Pt-Zr ³⁷⁷						
Pt-Co ³⁷⁸	γ -Al ₂ O ₃ C	Impregnation	CO, O ₂ , H ₂	Flow	343 - 403 K	N ₂ Adsorption, XRD
Pt-Co ³⁷⁹	YSZ	Impregnation	CO, O ₂ , H ₂	Flow	340 - 520 K	TPR, TEM, N ₂ Adsorption
Pt-Co ¹⁶⁷	γ -Al ₂ O ₃	Catalyst Coating	CO, O ₂ , H ₂ H ₂ O, CO ₂	Flow	385 - 455 K	XRD, TEM, XPS, DRIFTS, ICP
Pt-Sn						
Pt-Ge						
Pt-Tl	SiO ₂	Impregnation	CO, O ₂ , H ₂	Flow	373 - 453 K	XRD, XPS, FTIR, CO Chemisorption
Pt-Cu						
Pt-Fe ³⁸⁰						
Pt-Pd ³⁸¹	CeO ₂	Impregnation	CO, O ₂ , H ₂	Flow	323 - 463 K	XRD, TEM, N ₂ Adsorption, H ₂ Chemisorption
Pt-Sn ³⁸²⁻³⁸³	AC	Impregnation	CO, O ₂	Flow	398 K	H ₂ Chemisorption, XPS, XRD, DRIFTS
Pt-Mn ³⁸⁴	γ -Al ₂ O ₃	Impregnation	CO, O ₂ , H ₂ H ₂ O, CO ₂	Flow	298 - 523 K	XRD, TPR, TPD, AAS
Pt-Ru						
Pt-Rh						
Pt-Ir	γ -Al ₂ O ₃	Core-Shell	CO, O ₂ , H ₂	Flow	298 - 473 K	FTIR, TEM, TPR, EDS, XRD
Pt-Pd						
Pt-Au ¹⁵⁶						
Pt-Re ³⁸⁵	SiO ₂	Impregnation	CO, O ₂ , H ₂	Flow	300 - 460 K	TPR, XAS, FTIR
Pt-Sn ³²⁵	CeO ₂	Impregnation	Ethanol O ₂	Flow	320 - 390 K	CO Chemisorption, TPR, DTA, XPS, N ₂ Adsorption
Water-Gas Shift						
Bimetallic Catalyst	Support	Synthesis Method	Reactants	Reactor	Temperature	Characterization Techniques
Pt-Re ³⁸⁶	CeO ₂ -ZrO ₂ mixed oxides	Impregnation	H ₂ O, CO	Flow	523 - 673 K	CO Chemisorption, TPR
Pt-Re ³⁸⁷	TiO ₂	Impregnation	H ₂ O, CO	Flow	373 K 473 K	TEM, XRD, XPS, CO Chemisorption
Pt-Au ³⁸⁸	CeO ₂	Impregnation	H ₂ O, CO	Flow	373 K 423 K	XRD, TPR, XPS, UV-Vis
Pt-Cu ³⁸⁹	CeO ₂	Impregnation	H ₂ O, CO, O ₂	Flow	473 - 773 K	XAS, TPR, N ₂ Adsorption

Table 8. continued

CH ₄ Chemistry						
Bimetallic Catalyst	Support	Synthesis Method	Reactants	Reactor	Temperature	Characterization Techniques
Pt-Co ³⁹⁰	Al ₂ O ₃ (Not Specified)	Impregnation	CH ₄	Flow	523 - 673 K 1073 K	XAS, XRD, XPS, TPR, CO Chemisorption
Pt-Ni ³⁹¹	γ-Al ₂ O ₃	Impregnation	CH ₄ , H ₂ O, O ₂	Flow	723 - 1123 K	TPR, TEM, XAS, FTIR, CO Chemisorption
Pt-Pd ³⁹²	γ-Al ₂ O ₃ ZrO ₂ Ce-ZrO ₂ YSZ	Impregnation	CH ₄ , O ₂	Flow	573 - 1173 K	XRD, ICP-AES, CO Chemisorption, N ₂ Adsorption, XRD, TPO
Pt-Re ³²⁴	Ce-ZrO ₂	Impregnation	CO ₂ , CH ₄	Flow	1073 K	CO Chemisorption, DRIFTS, TPR, TPO, XRD
Pt-Ni ³⁹³	MgAlO	Impregnation	CH ₄ , H ₂ O	Flow	1123 K	XRD, TPR, ICP, N ₂ Chemisorption, H ₂ Chemisorption
Pt-Ru ³⁹⁴⁻³⁹⁵	γ-Al ₂ O ₃ ZrO ₂ CeO ₂	Impregnation	CH ₄ , O ₂	Flow	673 - 1073 K	TPR, TPO, SEM, EDS, XRD, N ₂ Adsorption

conversion at room temperature. The highly active Pt–Fe nanocatalysts are also found to show excellent stability in a 1-KW PEMFC working system and are thus feasible for industrial application.²⁷² The interface confinement effect and enhanced CO oxidation are also confirmed for the Pt–Ni system by Mu et al.,²⁷³ where the reversible structures are identified as NiO_{1-x}/Pt–Ni–Pt(111) and NiO_{1-x}/Pt(111) surfaces. Mu et al.²⁷³ have also proposed a synergetic effect of the surface and subsurface Ni species for CO oxidation: the surface Ni oxide nanoislands activate O₂ to produce atomic O species, and the subsurface Ni atoms further enhance the elementary reaction of CO oxidation with O.

The results on model surfaces are consistent with reactor studies over supported Pt–Fe and Pt–Ni catalysts. Pt–Fe/γ-Al₂O₃, Pt–Fe₂/γ-Al₂O₃, and Pt–Fe₃/γ-Al₂O₃ outperform Pt/γ-Al₂O₃ for the PROX of CO in a combined stream of CO and H₂.³⁹⁸ Siani et al. have proposed that the increased activity for CO oxidation correlates with the extent of Pt–Fe interactions and the strength of CO adsorption.²⁸⁶ PROX of CO over supported Pt/γ-Al₂O₃ and Pt–Ni/γ-Al₂O₃ shows that the bimetallic catalyst has higher CO conversion with higher CO₂ selectivity over a wide reaction temperature range in the presence of excess hydrogen. At low temperature, increasing the molar ratio of Ni/Pt increases the catalytic activity of Pt–Ni/γ-Al₂O₃.³⁷⁷ The coimpregnated Pt–Ni/γ-Al₂O₃ catalyst exhibits a much lower reduction temperature than Pt₂Ni/γ-Al₂O₃ and Ni₂Pt/γ-Al₂O₃ prepared by sequential impregnation.³⁷⁶ Alumina is a superior support when compared with TiO₂ and ZrO₂.³⁷⁶

Pt–Co/γ-Al₂O₃ catalysts are also more active than either parent metal for CO oxidation in gas streams containing hydrogen.³⁷⁸ When supported on yttria-stabilized zirconia (YSZ), Pt–Co is highly efficient for CO PROX in a H₂-rich gas stream at temperatures below 423 K. The addition of Co to Pt/YSZ results in enhancement of catalytic performance, especially in the temperature region below 423 K. Isolated bimetallic Pt–Co nanoparticles interacting with the support seem to give rise to the high catalytic activity.³⁷⁹ Findings by

Komatsu and Tamura agree that Pt–Co/SiO₂ catalysts are more effective for PROX than either parent metal.³⁸⁰ By varying the Pt/Co atomic ratios in the catalysts, a ratio of Pt/Co = 3 is identified as the most effective for the PROX reaction.³⁸⁰

Pt–Sn/AC is active for CO oxidation when the AC support is treated with HNO₃ prior to impregnation. The acid treatment creates an acidic surface that aids in the formation of Pt–Sn alloys.³⁸³ The Pt–Sn catalyst is synthesized by sequential impregnation with high temperature reduction at 673 K. Aksoylu et al. have proposed that sequential impregnation leads to higher activity because less Pt is alloyed with Sn, making more Pt sites available for CO oxidation.³⁸² Quantum calculations by Gülmen et al. on Pt–Sn surfaces show that Pt–Sn bimetallic particles adsorb CO more weakly than Pt alone. The studies also indicate that Sn present in the subsurface configuration strengthens CO adsorption, while neighboring Sn on the surface destabilizes CO adsorption.³⁹⁹

Pt–Mn/γ-Al₂O₃ with different loadings of Mn is active for partial oxidation of CO. TPR results indicate that Pt promotes the reduction of Mn to a greater extent and at lower temperatures than monometallic Mn. Catalysts with low Mn content show no improvement in catalytic activity, but CO oxidation activity increases dramatically in catalysts with compositions of Mn above 8 wt %. In the presence of CO₂, catalytic activity increases and CO conversion reaches 100% for the 15 wt % Mn, Pt–Mn/γ-Al₂O₃ catalyst. The addition of H₂O to the feed stream significantly decreases catalytic activity, possibly due to steam poisoning of oxygen vacancies in MnO_x.³⁸⁴

Other metals, such as Pd,³⁸¹ Ru,⁴⁰⁰ and Re,³⁸⁵ are active when alloyed with Pt for CO oxidation. Pt–Pd/CeO₂,³⁸¹ Pt–Ru/SiO₂,⁴⁰⁰ and Pt–Re/SiO₂³⁸⁵ all demonstrate enhanced PROX activity over the corresponding monometallic catalysts. For the latter catalyst, EXAFS analysis confirms the existence of Pt–Re bimetallic bonds. The synergistic effect occurs when the reduced Pt–Re bimetallic particles dissociate O₂, which then spills over to the Pt particles to oxidize CO.³⁸⁵

4.4.2. Water Gas Shift Reaction. Water gas shift (WGS) is an important reaction typically used during and after reforming to increase the yield of H_2 . CO is oxidized by H_2O to produce an additional mole of H_2 with CO_2 as a waste gas. Pt-based bimetallic catalysts are active for the WGS reaction and show enhanced activity when alloyed with Re,^{386,387} Co,³⁸⁶ and Au.³⁸⁸ The alloyed metal and dispersion have been found to play an important role in the activity of WGS. In comparing a series of Pt-based bimetallic catalysts over $\gamma-Al_2O_3$ and TiO_2 , catalysts containing Pt–Re and Pt–Co exhibit a higher WGS activity than Pt, but Pt–Mo, Pt–Sn, and Pt–Cu show a lower WGS activity. Reports by Choung et al. show that Pt–Re catalysts display higher activity because Re increases Pt dispersion on TiO_2 and $\gamma-Al_2O_3$.³⁸⁶ Sato et al. report that the WGS activity over Pt–Re/ TiO_2 exhibits a mild dependence on Re content and a strong dependence on reduction temperature.³⁸⁷ Additional Re increases the amount of Re on the catalyst surface and leads to an increase in the rate of WGS.³⁸⁷

Although the metals used for WGS play an important role, the support often participates in the WGS chemistry. For example, adding Pt to a Au/ CeO_2 catalyst is much more active for WGS than either parent metal. The introduction of Pt to the Au catalyst leads to the formation of a partially oxidized gold species. The presence of Au and Pt also help keep ceria in a Ce^{3+} state, which creates oxygen vacancies and aids in the overall activity of the catalyst.³⁸⁸

Kugai et al. examine the enhancement of water gas shift by the addition of oxygen to the feed stream (OWGS). Pt–Cu/ CeO_2 exhibits higher OWGS activity than monometallic catalysts, but the higher activity is not as pronounced in traditional WGS.³⁸⁹ The addition of oxygen to the reaction is suggested to both lower the CO surface coverage and increase the number of available surface sites to participate in the reaction. Another possible explanation is that supported Pt–Cu bimetallic catalysts are reduced more easily than the corresponding monometallic catalysts.

4.4.3. CH_4 Conversion. The large abundance of natural gas makes methane an attractive feedstock for use in hydrogen production, in the synthesis of more complex molecules, and as a direct fuel.²⁸⁹ Pt–Co catalysts have been shown to convert methane into C_2+ products with higher conversion than the corresponding monometallic catalysts.³⁹⁰ The enhanced activity of the bimetallic system can be explained by increased reducibility of Co and facilitated chain-growth by Co from partially dehydrogenated species produced on Pt.³⁹⁰

For CH_4 to be used as a direct fuel, it must be fully combusted to CO_2 and H_2O to reduce environmental impacts, mainly because CH_4 is a greenhouse gas that has an even greater global-warming potential than CO_2 .⁴⁰¹ Studies on catalytic combustion of CH_4 over Pt–Pd catalysts show that the bimetallic outperforms monometallic Pd catalysts independent of the catalyst support.^{392,402} The metal particles in Pt–Pd/ $\gamma-Al_2O_3$ consist of two phases: a PdO phase and a Pt and Pd alloy.^{392,402} Castellazzi et al. have found that the effect of Pt on PdO for CH_4 combustion depends on several factors such as the extent of PdO bond formation and the strength of the Pd–support interaction.⁴⁰³

The recent discovery of large natural gas reservoirs has increased efforts in finding efficient processes to partially oxidize CH_4 into CO and H_2 . Lanza et al. have found that Pt–Ru is an active metal combination for CH_4 partial oxidation because Pt activates CH_4 at low temperature and Ru is selective toward H_2 and CO. The bimetallic catalyst begins to show

oxidation activity at 823 K for Pt–Ru versus 903 K for the monometallic Ru catalyst. Above ~ 800 K, syngas at a H_2/CO ratio of 2 is produced as the favored product.^{394,395} DFT and experimental results show that Pt–Ru core–shell nanoparticles have a weaker CO binding energy than monometallic Pt nanoparticles, leading to lower CO coverage and higher activity.¹⁵⁶

Pt–Ni³⁹¹ catalysts have also been evaluated for the partial oxidation of CH_4 . Small amounts of Pt are added to the Ni catalyst to reduce the extent of Ni oxidation. In this case, the high reducibility of Pt and the high activity of Ni are both utilized. Introduction of Pt to Ni catalysts by sequential impregnation enhances the catalytic performance by keeping Ni reduced in the presence of oxygen.³⁹¹ Characterization by TEM, TPR, EXAFS, and FTIR suggest that the catalysts prepared by sequential impregnation are mostly Pt-terminated while catalysts prepared by coimpregnation do not show increased amounts of surface Pt. The lack of surface Pt in the coimpregnated catalyst may lead to rapid deactivation from the oxidation of Ni, possibly explaining the decreased activity.

Steam reforming of CH_4 encounters problems of coking and fast deactivation of catalysts.⁴⁰⁴ However, research groups have found that Pt–Ni is an effective catalyst for reforming of CH_4 .^{172,358,360–362} For example, Pt–Ni supported on $MgAl_2O_4$ exhibits self-activation and self-regeneration characteristics.³⁹³ Without prereduction, the Pt–Ni bimetallic catalyst dissociates CH_4 under reaction conditions to form hydrogen, which spills over and reduces other metallic particles on the catalyst. The addition of Pt to the Ni/ $MgAl_2O_4$ catalyst also prevents deactivation by helping the alloyed Ni rereduce from Ni^{2+} to Ni^0 . At increased Ni loading the self-activation and self-regeneration characteristics are no longer present.³⁹³

Dry reforming of methane is an attractive process because it utilizes two abundant, cheap compounds as a hydrogen source; however, the process requires high temperatures, and the catalyst deactivates quickly due to coking. Pinheiro et al. show that Pt–Ni supported on polytype A of beta-zeolite (BEA) zeolites has superior activity and stability for dry reforming of methane, compared with $\gamma-Al_2O_3$ and AC supports, due to its high resistance to coking.³⁵⁹ These findings are confirmed by Arishtirova et al., who find that the addition of Pt to Ni catalysts supported on a NaZSM-5 zeolite leads to better reducibility of the catalyst, higher Ni dispersion, and increased activity and stability for CH_4 reforming by CO_2 .³⁵⁷ In addition, Pt–Re³⁴⁵ supported on ceria–zirconia mixed oxides shows enhanced dry reforming activity. The Pt–Re interaction reduces coke deposition, improves Pt dispersion, and significantly enhances selectivity and stability, while oxygen exchange of the reactants is facilitated by the reducible support.

4.5. Brief Summary of Pt-Based Bimetallic Electrocatalysts

Pt-based bimetallic catalysts are widely utilized for both anodic and cathodic reactions in low-temperature fuel cells, in particular PEMFCs. For example, Pt–Ru and Pt–Rh based catalysts are promising anode catalysts for the electrooxidation of methanol⁴⁰⁵ and ethanol,⁴⁰⁶ respectively. Pt–3d alloys have been extensively studied as cathode catalysts for the oxygen reduction reaction (ORR). Similar to that described for the hydrogenation reaction in section 4.1, the subsurface Pt–3d–Pt structures are preferred for the ORR reaction due to optimized binding with atomic oxygen and hydroxyl groups. One of the challenges is to prevent the segregation of subsurface 3d metals to the surface, which is thermodynamically favorable in the

presence of adsorbed oxygen, as described in section 3.1. The topic of electrocatalysts is beyond the scope of the current review; however, the basic principles, synthesis methods, and characterization techniques in the current review share many common themes with Pt-based bimetallic electrocatalysts. Interested readers can refer to several recent reviews on bimetallic electrocatalysts.^{405,407,408}

4.6. Brief Summary of Trimetallic Catalysts

Some recent studies show that trimetallic catalysts exhibit better performance than both monometallic and bimetallic systems. For example, Epron et al.⁴⁰⁹ have studied *n*-heptane reforming on Pt–Sn and Pt–Ir–Sn/Al₂O₃ catalysts and find that the addition of Sn to the bimetallic Pt–Ir increases the stability of the catalysts and also the selectivity toward toluene. Compared with Pt–Sn bimetallic catalysts, less Sn is needed in Pt–Ir–Sn trimetallic catalyst to obtain the same toluene yield. Aranishi et al.⁴¹⁰ have synthesized the Au/Co/Fe triple-layered core–shell nanoparticles that exhibit much higher catalytic activities for hydrolytic dehydrogenation of ammonia borane than the corresponding monometallic (Au, Co, Fe) or bimetallic (AuCo, AuFe, CoFe) catalysts. Pd/Ag/Rh trimetallic nanoparticles have been synthesized and exhibit high hydrogenation activity of methyl acrylate at an atomic composition of Pd/Ag/Rh = 1/2/13.5 and an average diameter of 2.2 nm.⁴¹¹ The mechanism of the promoted reactivity in trimetallic catalysts has also been investigated. For example, Fang et al.⁴¹² have studied the electrooxidation of formic acid on Au@Pd@Pt NPs and find a synergistic effect between the three different nanostructure components (sphere, shell, and islands). Using FePtAu nanoparticles as an example, Zhang et al.⁴¹³ demonstrate that the presence of Au in FePtAu facilitates FePt structure transformation from chemically disordered face-centered cubic (fcc) structure to chemically ordered face-centered tetragonal (fct) structure.

5. CONCLUSIONS AND FUTURE RESEARCH OPPORTUNITIES

The examples in the current review illustrate the unique catalytic properties of bimetallic surfaces and catalysts. Several examples, such as the hydrogenation of C=C and C=O bonds over Pt–3d bimetallic materials, also demonstrate a strong correlation between model surfaces and supported catalysts, showing the promise of designing catalysts using first principles on model surfaces. The main reason for such strong correlations is that the desirable bimetallic structures for hydrogenation reactions, with subsurface 3d atoms underneath the surface Pt layer, are thermodynamically stable both in UHV environment and under hydrogenation reaction conditions.

In comparison, for other types of reactions, such as dehydrogenation and reforming, the desirable Pt–3d bimetallic structures should be the 3d-terminated surfaces. However, it is less clear whether these structures are present under dehydrogenation and reforming reaction conditions. Similarly, more studies are needed to determine the structures and their stability in other Pt-based bimetallic catalysts. Such understanding is critical in extending the design of bimetallic catalysts from hydrogenation to other types of reactions. Below are some opportunities for future research in the area of bimetallic catalysts:

- (1) *Characterization of bimetallic catalysts under in situ reaction conditions.* Because bimetallic structures would most likely change during reactions, it is critical to identify the

atomic arrangement of bimetallic catalysts under temperatures, pressures, and reaction media (vapor phase or aqueous phase) relevant to catalytic reactions. One promising in situ technique is EXAFS, which allows measurements of the coordination numbers of monometallic and bimetallic bonds under in situ conditions. Recently in situ EXAFS and XRD have been combined to determine the short-range bonding environment of metal catalysts and the long-range order of oxide supports, respectively, under reaction conditions.^{414,415} These techniques should provide important information on the bimetallic structures and their stability under reaction conditions, which would in turn provide critical input for constructing relevant model surfaces in DFT calculations and UHV studies. To truly achieve the rational design of catalysts from first principles, it is essential that the model systems are as close as possible to those under reaction conditions. This is especially true for bimetallic catalysts due to the adsorbate-induced segregation and diffusion of metal atoms.

- (2) *Synthesis of stable bimetallic structures.* The prevention of metal segregation and diffusion is a challenge under reaction conditions. For example, for the Pt–3d bimetallic catalysts, ideally one would design Pt-terminated surfaces for hydrogenation reactions and 3d-terminated catalysts for reforming reactions. Although the synthesis of well-defined core–shell bimetallic catalysts has been demonstrated for Pt–3d bimetallic electrocatalysts,⁴⁰⁷ it is unlikely that such well-defined core–shell structures, in particular the maintenance of Pt or 3d as the surface atoms, would survive the relatively harsh conditions of calcination and reduction treatment in typical heterogeneous catalysis. One possibility to prevent the metal movement is to increase the activation barriers of segregation/diffusion by anchoring one or both metal atoms by the catalyst supports, although the strong metal–support interaction might change the electronic and catalytic properties of the bimetallic catalysts.
- (3) *Metal carbides as substrates in bimetallic catalysts.* Another possibility is to replace Pt with a metal-like substrate that prevents the diffusion of the 3d metals. For example, Ni-terminated Pt–Ni surfaces are identified as effective catalysts for the reforming of alcohols and polyols. However, under reduction conditions or higher temperatures the surface Ni atoms would diffuse into bulk Pt, losing the high reforming activity. Recently, tungsten carbide (WC) was utilized to replace Pt because WC often shows catalytic properties similar to Pt⁴¹⁶ and is an effective diffusion barrier layer for surface metal atoms.⁴¹⁷ A comparative DFT and UHV study confirms that monolayer Ni–Pt and Ni–WC surfaces show nearly identical reforming activity for ethanol.²⁶¹ A recent study also demonstrates that other carbides, including W₂C and Mo₂C, can be used to replace Pt to support monolayer metals.^{418–421} Synthesis efforts to extend these model surfaces to powder catalysts will lead to the production of alternative bimetallic catalysts with higher stability and lower cost.
- (4) *Correlation between model systems and catalytic reactions through theory.* In addition to experimental efforts, calculations through multiscale modeling offer additional

opportunities to correlate results on model surfaces to catalytic performance over supported catalysts. For example, recently Vlachos and co-workers have demonstrated the feasibility of creating activity maps to predict catalytic activity and selectivity of several Pt-based bimetallic catalysts using a combination of DFT calculations, linear energy correlations, and microkinetic modeling.^{252,422,423} These types of calculations, coupled with parallel experimental efforts, will offer fruitful opportunities for the rational design of bimetallic catalysts with desirable activity, selectivity, and stability.

AUTHOR INFORMATION

Corresponding Author

*E-mail: jgchen@udel.edu.

Notes

The authors declare no competing financial interest.

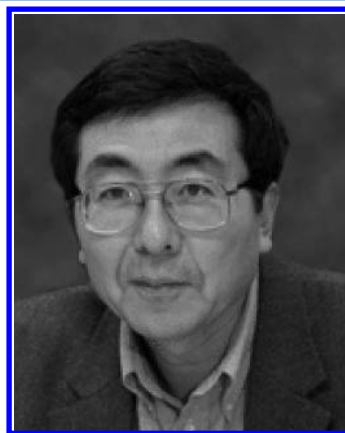
Biographies



Weiting Yu received her bachelor's degree in chemical engineering from Zhejiang University in 2008. She joined the Department of Chemical Engineering at the University of Delaware the following fall and is currently in her fourth year. She is co-advised by Dr. Jingguang G. Chen and Dr. Mark A. Barteau. Her thesis is exploring catalytic conversion of biomass derivatives with topics of interest including catalysis, surface science, and renewable energy such as biomass.



Marc Porosoff received his B.S. in 2009 and M.S. in 2010, both in Chemical Engineering from the Johns Hopkins University. He is currently working on his Ph.D. in Chemical Engineering at the University of Delaware. His research interests relate to alternative energy technologies through applications of supported bimetallic catalysts.



Dr. Jingguang Chen is a professor of Chemical Engineering at Columbia University. He started his career at the Exxon Corporate Research Laboratories before joining the faculty at the University of Delaware. His current research activities include experimental and theoretical studies aimed at the utilization of carbide and bimetallic materials in catalysis and electrocatalysis.

ACKNOWLEDGMENTS

The authors acknowledge support from the Catalysis Center for Energy Innovation, an Energy Frontier Research Center funded by the U.S. Department of Energy, Office of Science, Office of Basic Energy Sciences under Award Number DE-SC0001004.

DEDICATION

This review is dedicated to the memory of the late Professor Wayne Goodman, who was a pioneer in applying surface science techniques to study bimetallic surfaces and model catalysts.

LIST OF ABBREVIATIONS

$\Delta\Phi$	work-function change
2D	2-dimensional
3D	3-dimensional
3d	3d-metal
AAS	atomic absorption spectroscopy
AC	activated carbon
AES	Auger electron spectroscopy
AFM	atomic force microscopy
ALISS	alkali ion scattering spectroscopy
ATR-IR	attenuated total reflectance infrared
BEP	Brønsted–Evans–Polanyi
BF	bright field
BFS	Bozzolo, Ferrante, and Smith
CAICIS	coaxial impact collision ion scattering spectroscopy
CNF	carbon nanofibers
CNT	carbon nanotubes
CO	carbon monoxide
colloid	colloidal synthesis
core–shell	core–shell synthesis
CUF	coordinatively unsaturated ferrous
CV	cyclic voltammetry
DF	dark field
DFT	density functional theory
DRIFTS	diffuse reflectance infrared Fourier transform spectroscopy
EDS	energy-dispersive X-ray spectroscopy

E _{seg}	segregation energy
EXAFS	extended X-ray absorption fine structure
FEM	field emission microscopy
FTIR	Fourier transform infrared spectroscopy
FTIRAS	Fourier transform infrared absorption–reflection (FTIRA) spectroscopy
HAADF	high annular dark field
HAS	helium atom scattering
HBE	hydrogen-binding energy
HDO	hydrodeoxygenation
HREELS	high-resolution electron energy loss spectroscopy
ICP-AES/OES	inductively coupled plasma atomic/optical emission spectroscopy
IR	infrared
IRAS	infrared reflection absorption spectroscopy
IS	ionization spectroscopy
KMCS	kinetic Monte Carlo simulation
LEED	low-energy electron diffraction
LEEM	low-energy electron microscopy
LEIS	low-energy ion scattering
MA	maleic anhydride
MAPR	microwave-assisted polyol reduction
MCS	Monte Carlo simulations
MD	molecular dynamics
MEIS	medium-energy ion scattering
NEXAFS	near-edge X-ray absorption fine structure
ORR	oxygen reduction reaction
OWGS	oxygen-enhanced water gas shift
PAA	polyacrylic acid
PAX	photoemission of adsorbed xenon
PEMFCs	proton-exchange membrane fuel cells
PES	photoemission spectroscopy
PROX	preferential oxidation
PVD	physical vapor deposition
SEM	scanning electron microscopy
SMOKE	surface magneto-optical Kerr effect
STEM	scanning transmission electron microscopy
STM	scanning tunneling microscopy
SXPS	soft X-ray photoelectron spectroscopy
SXS	surface X-ray scattering
TCD	thermal conductivity detector
TDS	thermal desorption spectroscopy
TEAS	thermal energy He atom scattering
TEM	transmission electron microscopy
TGA/DTA	thermogravimetric analysis/differential thermal analysis
TOF	turnover frequency
TOF-SIMS	time-of-flight secondary ion mass spectroscopy
TPD	temperature-programmed desorption
TPO	temperature-programmed oxidation
TPR	temperature-programmed reduction
UHV	ultrahigh vacuum
UPS	ultraviolet photoemission spectroscopy
UV–vis DRS	ultraviolet–visible diffuse reflectance spectroscopy
WC	tungsten monocarbide or tungsten carbide
WGS	water gas shift
XAES	X-ray excited Auger electron spectroscopy
XANES	X-ray absorption near-edge structure
XAS	X-ray absorption spectroscopy
XPS	X-ray photoelectron spectroscopy
XRD	X-ray diffraction

YSZ yttria-stabilized zirconia

REFERENCES

- (1) Sinfelt, J. H. *Acc. Chem. Res.* **1977**, *10*, 15.
- (2) Sinfelt, J. H. *Bimetallic Catalysts: Discoveries, Concepts and Applications*; John Wiley and Sons: New York, 1983.
- (3) Sinfelt, J. H.; Barnett, A. E.; Dembinski, G. W. U.S. patent, US3442973, 1969.
- (4) Bartholomew, C. H.; Farrauto, R. J. *Fundamentals of industrial catalytic processes*; Wiley Interscience: Hoboken, NJ, 2006.
- (5) Stamenkovic, V. R.; Fowler, B.; Mun, B. S.; Wang, G. F.; Ross, P. N.; Lucas, C. A.; Markovic, N. M. *Science* **2007**, *315*, 493.
- (6) Zhang, J.; Sasaki, K.; Sutter, E.; Adzic, R. R. *Science* **2007**, *315*, 220.
- (7) Campbell, C. T. *Annu. Rev. Phys. Chem.* **1990**, *41*, 775.
- (8) Rodriguez, J. A. *Surf. Sci. Rep.* **1996**, *24*, 225.
- (9) Madey, T. E.; Nien, C.-H.; Pelhos, K.; Kolodziej, J. J.; Abdelrehim, I. M.; Tao, H.-S. *Surf. Sci.* **1999**, *438*, 191.
- (10) Chen, J. G.; Menning, C. A.; Zellner, M. B. *Surf. Sci. Rep.* **2008**, *63*, 201.
- (11) Goodman, D. W. *Ultramicroscopy* **1990**, *34*, 1.
- (12) Greeley, J.; Mavrikakis, M. *Nat. Mater.* **2004**, *3*, 810.
- (13) Hammer, B.; Morikawa, Y.; Norskov, J. K. *Phys. Rev. Lett.* **1996**, *76*, 2141.
- (14) Hansgen, D. A.; Vlachos, D. G.; Chen, J. G. *Nat. Chem.* **2011**, *2*, 484.
- (15) Hwu, H. H.; Eng, J.; Chen, J. G. *J. Am. Chem. Soc.* **2002**, *124*, 702.
- (16) Kitchin, J. R.; Norskov, J. K.; Barteau, M. A.; Chen, J. G. *Phys. Rev. Lett.* **2004**, *93*.
- (17) Murillo, L. E.; Goda, A. M.; Chen, J. G. *J. Am. Chem. Soc.* **2007**, *129*, 7101.
- (18) Neurock, M.; van Santen, R. A. *J. Phys. Chem. B* **2000**, *104*, 11127.
- (19) Pallassana, V.; Neurock, M.; Hansen, L. B.; Hammer, B.; Norskov, J. K. *Phys. Rev. B: Condens. Matter.* **1999**, *60*, 6146.
- (20) Rodriguez, J. A.; Goodman, D. W. *J. Phys. Chem.* **1991**, *95*, 4196.
- (21) Rodriguez, J. A.; Goodman, D. W. *Science* **1992**, *257*, 897.
- (22) Saliccioli, M.; Yu, W. T.; Barteau, M. A.; Chen, J. G.; Vlachos, D. G. *J. Am. Chem. Soc.* **2011**, *133*, 7996.
- (23) Yu, W. T.; Barteau, M. A.; Chen, J. G. *J. Am. Chem. Soc.* **2011**, *133*, 20528.
- (24) Jiang, H. L.; Xu, Q. *J. Mater. Chem.* **2011**, *21*, 13705.
- (25) Wang, A. Q.; Chang, C. M.; Mou, C. Y. *J. Phys. Chem. B* **2005**, *109*, 18860.
- (26) Zhang, Y. W.; Huang, W. Y.; Habas, S. E.; Kuhn, J. N.; Grass, M. E.; Yamada, Y.; Yang, P.; Somorjai, G. A. *J. Phys. Chem. C* **2008**, *112*, 12092.
- (27) Humbert, M. P.; Chen, J. G. *J. Catal.* **2008**, *257*, 297.
- (28) Kitchin, J. R.; Khan, N. A.; Barteau, M. A.; Chen, J. G.; Yakshinskiy, B.; Madey, T. E. *Surf. Sci.* **2003**, *544*, 295.
- (29) O'Connor, D. J.; Sexton, B. A.; Smart, R. C. *Surface analysis methods in materials science*, 2nd ed.; Springer: New York, 2003.
- (30) Masel, R. I. *Principles of adsorption and reaction on solid surfaces*; John Wiley and Sons, Inc.: New York, 1996.
- (31) Pendry, J. B. *Low Energy Electron Diffraction*; Academic Press: New York, 1974.
- (32) Gauthier, Y. *Surf. Rev. Lett.* **1996**, *3*, 1663.
- (33) Menning, C. A.; Chen, J. G. *J. Chem. Phys.* **2008**, *128*.
- (34) Cabeza, G. F.; Castellani, N. J.; Legare, P. J. *Phys. Chem. Solids* **2006**, *67*, 690.
- (35) Goyhenex, C.; Bulou, H.; Deville, J. P.; Treglia, G. *Phys. Rev. B: Condens. Matter.* **1999**, *60*, 2781.
- (36) Walker, M.; Parkinson, C. R.; Draxler, M.; McConville, C. F. *Surf. Sci.* **2005**, *584*, 153.
- (37) AlShamaileh, E.; Younis, H.; Barnes, C. J.; Pussi, K.; Lindroos, M. *Surf. Sci.* **2002**, *515*, 94.
- (38) AlShamaileh, E.; Barnes, C. J.; Wander, A. J. *Phys.: Condens. Matter.* **2003**, *15*, 1879.

- (39) AlShamaileh, E.; Pussi, K.; Younis, H.; Barnes, C.; Lindroos, M. *Surf. Sci.* **2004**, *548*, 231.
- (40) Belkhou, R.; Thiele, J.; Guillot, C. *Surf. Sci.* **1997**, *377*, 948.
- (41) Reilly, J. P.; O'Connell, D.; Barnes, C. J. *J. Phys.: Condens. Matter.* **1999**, *11*, 8417.
- (42) Demarco, G.; Garces, J. E.; Bozzolo, G. *Surf. Sci.* **2003**, *526*, 309.
- (43) Christensen, A.; Ruban, A.; Stoltze, P.; Jacobsen, K. W.; Skriver, H. L.; Norskov, J. K. *Phys. Rev. B* **1997**, *56*, 5822.
- (44) Boo, J. B.; Lee, S. B.; Linke, R.; Becker, C.; Schroder, U.; Wandelt, K. *J. Korean Phys. Soc.* **1999**, *35*, S582.
- (45) Boo, J. H.; Lee, S. Y.; Lee, S. B.; Kwak, H. T.; Schroder, U.; Linke, R.; Wandelt, K. *J. Korean Phys. Soc.* **1999**, *35*, S554.
- (46) Barrett, N. T.; Belkhou, R.; Thiele, J.; Guillot, C. *Surf. Sci.* **1995**, *333*, 776.
- (47) Shen, Y. G.; O'Connor, D. J.; MacDonald, R. J. *Nucl. Instrum. Methods Phys. Res., Sect. B* **1998**, *135*, 361.
- (48) Dastoor, P. C.; O'Connor, D. J.; MacLaren, D. A.; Allison, W.; Noakes, T. C. Q.; Bailey, P. *Surf. Sci.* **2005**, *588*, 101.
- (49) Shen, Y. G.; O'Connor, D. J.; King, B. V.; MacDonald, R. J. *Nucl. Instrum. Methods Phys. Res., Sect. B* **1996**, *115*, 191.
- (50) Shen, Y. G.; O'Connor, D. J.; Wandelt, K.; MacDonald, R. J. *Surf. Sci.* **1996**, *358*, 921.
- (51) Sadek, M. M.; Wang, L. C. *J. Phys. Chem. A* **2006**, *110*, 14036.
- (52) Egawa, C.; Endo, S.; Iwai, H.; Oki, S. *Surf. Sci.* **2001**, *474*, 14.
- (53) Khan, N. A.; Zellner, M. B.; Chen, J. G. *Surf. Sci.* **2004**, *556*, 87.
- (54) Khan, N. A.; Zellner, M. B.; Murillo, L. E.; Chen, J. G. *Catal. Lett.* **2004**, *95*, 1.
- (55) Castellani, N. J.; Legare, P.; Demangeat, C.; Pick, S. *Surf. Sci.* **1996**, *352–354*, 148.
- (56) Radosavkic, D.; Belkhou, R.; Thiele, J.; Barrett, N.; Guillot, C. *J. Phys. IV* **1996**, *6*, 201.
- (57) Radosavkic, D.; Thiele, J.; Barrett, N.; Guillot, C.; Belkhou, R. *Surf. Sci.* **1997**, *377*, 168.
- (58) Wilson, K.; Brake, J.; Lee, A. F.; Lambert, R. M. *Surf. Sci.* **1997**, *387*, 257.
- (59) Vermang, B.; Juel, M.; Raaen, S. *Phys. Rev. B: Condens. Matter.* **2006**, *73*.
- (60) Khan, N. A.; Murillo, L. E.; Chen, J. G. *J. Phys. Chem. B* **2004**, *108*, 15748.
- (61) Tsay, J. S.; Shern, C. S. *Surf. Sci.* **1998**, *396*, 313.
- (62) Shern, C. S.; Tsay, J. S.; Her, H. Y.; Wu, Y. E.; Chen, R. H. *Surf. Sci.* **1999**, *429*, L497.
- (63) Tsay, J. S.; Chern, C. S. *Surf. Sci.* **1998**, *396*, 319.
- (64) Menning, C. A.; Hwu, H. H.; Chen, J. G. *J. Phys. Chem. B* **2006**, *110*, 15471.
- (65) Lundgren, E.; Leonardelli, G.; Schmid, M.; Varga, P. *Surf. Sci.* **2002**, *498*, 257.
- (66) Atrei, A.; Bardi, U.; Galeotti, M.; Roviola, G.; Torrini, M.; Zanazzi, E. *Surf. Sci.* **1995**, *339*, 323.
- (67) Lamas, E. J.; Balbuena, P. B. *J. Chem. Theory Comput.* **2006**, *2*, 1388.
- (68) Kitchin, J. R.; Norskov, J. K.; Barteau, M. A.; Chen, J. G. *J. Chem. Phys.* **2004**, *120*, 10240.
- (69) Kim, J.; Lee, J. W.; Jeong, J. R.; Shin, S. C.; Ha, Y. H.; Park, Y.; Moon, D. W. *Phys. Rev. B: Condens. Matter.* **2002**, *65*.
- (70) Moon, D. W.; Ha, Y. H.; Park, Y.; Lee, J. W.; Kim, J.; Shin, S. C. *Appl. Phys. Lett.* **2001**, *79*, 503.
- (71) Vasylyev, M. A.; Tinkov, V. A.; Blaschuk, A. G.; Luyten, J.; Creemers, C. *Appl. Surf. Sci.* **2006**, *253*, 1081.
- (72) Radnik, J.; Wagner, B. D.; Oster, K.; Wandelt, K. *Surf. Sci.* **1996**, *358*, 943.
- (73) Holst, B.; Nohlen, M.; Wandelt, K.; Allison, W. *Surf. Sci.* **1997**, *377–379*, 891.
- (74) Colen, R. E. R.; Kolodziejczyk, M.; Delmon, B.; Block, J. H. *Surf. Sci.* **1998**, *412–413*, 447.
- (75) Tsay, J. S.; Mangen, T.; Wandelt, K. *Thin Solid Films* **2001**, *397*, 152.
- (76) O'Connor, D. J.; MacLaren, D. A.; Noakes, T. C. Q.; Bailey, P.; Allison, W.; Dastoor, P. C. *Vacuum* **2004**, *73*, 115.
- (77) Hamad, B. A.; Khalifeh, J. M.; Demangeat, C. *Surf. Sci.* **2003**, *542*, 230.
- (78) Zhang, L. P.; van Ek, J.; Diebold, U. *Phys. Rev. B: Condens. Matter.* **1998**, *57*, R4285.
- (79) Bastl, Z.; Pick, S. *Surf. Sci.* **2004**, *566–568*, 832.
- (80) Davis, D. J.; Kyriakou, G.; Lambert, R. M. *J. Phys. Chem. B* **2006**, *110*, 11958.
- (81) Jerdev, D. I.; Koel, B. E. *Surf. Sci.* **2002**, *513*, L391.
- (82) Lee, T. Y.; Sarbach, S.; Kuhnke, K.; Kern, K. *Surf. Sci.* **2006**, *600*, 3266.
- (83) Ramstad, A.; Raaen, S. *Phys. Rev. B: Condens. Matter.* **1999**, *59*, 15935.
- (84) Ramstad, A.; Raaen, S.; Barrett, N. *Surf. Sci.* **2000**, *448*, 179.
- (85) Yeh, C.-C.; Lai, Y.-H.; Chu, W.-Y.; Yeh, C.-T.; Hung, W.-H. *Surf. Sci.* **2004**, *565*, 81.
- (86) Bassett, D. W. *Surf. Sci.* **1995**, *325*, 121.
- (87) Pourovskii, L. V.; Ruban, A. V.; Abrikosov, I. A.; Vekilov, Y. K.; Johansson, B. *Phys. Rev. B: Condens. Matter.* **2001**, *6403*.
- (88) Khan, N. A.; Hwu, H. H.; Chen, J. G. *J. Catal.* **2002**, *205*, 259.
- (89) Fruhberger, B.; Eng, J.; Chen, J. G. *Catal. Lett.* **1997**, *45*, 85.
- (90) Su, C. W.; Ho, H. Y.; Shern, C. S.; Chen, R. H. *Surf. Sci.* **2002**, *499*, 103.
- (91) Habar, M.; Stauffer, L.; Wille, L. T.; Dreyse, H. *Surf. Sci.* **2003**, *532–535*, 53.
- (92) Goda, A. M.; Barteau, M. A.; Chen, J. G. *J. Phys. Chem. B* **2006**, *110*, 11823.
- (93) Gambardella, P.; Kern, K. *Surf. Sci.* **2001**, *475*, L229.
- (94) Arenz, M.; Stamenkovic, V.; Ross, P. N.; Markovic, N. M. *Electrochem. Commun.* **2003**, *5*, 809.
- (95) Greeley, J.; Norskov, J. K.; Kibler, L. A.; El-Aziz, A. M.; Kolb, D. M. *ChemPhysChem* **2006**, *7*, 1032.
- (96) Lucas, C. A.; Markovic, N. M.; Ball, M.; Stamenkovic, V.; Climent, V.; Ross, P. N. *Surf. Sci.* **2001**, *479*, 241.
- (97) Tanaka, K.; Sasahara, A. *J. Mol. Catal. A: Chem.* **2000**, *155*, 13.
- (98) Lamouri, A.; Gofer, Y.; Luo, Y.; Chottiner, G. S.; Scherson, D. A. *J. Phys. Chem. B* **2001**, *105*, 6172.
- (99) Yee, N.; Chottiner, G. S.; Scherson, D. A. *J. Phys. Chem. B* **2005**, *109*, 5707.
- (100) Batzill, M.; Koel, B. E. *Surf. Sci.* **2004**, *553*, 50.
- (101) Smadic, S.; Osgood, R. M. *Phys. Rev. B: Condens. Matter* **2005**, *71*, 165424.
- (102) Miya, K.; Sinsarp, A.; Sasaki, M.; Yamamoto, S. *Jpn. J. Appl. Phys., Part 2* **2005**, *44*, L31.
- (103) Schuster, R.; Roder, H.; Bromann, K.; Brune, H.; Kern, K. *Phys. Rev. B: Condens. Matter* **1996**, *54*, 13476.
- (104) Tsay, J. S.; Shern, C. S. *J. Vac. Sci. Technol., A* **1996**, *14*, 2522.
- (105) Tsay, J. S.; Shern, C. S. *Chin. J. Phys.* **1996**, *34*, 130.
- (106) Tsay, J. S.; Yao, Y. D.; Shern, C. S. *Phys. Rev. B: Condens. Matter* **1998**, *58*, 3609.
- (107) Batzill, M.; Beck, D.; Koel, B. E. *Surf. Sci.* **2004**, *558*, 35.
- (108) Panja, C.; Saliba, N.; Koel, B. E. *J. Phys. Chem. B* **2001**, *105*, 3786.
- (109) Li, Y. D.; Koel, B. E. *Surf. Sci.* **1995**, *330*, 193.
- (110) Zhao, H.; Koel, B. E. *Langmuir* **2005**, *21*, 971.
- (111) Voss, M. R.; Zhao, H.; Koel, B. E. *Surf. Sci.* **2004**, *560*, 235.
- (112) Batzill, M.; Beck, D. E.; Jerdev, D.; Koel, B. E. *J. Vac. Sci. Technol., A* **2001**, *19*, 1953.
- (113) Hayden, B. E.; Rendall, M. E.; South, O. *J. Mol. Catal. A: Chem.* **2005**, *228*, 55.
- (114) Janin, E.; Bjorkqvist, M.; Grehk, T. M.; Gothelid, M.; Pradier, C. M.; Karlsson, U. O.; Rosengren, A. *Appl. Surf. Sci.* **1996**, *99*, 371.
- (115) Olivas, A.; Jerdev, D. I.; Koel, B. E. *J. Catal.* **2004**, *222*, 285.
- (116) Rodriguez, J. A.; Hrbek, J.; Kuhn, M.; Jirsak, T.; Chaturvedi, S.; Maiti, A. *J. Chem. Phys.* **2000**, *113*, 11284.
- (117) Fearon, J.; Watson, G. W. *J. Mater. Chem.* **2006**, *16*, 1989.
- (118) Kildemo, M.; Juel, M.; Raaen, S. *Surf. Sci.* **2005**, *581*, 133.
- (119) Oliver, C. P.; King, B. V.; O'Connor, D. J. *Surf. Sci.* **2004**, *557*, 101.

- (120) Ramstad, A.; Strisland, F.; Ramsvik, T.; Borg, A. *Surf. Sci.* **2000**, 458, 135.
- (121) Duisberg, M.; Drager, M.; Wandelt, K.; Gruber, E. L. D.; Schmid, M.; Varga, P. *Surf. Sci.* **1999**, 435, 554.
- (122) Moest, B.; Wouda, P. T.; van der Gon, A. W. D.; Langelaar, M. C.; Brongersma, H. H.; Nieuwenhuys, B. E.; Boerma, D. O. *Surf. Sci.* **2001**, 473, 159.
- (123) Schlappa, A.; Kasberger, U.; Menzel, D.; Jakob, P. *Surf. Sci.* **2002**, 502–503, 129.
- (124) de Mongeot, F. B.; Scherer, M.; Gleich, B.; Kopatzki, E.; Behm, R. J. *Surf. Sci.* **1998**, 411, 249.
- (125) Diemant, T.; Hager, T.; Hoster, H. E.; Rauscher, H.; Behm, R. J. *Surf. Sci.* **2003**, 541, 137.
- (126) Kolaczkiwicz, J.; Bauer, E. *Surf. Sci.* **1996**, 366, 71.
- (127) Zellner, M. B.; Goda, A. M.; Skoplyak, O.; Barteau, M. A.; Chen, J. G. *Surf. Sci.* **2005**, 583, 281.
- (128) Tao, H.-S.; Rowe, J. E.; Madey, T. E. *Surf. Sci.* **1998**, 407, L640.
- (129) Tao, H.-S.; Nien, C.-H.; Madey, T. E.; Rowe, J. E.; Wertheim, G. K. *Surf. Sci.* **1996**, 357–358, 55.
- (130) Pelhos, K.; Madey, T. E.; Hannon, J. B.; Kellogg, G. L. *Surf. Rev. Lett.* **1999**, 6, 767.
- (131) Antczak, G.; Madey, T. E.; Blaszczyzyn, M.; Blaszczyzyn, R. *Vacuum* **2001**, 63, 43.
- (132) Kolodziej, J. J.; Madey, T. E.; Keister, J. W.; Rowe, J. E. *Phys. Rev. B: Condens. Matter* **2000**, 62, 5150.
- (133) Kolodziej, J. J.; Pelhos, K.; Abdelrehim, I. M.; Keister, J. W.; Rowe, J. E.; Madey, T. E. *Prog. Surf. Sci.* **1998**, 59, 117.
- (134) Pelhos, K.; Abdelrehim, I. M.; Nien, C.-H.; Madey, T. E. *J. Phys. Chem. B* **2001**, 105, 3708.
- (135) Block, J.; Kolodziej, J. J.; Rowe, J. E.; Madey, T. E.; Schroder, E. *Thin Solid Films* **2003**, 428, 47.
- (136) Yang, X.; Koel, B. E.; Wang, H.; Chen, W.; Bartynski, R. A. *ACS Nano* **2012**, 6, 1404.
- (137) Richardson, J. T. *Principles of catalyst development*; Plenum Press: New York, 1989.
- (138) Albertazzi, S.; Busca, G.; Finocchio, E.; Glockler, R.; Vaccari, A. *J. Catal.* **2004**, 223, 372.
- (139) Jongpatiwat, S.; Li, Z. R.; Resasco, D. E.; Alvarez, W. E.; Sughrae, E. L.; Dodwell, G. W. *Appl. Catal., A* **2004**, 262, 241.
- (140) Plomp, A. J.; van Asten, D. M. P.; van der Eerden, A. M. J.; Maki-Arvela, P.; Murzin, D. Y.; de Jong, K. P.; Bitter, J. H. *J. Catal.* **2009**, 263, 146.
- (141) Silvestre-Albero, J.; Serrano-Ruiz, J. C.; Sepulveda-Escribano, A.; Rodriguez-Reinoso, F. *Appl. Catal., A* **2005**, 292, 244.
- (142) Merlo, A. B.; Vetere, V.; Ruggera, J. F.; Casella, M. L. *Catal. Commun.* **2009**, 10, 1665.
- (143) Lonergan, W. W.; Vlachos, D. G.; Chen, J. G. *J. Catal.* **2010**, 271, 239.
- (144) Serna, P.; Concepción, P.; Corma, A. *J. Catal.* **2009**, 265, 19.
- (145) Chandler, B. D.; Pignolet, L. H. *Catal. Today* **2001**, 65, 39.
- (146) Todorova, S.; Kadinov, G.; Tenchev, K.; Kalvachev, Y.; Kostov-Kytin, V. *J. Mater. Sci.* **2007**, 42, 3315.
- (147) Chandler, B. D.; Schabel, A. B.; Pignolet, L. H. *J. Catal.* **2000**, 193, 186.
- (148) Graf, I. V. G.; Bacon, J. W.; Consugar, M. B.; Curley, M. E.; Ito, L. N.; Pignolet, L. H. *Inorg. Chem.* **1996**, 35, 689.
- (149) Koh, A. C. W.; Chen, L. W.; Leong, W. K.; Ang, T. P.; Johnson, B. F. G.; Khimyak, T.; Lin, J. Y. *Int. J. Hydrogen Energy* **2009**, 34, 5691.
- (150) Margitfalvi, J. L.; Borbath, I.; Hegedus, M.; Tompos, A. *Appl. Catal., A* **2002**, 229, 35.
- (151) Ekou, T.; Vicente, A.; Lafaye, G.; Espécel, C.; Marecot, P. *Appl. Catal., A* **2006**, 314, 64.
- (152) Ekou, T.; Vicente, A.; Lafaye, G.; Espécel, C.; Marecot, P. *Appl. Catal., A* **2006**, 314, 73.
- (153) Schaal, M. T.; Pickerel, A. C.; Williams, C. T.; Monnier, J. R. *J. Catal.* **2008**, 254, 131.
- (154) Veisz, B.; Tóth, L.; Teschner, D.; Paál, Z.; Györfy, N.; Wild, U.; Schlögl, R. *J. Mol. Catal. A: Chem.* **2005**, 238, 56.
- (155) Alayoglu, S.; Beaumont, S.; Zheng, F.; Pushkarev, V.; Zheng, H.; Iablokov, V.; Liu, Z.; Guo, J.; Kruse, N.; Somorjai, G. *Top. Catal.* **2011**, 54, 778.
- (156) Nilekar, A. U.; Alayoglu, S.; Eichhorn, B.; Mavrikakis, M. *J. Am. Chem. Soc.* **2010**, 132, 7418.
- (157) Mayrhofer, K. J. J.; Juhart, V.; Hartl, K.; Hanzlik, M.; Arenz, M. *Angew. Chem., Int. Ed.* **2009**, 48, 3529.
- (158) Yang, X. J.; Cheng, F. Y.; Liang, J.; Tao, Z. L.; Chen, J. *Int. J. Hydrogen Energy* **2011**, 36, 1984.
- (159) Zhang, X. B.; Yan, J. M.; Han, S.; Shioyama, H.; Xu, Q. *J. Am. Chem. Soc.* **2009**, 131, 2778.
- (160) Cheney, B. A. Masters thesis, University of Delaware, 2010.
- (161) Zhang, X.; Tsang, K.-Y.; Chan, K.-Y. *J. Electroanal. Chem.* **2004**, 573, 1.
- (162) Cheney, B. A.; Lauterbach, J. A.; Chen, J. G. *Appl. Catal., A* **2011**, 394, 41.
- (163) Lang, H. F.; May, R. A.; Iversen, B. L.; Chandler, B. D. *J. Am. Chem. Soc.* **2003**, 125, 14832.
- (164) Scott, R. W. J.; Wilson, O. M.; Crooks, R. M. *J. Phys. Chem. B* **2004**, 109, 692.
- (165) Albiter, M. A.; Morales, R.; Zaera, F. *Appl. Catal., A* **2011**, 391, 386.
- (166) Guo, Z.; Chen, Y. T.; Li, L. S.; Wang, X. M.; Haller, G. L.; Yang, Y. H. *J. Catal.* **2010**, 276, 314.
- (167) Li, H.; Yu, X.; Tu, S.-T.; Yan, J.; Wang, Z. *Appl. Catal., A* **2010**, 387, 215.
- (168) Roussel, J. L.; Stievano, L.; Aires, F.; Geantet, C.; Renouprez, A. J.; Pellarin, M. *J. Catal.* **2001**, 197, 335.
- (169) L'Vov, B. V. *J. Anal. Chem.* **2005**, 60, 382.
- (170) *ICP Emission Spectrometry: A Practical Guide*; Nolte, J., Ed.; Wiley-VCH: Morlenbach, 2003.
- (171) Pawelec, B.; Damyanova, S.; Arishtirova, K.; Fierro, J. L. G.; Petrov, L. *Appl. Catal., A* **2007**, 323, 188.
- (172) Özkara-Aydınoğlu, Ş.; Aksoylu, A. E. *Int. J. Hydrogen Energy* **2011**, 36, 2950.
- (173) Ozkaya, D.; Zhou, W. Z.; Thomas, J. M.; Midgley, P.; Keast, V. J.; Hermans, S. *Catal. Lett.* **1999**, 60, 113.
- (174) Gan, L.; Yu, R.; Luo, J.; Cheng, Z. Y.; Zhu, J. *J. Phys. Chem. Lett.* **2012**, 3, 934.
- (175) Ciston, J.; Si, R.; Rodriguez, J. A.; Hanson, J. C.; Martinez-Arias, A.; Fernandez-Garcia, M.; Zhu, Y. M. *J. Phys. Chem. C* **2011**, 115, 13851.
- (176) Williams, D. B.; Carter, C. B. *Transmission electron microscopy*; Springer: New York, 1996.
- (177) Griffiths, P. R.; De Haseth, J. A. *Fourier transform infrared spectrometry*; Wiley: New York, 1986.
- (178) Smith, B. C. *Fundamentals of Fourier transform infrared spectrometry*; CRC Press: Boca Raton, FL, 1996.
- (179) Ferri, D.; Burgi, T.; Baiker, A. *J. Phys. Chem. B* **2001**, 105, 3187.
- (180) Burcham, L.; Deo, G.; Gao, X.; Wachs, I. *Top. Catal.* **2000**, 11–12, 85.
- (181) Koningsberger, D. C.; Prins, R. *X-ray absorption: principles, applications, techniques of EXAFS, SEXAFS, and XANES*; Wiley: New York, 1988.
- (182) Niemantsverdriet, J. W. *Spectroscopy in catalysis: An introduction*; VCH Weinheim: New York, 1995.
- (183) Aksenov, V. L.; Kuzmin, A. Y.; Purans, J.; Tyutyunnikov, S. I. *Phys. Part. Nucl.* **2001**, 32, 675.
- (184) Aksenov, V. L.; Koval'chuk, M. V.; Kuz'min, A. Y.; Purans, Y.; Tyutyunnikov, S. I. *Crystallogr. Rep.* **2006**, 51, 908.
- (185) Iwasawa, Y. *X-ray absorption fine structure for catalysis and surfaces*; World Scientific: Hackensack, NJ, 1986.
- (186) Teo, B. K. *EXAFS: Basic principles and data analysis*; Springer-Verlag: Berlin/New York, 1986.
- (187) Newville, M. *J. Synchrotron Radiat.* **2001**, 8, 322.
- (188) Ravel, B.; Newville, M. *J. Synchrotron Radiat.* **2005**, 12, 537.
- (189) Rehr, J. J.; Albers, R. C. *Rev. Mod. Phys.* **2000**, 72, 621.
- (190) Grunwaldt, J. D.; Clausen, B. S. *Top. Catal.* **2002**, 18, 37.
- (191) Weckhuysen, B. M. *Phys. Chem. Chem. Phys.* **2003**, 5, 4351.

- (192) Beale, A. M.; van der Eerden, A. M. J.; Jacques, S. D. M.; Leynaud, O.; O'Brien, M. G.; Meneau, F.; Nikitenko, S.; Bras, W.; Weckhuysen, B. M. *J. Am. Chem. Soc.* **2006**, *128*, 12386.
- (193) Nikitenko, S.; Beale, A. M.; van der Eerden, A. M. J.; Jacques, S. D. M.; Leynaud, O.; O'Brien, M. G.; Detollenaere, D.; Kaptein, R.; Weckhuysen, B. M.; Bras, W. *J. Synchrotron Radiat.* **2008**, *15*, 632.
- (194) Bentrup, U. *Chem. Soc. Rev.* **2010**, *39*, 4718.
- (195) Toda, T.; Igarashi, H.; Watanabe, M. *J. Electroanal. Chem.* **1999**, *460*, 258.
- (196) Wan, L. J.; Moriyama, T.; Ito, M.; Uchida, H.; Watanabe, M. *Chem. Commun.* **2002**, 58.
- (197) Watanabe, M. *Electrochemistry* **2000**, *68*, 941.
- (198) Ruban, A. V.; Skriver, H. L.; Norskov, J. K. *Phys. Rev. B: Condens. Matter* **1999**, *59*, 15990.
- (199) Alden, M.; Abrikosov, I. A.; Johansson, B.; Rosengaard, N. M.; Skriver, H. L. *Phys. Rev. B: Condens. Matter* **1994**, *50*, 5131.
- (200) Menning, C. A.; Chen, J. G. *J. Chem. Phys.* **2009**, *130*.
- (201) Callejas-Tovar, R.; Balbuena, P. B. *Surf. Sci.* **2008**, *602*, 3531.
- (202) Menning, C. A.; Chen, J. G. *Top. Catal.* **2010**, *53*, 338.
- (203) Wang, H.; Stamatakis, M.; Hansgen, D. A.; Caratzoulas, S.; Vlachos, D. G. *J. Chem. Phys.* **2010**, *133*.
- (204) Mun, B. S.; Rossi, M.; Ross, P. N. *J. Chem. Phys.* **2008**, *129*.
- (205) Duan, Z. Y.; Zhong, J.; Wang, G. F. *J. Chem. Phys.* **2010**, *133*.
- (206) Ma, Y. G.; Balbuena, P. B. *J. Electrochem. Soc.* **2010**, *157*, B959.
- (207) Ma, T.; Fu, Q.; Cui, Y.; Zhang, Z.; Wang, Z.; Tan, D.; Bao, X. *Chin. J. Catal.* **2010**, *31*, 24.
- (208) Ma, T.; Fu, Q.; Su, H.-Y.; Liu, H.-Y.; Cui, Y.; Wang, Z.; Mu, R.-T.; Li, W.-X.; Bao, X.-H. *ChemPhysChem* **2009**, *10*, 1013.
- (209) Mu, R.; Fu, Q.; Liu, H.; Tan, D.; Zhai, R.; Bao, X. *Appl. Surf. Sci.* **2009**, *255*, 7296.
- (210) Andersson, K. J.; Calle-Vallejo, F.; Rossmeisl, J.; Chorkendorff, L. *J. Am. Chem. Soc.* **2009**, *131*, 2404.
- (211) Ma, Y. G.; Balbuena, P. B. *Surf. Sci.* **2009**, *603*, 349.
- (212) Ma, Y. G.; Balbuena, P. B. *J. Phys. Chem. C* **2008**, *112*, 14520.
- (213) Ma, Y. G.; Balbuena, P. B. *Surf. Sci.* **2008**, *602*, 107.
- (214) Ma, Y.; Balbuena, P. B. *J. Chem. Theory Comput.* **2008**, *4*, 1991.
- (215) Escano, M. C. S.; Nguyen, T. Q.; Nakanishi, H.; Kasai, H. *Surf. Sci.* **2008**, *602*, 3415.
- (216) Ramirez-Caballero, G. E.; Balbuena, P. B. *Chem. Phys. Lett.* **2011**, *507*, 117.
- (217) Duan, Z. Y.; Wang, G. F. *J. Phys.: Condens. Matter* **2011**, *23*.
- (218) Mu, R. T.; Guo, X. G.; Fu, Q.; Bao, X. H. *J. Phys. Chem. C* **2011**, *115*, 20590.
- (219) Zhang, Y. H.; Duan, Z. Y.; Xiao, C.; Wang, G. F. *Surf. Sci.* **2011**, *605*, 1577.
- (220) Su, H. Y.; Gu, X. K.; Ma, X. F.; Zhao, Y. H.; Bao, X. H.; Li, W. X. *Catal. Today* **2011**, *165*, 89.
- (221) Huang, Y. W.; Chou, T. Y.; Yu, G. Y.; Lee, S. L. *J. Phys. Chem. C* **2011**, *115*, 9105.
- (222) Bergbreiter, A.; Hoster, H. E.; Behm, R. J. *ChemPhysChem* **2011**, *12*, 1148.
- (223) Diemant, T.; Bergbreiter, A.; Bansmann, J.; Hoster, H. E.; Behm, R. J. *ChemPhysChem* **2010**, *11*, 3123.
- (224) Wei, G. F.; Liu, Z. P. *Energy Environ. Sci.* **2011**, *4*, 1268.
- (225) Tenney, S. A.; Ratliff, J. S.; Roberts, C. C.; He, W.; Ammal, S. C.; Heyden, A.; Chen, D. A. *J. Phys. Chem. C* **2010**, *114*, 21652.
- (226) Menning, C. A.; Chen, J. G. *J. Power Sources* **2010**, *195*, 3140.
- (227) Hirschl, R.; Delbecq, F.; Sautet, P.; Hafner, J. J. *Catal.* **2003**, *217*, 354.
- (228) Murillo, L. E.; Khan, N. A.; Chen, J. G. *Surf. Sci.* **2005**, *594*, 27.
- (229) Beccat, P.; Bertolini, J. C.; Gauthier, Y.; Massardier, J.; Ruiz, P. *J. Catal.* **1990**, *126*, 451.
- (230) Jerdev, D. I.; Olivas, A.; Koel, B. E. *J. Catal.* **2002**, *205*, 278.
- (231) Humbert, M. P.; Murillo, L. E.; Chen, J. G. *ChemPhysChem* **2008**, *9*, 1262.
- (232) Khan, N. A.; Chen, J. G. *J. Vac. Sci. Technol., A* **2003**, *21*, 1302.
- (233) Hirschl, R.; Eichler, A.; Hafner, J. J. *Catal.* **2004**, *226*, 273.
- (234) Zhao, H. B.; Koel, B. E. *Catal. Lett.* **2005**, *99*, 27.
- (235) Peck, J. W.; Mahon, D. I.; Koel, B. E. *Surf. Sci.* **1998**, *410*, 200.
- (236) Zhao, H. B.; Koel, B. E. *J. Catal.* **2005**, *234*, 24.
- (237) Vigne, F.; Haubrich, J.; Loffreda, D.; Sautet, P.; Delbecq, F. *J. Catal.* **2010**, *275*, 129.
- (238) Lonergan, W. W.; Xing, X.; Zheng, R.; Qi, S.; Huang, B.; Chen, J. G. *Catal. Today* **2011**, *160*, 61.
- (239) Humbert, M. P.; Stottlemeyer, A. L.; Menning, C. A.; Chen, J. G. *J. Catal.* **2011**, *280*, 96.
- (240) Murillo, L. E.; Chen, J. G. *Surf. Sci.* **2008**, *602*, 919.
- (241) Murillo, L. E.; Menning, C. A.; Chen, J. G. *J. Catal.* **2009**, *268*, 335.
- (242) Medlin, J. W. *ACS Catal.* **2011**, *1*, 1284.
- (243) Qi, S.; Yu, W.; Lonergan, W. W.; Yang, B.; Chen, J. G. *ChemCatChem* **2010**, *2*, 625.
- (244) Qi, S.; Yu, W.; Lonergan, W. W.; Yang, B.; Chen, J. G. *Chin. J. Catal.* **2010**, *31*, 955.
- (245) Zheng, R.; Humbert, M. P.; Zhu, Y.; Chen, J. G. *Catal. Sci. Technol.* **2011**, *1*, 638.
- (246) Zheng, R.; Zhu, Y.; Chen, J. G. *ChemCatChem* **2011**, *3*, 578.
- (247) Qi, S.; Cheney, B. A.; Zheng, R.; Lonergan, W. W.; Yu, W.; Chen, J. G. *Appl. Catal., A* **2011**, *393*, 44.
- (248) Tsai, Y. L.; Xu, C.; Koel, B. E. *Surf. Sci.* **1997**, *385*, 37.
- (249) Zhao, H. B.; Koel, B. E. *J. Phys. Chem. C* **2009**, *113*, 18152.
- (250) Becker, C.; Delbecq, F.; Breitbach, J.; Hamm, G.; Franke, D.; Jager, F.; Wandelt, K. *J. Phys. Chem. B* **2004**, *108*, 18960.
- (251) Ma, H. Y.; Wang, G. C. *J. Catal.* **2011**, *281*, 63.
- (252) Saliccioli, M.; Stamatakis, M.; Caratzoulas, S.; Vlachos, D. G. *Chem. Eng. Sci.* **2011**, *66*, 4319.
- (253) Hansgen, D. A.; Thomanek, L. M.; Chen, J. G.; Vlachos, D. G. *J. Chem. Phys.* **2011**, *134*.
- (254) Ren, H.; Humbert, M. P.; Menning, C. A.; Chen, J. G.; Shu, Y.; Singh, U. G.; Cheng, W.-C. *Appl. Catal., A* **2010**, *375*, 303.
- (255) Panja, C.; Saliba, N.; Koel, B. E. *Surf. Sci.* **1998**, *395*, 248.
- (256) Skoplyak, O.; Menning, C. A.; Barteau, M. A.; Chen, J. G. *Top. Catal.* **2008**, *51*, 49.
- (257) Skoplyak, O.; Barteau, M. A.; Chen, J. G. *Surf. Sci.* **2008**, *602*, 3578.
- (258) Skoplyak, O.; Barteau, M. A.; Chen, J. G. *J. Phys. Chem. B* **2006**, *110*, 1686.
- (259) Skoplyak, O.; Barteau, M. A.; Chen, J. G. *ChemSusChem* **2008**, *1*, 524.
- (260) Skoplyak, O.; Barteau, M. A.; Chen, J. G. *Catal. Today* **2009**, *147*, 150.
- (261) Ren, H.; Hansgen, D. A.; Stottlemeyer, A. L.; Kelly, T. G.; Chen, J. G. *ACS Catal.* **2011**, *1*, 390.
- (262) Stottlemeyer, A. L.; Ren, H.; Chen, J. G. *Surf. Sci.* **2009**, *603*, 2630.
- (263) Veltruska, K.; Cabala, M.; Libra, J.; Skala, T.; Tsud, N.; Matolin, V. *Surf. Interface Anal.* **2010**, *42*, 555.
- (264) Skoplyak, O.; Menning, C. A.; Barteau, M. A.; Chen, J. G. *J. Chem. Phys.* **2007**, *114707*.
- (265) Neurock, M.; Wasileski, S. A.; Mei, D. *Chem. Eng. Sci.* **2004**, *59*, 4703.
- (266) Meng, J. H.; Carl, A. M.; Zellner, M. B.; Chen, J. G. *Surf. Sci.* **2010**, *604*, 1845.
- (267) Kieken, L. D.; Neurock, M.; Mei, D. *J. Phys. Chem. B* **2004**, *109*, 2234.
- (268) Kim, J.; Welch, L. A.; Olivas, A.; Podkolzin, S. G.; Koel, B. E. *Langmuir* **2010**, *26*, 16401.
- (269) Kim, J.; Fu, J.; Podkolzin, S. G.; Koel, B. E. *J. Phys. Chem. C* **2010**, *114*, 17238.
- (270) Desai, S.; Neurock, M. *Electrochim. Acta* **2003**, *48*, 3759.
- (271) Su, H. Y.; Bao, X. H.; Li, W. X. *J. Chem. Phys.* **2008**, *128*.
- (272) Fu, Q.; Li, W. X.; Yao, Y. X.; Liu, H. Y.; Su, H. Y.; Ma, D.; Gu, X. K.; Chen, L. M.; Wang, Z.; Zhang, H.; Wang, B.; Bao, X. H. *Science* **2010**, *328*, 1141.
- (273) Mu, R.; Fu, Q.; Xu, H.; Zhang, H.; Huang, Y.; Jiang, Z.; Zhang, S.; Tan, D.; Bao, X. *J. Am. Chem. Soc.* **2011**, *133*, 1978.
- (274) Gazdzicki, P.; Thussing, S.; Jakob, P. *J. Phys. Chem. C* **2011**, *115*, 23013.

- (275) Kuhn, M.; Rodriguez, J. A. *Catal. Lett.* **1995**, *32*, 345.
- (276) Lonergan, W. W.; Wang, T. F.; Vlachos, D. G.; Chen, J. G. *Appl. Catal., A* **2011**, *408*, 87.
- (277) Lu, S.; Lonergan, W. W.; Zhu, Y.; Xie, Y.; Chen, J. G. *Appl. Catal., B* **2009**, *91*, 610.
- (278) Rynkowski, J.; Rajski, D.; Szyska, I.; Grzechowiak, J. R. *Catal. Today* **2004**, *90*, 159.
- (279) Khan, N. A.; Murillo, L. E.; Shu, Y. Y.; Chen, J. G. *Catal. Lett.* **2005**, *105*, 233.
- (280) Lu, S. L.; Lonergan, W. W.; Bosco, J. P.; Wang, S. R.; Zhu, Y. X.; Xie, Y. C.; Chen, J. G. *J. Catal.* **2008**, *259*, 260.
- (281) Sun, K.-Q.; Hong, Y.-C.; Zhang, G.-R.; Xu, B.-Q. *ACS Catal.* **2011**, *1*, 1336.
- (282) Siepen, K.; Bonnemann, H.; Brijoux, W.; Rothe, J.; Hormes, J. *Appl. Organomet. Chem.* **2000**, *14*, 549.
- (283) Silvestre-Albero, J.; Sepulveda-Escribano, A.; Rodriguez-Reinoso, F.; Anderson, J. A. *J. Catal.* **2004**, *223*, 179.
- (284) Homs, N.; Llorca, J.; de la Piscina, P. R.; Rodriguez-Reinoso, F.; Sepulveda-Escribano, A.; Silvestre-Albero, J. *Phys. Chem. Chem. Phys.* **2001**, *3*, 1782.
- (285) Serrano-Ruiz, J. C.; Sepulveda-Escribano, A.; Rodriguez-Reinoso, F.; Duprez, D. *J. Mol. Catal. A: Chem.* **2007**, *268*, 227.
- (286) Siani, A.; Alexeev, O. S.; Lafaye, G.; Amiridis, M. D. *J. Catal.* **2009**, *266*, 26.
- (287) Rachmady, W.; Vannice, M. A. *J. Catal.* **2002**, *209*, 87.
- (288) Crabb, E. M.; Marshall, R. *Appl. Catal., A* **2001**, *217*, 41.
- (289) Gyorffy, N.; Paal, Z. *J. Mol. Catal. A: Chem.* **2008**, *295*, 24.
- (290) Burch, R.; Paun, C.; Cao, X. M.; Crawford, P.; Goodrich, P.; Hardacre, C.; Hu, P.; McLaughlin, L.; Sa, J.; Thompson, J. M. *J. Catal.* **2011**, *283*, 89.
- (291) Zheng, Y.; Wang, X. X.; Fu, X. Z.; Wei, K. M. *Appl. Organomet. Chem.* **2007**, *21*, 836.
- (292) Li, J.; Tian, W. P.; Shi, L. *Catal. Lett.* **2011**, *141*, 565.
- (293) Li, J.; Tian, W. P.; Wang, X.; Shi, L. *Chem. Eng. J.* **2011**, *175*, 417.
- (294) Gucci, L.; Bazin, D. *Appl. Catal., A* **1999**, *188*, 163.
- (295) Gucci, L.; Bazin, D.; Kovacs, I.; Borko, L.; Schay, Z.; Lynch, J.; Parent, P.; Lafon, C.; Stefler, G.; Koppány, Z.; Sajo, I. *Top. Catal.* **2002**, *20*, 129.
- (296) Choi, S. H.; Lee, J. S. *J. Catal.* **1997**, *167*, 364.
- (297) Ismagilov, Z. R.; Matus, E. V.; Yakutova, A. M.; Protasova, L. N.; Ismagilov, I. Z.; Kerzhentsev, M. A.; Rebrov, E. V.; Schouten, J. C. *Catal. Today* **2009**, *147*, S81.
- (298) Tsang, S. C.; Cailuo, N.; Oduro, W.; Kong, A. T. S.; Clifton, L.; Yu, K. M. K.; Thiebaud, B.; Cookson, J.; Bishop, P. *ACS Nano* **2008**, *2*, 2547.
- (299) Santori, G. F.; Casella, M. L.; Siri, G. J.; Aduriz, H. R.; Ferretti, O. A. *React. Kinet. Catal. Lett.* **2002**, *75*, 225.
- (300) Castillejos, E.; Jahjah, M.; Favier, L.; Orejón, A.; Pradel, C.; Teuma, E.; Masdeu-Bultó, A. M.; Serp, P.; Gómez, M. *ChemCatChem* **2012**, *4*, 118.
- (301) Zheng, R.; Porosoff, M. D.; Weiner, J. L.; Lu, S.; Zhu, Y.; Chen, J. G. *Appl. Catal., A* **2012**, *419–420*, 126.
- (302) Hammer, B.; Nørskov, J. K. *Adv. Catal.* **2000**, *45*, 71.
- (303) Shu, Y. Y.; Murillo, L. E.; Bosco, J. P.; Huang, W.; Frenkel, A. I.; Chen, J. G. *Appl. Catal., A* **2008**, *339*, 169.
- (304) Sedlacek, J.; Hilaire, L.; Legare, P.; Maire, G. *Surf. Sci.* **1982**, *115*, 541.
- (305) Arenas-Alatorre, J.; Avalos-Borja, M.; Diaz, G. *Appl. Surf. Sci.* **2002**, *189*, 7.
- (306) Goda, A. M.; Neurock, M.; Barteau, M. A.; Chen, J. G. *Surf. Sci.* **2008**, *602*, 2513.
- (307) Oxford, S. M.; Lee, P. L.; Chupas, P. J.; Chapman, K. W.; Kung, M. C.; Kung, H. H. *J. Phys. Chem. C* **2010**, *114*, 17085.
- (308) Borodzinski, A. *Catal. Rev.—Sci. Eng.* **2006**, *48*, 91.
- (309) Stanislaus, A.; Cooper, B. H. *Catal. Rev.—Sci. Eng.* **1994**, *36*, 75.
- (310) Lu, S. L.; Menning, C. A.; Zhu, Y. X.; Chen, J. G. *ChemPhysChem* **2009**, *10*, 1763.
- (311) Kumbiliev, K.; Gaidai, N. A.; Nekrasov, N. V.; Petrov, L.; Lapidus, A. L. *Chem. Eng. J.* **2006**, *120*, 25.
- (312) Coq, B.; Figueras, F. *J. Mol. Catal. A: Chem.* **2001**, *173*, 117.
- (313) Babu, P. K.; Kim, H. S.; Chung, J. H.; Oldfield, E.; Wieckowski, A. *J. Phys. Chem. B* **2004**, *108*, 20228.
- (314) Do, P. T. M.; Foster, A. J.; Chen, J. G.; Lobo, R. F. *Green Chem.* **2012**, *14*, 1388.
- (315) Maki-Arvela, P.; Hajek, J.; Salmi, T.; Murzin, D. Y. *Appl. Catal., A* **2005**, *292*, 1.
- (316) Nishimura, S. *Handbook of Heterogeneous Catalytic Hydrogenation for Organic Synthesis*; Wiley: New York, 2001.
- (317) Loffreda, D.; Delbecq, F.; Vigne, F.; Sautet, P. *J. Am. Chem. Soc.* **2006**, *128*, 1316.
- (318) Ji, N.; Zhang, T.; Zheng, M. Y.; Wang, A. Q.; Wang, H.; Wang, X. D.; Chen, J. G. *Angew. Chem., Int. Ed.* **2008**, *47*, 8510.
- (319) Lim, K. H.; Mohammad, A. B.; Yudanov, I. V.; Neyman, K. M.; Bron, M.; Claus, P.; Rosch, N. *J. Phys. Chem. C* **2009**, *113*, 13231.
- (320) Bus, E.; van Bokhoven, J. A. *J. Phys. Chem. C* **2007**, *111*, 9761.
- (321) Mott, D.; Luo, J.; Njoki, P. N.; Lin, Y.; Wang, L. Y.; Zhong, C. *J. Catal. Today* **2007**, *122*, 378.
- (322) Alexeev, O. S.; Gates, B. C. *Ind. Eng. Chem. Res.* **2003**, *42*, 1571.
- (323) Chantavitoon, P.; Chavadej, S.; Schwank, J. *Chem. Eng. J.* **2004**, *98*, 99.
- (324) Mueller, S. G.; Stallbaumer, P. J.; Slade, D. A.; Stagg-Williams, S. M. *Catal. Lett.* **2005**, *103*, 69.
- (325) Tang, X. L.; Zhang, B. C.; Li, Y.; Xu, Y.; Xin, Q.; Shen, W. J. *J. Mol. Catal. A: Chem.* **2005**, *235*, 122.
- (326) Schaal, M. T.; Hyman, M. P.; Rangan, M.; Ma, S.; Williams, C. T.; Monnier, J. R.; Medlin, J. W. *Surf. Sci.* **2009**, *603*, 690.
- (327) Huang, Y. Y.; Sachtler, W. M. H. *J. Catal.* **1999**, *188*, 215.
- (328) Liu, M. H.; Yu, W. Y.; Liu, H. F.; Zheng, J. M. *J. Colloid Interface Sci.* **1999**, *214*, 231.
- (329) Liu, X. M.; Chen, J. R.; Zhao, S. L.; Li, X. J. *Chin. J. Catal.* **2005**, *26*, 323.
- (330) Epron, F.; Gauthard, F.; Pineda, C.; Barbier, J. *J. Catal.* **2001**, *198*, 309.
- (331) Marchesini, F. A.; Irusta, S.; Querini, C.; Miro, E. *Catal. Commun.* **2008**, *9*, 1021.
- (332) Kaneko, S.; Arakawa, T.; Ohshima, M.-a.; Kurokawa, H.; Miura, H. *Appl. Catal., A* **2009**, *356*, 80.
- (333) Pakhomov, N. A. *Kinet. Catal.* **2001**, *42*, 334.
- (334) Singh, S. K.; Xu, Q. A. *Inorg. Chem.* **2010**, *49*, 6148.
- (335) Siri, G. J.; Ramallo-Lopez, J. M.; Casella, M. L.; Fierro, J. L. G.; Requejo, F. G.; Ferretti, O. A. *Appl. Catal., A* **2005**, *278*, 239.
- (336) Biniwale, R. B.; Kariya, N.; Ichikawa, M. *Catal. Lett.* **2005**, *105*, 83.
- (337) Bednarova, L.; Lyman, C. E.; Rytter, E.; Holmen, A. *J. Catal.* **2002**, *211*, 335.
- (338) Salmones, J.; Wang, J. A.; Galicia, J. A.; Aguilar-Rios, G. *J. Mol. Catal. A: Chem.* **2002**, *184*, 203.
- (339) Liu, C. K.; Zhu, Q.; Wu, Z. H.; Zhou, Z. H.; Bhargava, G. R.; Parasher, S.; Rueter, M.; Zhou, B.; Chen, J. G. *Appl. Catal., A* **2010**, *390*, 19.
- (340) Kereszszegi, C.; Mallat, T.; Grunwaldt, J. D.; Baiker, A. *J. Catal.* **2004**, *225*, 138.
- (341) Dietrich, H.; Jacobi, K.; Ertl, G. *J. Chem. Phys.* **1996**, *105*, 8944.
- (342) Cheekatamarla, P. K.; Lane, A. M. *Int. J. Hydrogen Energy* **2005**, *30*, 1277.
- (343) Cheekatamarla, P. K.; Lane, A. M. *J. Power Sources* **2006**, *153*, 157.
- (344) Ronning, M.; Gjervan, T.; Prestvik, R.; Nicholson, D. G.; Holmen, A. *J. Catal.* **2001**, *204*, 292.
- (345) Simson, A.; Farrauto, R.; Castaldi, M. *Appl. Catal., B* **2011**, *106*, 295.
- (346) Kaila, R. K.; Gutierrez, A.; Slioor, R.; Kemell, M.; Leskela, M.; Krause, A. O. I. *Appl. Catal., B* **2008**, *84*, 223.
- (347) Yuan, L. X.; Chen, Y. Q.; Song, C. F.; Ye, T. Q.; Guo, Q. X.; Zhu, Q. S.; Torimoto, Y.; Li, Q. X. *Chem. Commun.* **2008**, 5215.

- (348) Kunkes, E. L.; Simonetti, D. A.; Dumesic, J. A.; Pyrz, W. D.; Murillo, L. E.; Chen, J. G.; Buttrey, D. J. *J. Catal.* **2008**, *260*, 164.
- (349) Huber, G. W.; Shabaker, J. W.; Evans, S. T.; Dumesic, J. A. *Appl. Catal., B* **2006**, *62*, 226.
- (350) Avci, A. K.; Trimm, D. L.; Aksoylu, A. E.; Onsan, Z. I. *Appl. Catal., A* **2004**, *258*, 235.
- (351) Tanksale, A.; Beltramini, J. N.; Dumesic, J. A.; Lu, G. Q. *J. Catal.* **2008**, *258*, 366.
- (352) Tanksale, A.; Zhou, C. H.; Beltramini, J. N.; Lu, G. Q. *J. Inclusion Phenom. Macrocyclic Chem.* **2009**, *65*, 83.
- (353) Croy, J. R.; Mostafa, S.; Hickman, L.; Heinrich, H.; Cuenya, B. R. *Appl. Catal., A* **2008**, *350*, 207.
- (354) Miyao, T.; Yamauchi, M.; Narita, H.; Naito, S. *Appl. Catal., A* **2006**, *299*, 285.
- (355) Kunkes, E. L.; Soares, R. R.; Simonetti, D. A.; Dumesic, J. A. *Appl. Catal., B* **2009**, *90*, 693.
- (356) Bianchi, C. L.; Canton, P.; Dimitratos, N.; Porta, F.; Prati, L. *Catal. Today* **2005**, *102*, 203.
- (357) Arishtirova, K.; Pawelec, B.; Nikolov, R. N.; Fierro, L. G.; Damyanova, S. *React. Kinet. Catal. Lett.* **2007**, *91*, 241.
- (358) Mukainakano, Y.; Yoshida, K.; Kado, S.; Okumura, K.; Kunimori, K.; Tomishige, K. *Chem. Eng. Sci.* **2008**, *63*, 4891.
- (359) Pinheiro, A. N.; Valentini, A.; Sasaki, J. M.; Oliveira, A. C. *Appl. Catal., A* **2009**, *355*, 156.
- (360) Garcia-Dieguez, M.; Finocchio, E.; Larrubia, M. A.; Alemany, L. J.; Busca, G. J. *Catal.* **2010**, *274*, 11.
- (361) Garcia-Dieguez, M.; Pieta, I. S.; Herrera, M. C.; Larrubia, M. A.; Alemany, L. J. *Appl. Catal., A* **2010**, *377*, 191.
- (362) Garcia-Dieguez, M.; Pieta, I. S.; Herrera, M. C.; Larrubia, M. A.; Alemany, L. J. *J. Catal.* **2010**, *270*, 136.
- (363) Tang, S.; Lin, J.; Tan, K. L. *Surf. Interface Anal.* **1999**, *28*, 155.
- (364) Kaila, R. K.; Gutierrez, A.; Krause, A. O. I. *Appl. Catal., B* **2008**, *84*, 324.
- (365) Gutierrez, A.; Karinen, R.; Airaksinen, S.; Kaila, R.; Krause, A. O. I. *Int. J. Hydrogen Energy* **2011**, *36*, 8967.
- (366) Orucu, E.; Gokaliler, F.; Aksoylu, A. E.; Onsan, Z. I. *Catal. Lett.* **2008**, *120*, 198.
- (367) Soyalt-Baltacıoğlu, F.; Aksoylu, A. E.; Onsan, Z. I. *Catal. Today* **2008**, *138*, 183.
- (368) Iriondo, A.; Cambra, J. F.; Barrio, V. L.; Guemez, M. B.; Arias, P. L.; Sanchez-Sanchez, M. C.; Navarro, R. M.; Fierro, J. L. G. *Appl. Catal., B* **2011**, *106*, 83.
- (369) Akhter, S.; White, J. M. *Surf. Sci.* **1986**, *167*, 101.
- (370) Diekhöner, L.; Butler, D. A.; Baurichter, A.; Luntz, A. C. *Surf. Sci.* **1998**, *409*, 384.
- (371) Gibson, K. D.; Dubois, L. H. *Surf. Sci.* **1990**, *233*, 59.
- (372) Anderson, J. A.; Fernandez-Garcia, M. *Chem. Eng. Res. Des.* **2000**, *78*, 935.
- (373) Ni, M.; Leung, D. Y. C.; Leung, M. K. H. *Int. J. Hydrogen Energy* **2007**, *32*, 3238.
- (374) Sheng, P. Y.; Chiu, W. W.; Yee, A.; Morrison, S. J.; Idriss, H. *Catal. Today* **2007**, *129*, 313.
- (375) Agrawal, R.; Singh, N. R.; Ribeiro, F. H.; Delgass, W. N. *Proc. Natl. Acad. Sci. U.S.A.* **2007**, *104*, 4828.
- (376) Ko, E. Y.; Park, E. D.; Seo, K. W.; Lee, H. C.; Lee, D.; Kim, S. *Catal. Lett.* **2006**, *110*, 275.
- (377) Ko, E. Y.; Park, E. D.; Seo, K. W.; Lee, H. C.; Lee, D.; Kim, S. *Korean J. Chem. Eng.* **2006**, *23*, 182.
- (378) Snytnikov, P. V.; Yusevko, K. V.; Korenev, S. V.; Shubin, Y. V.; Sobyenin, V. A. *Kinet. Catal.* **2007**, *48*, 276.
- (379) Ko, E. Y.; Park, E. D.; Lee, H. C.; Lee, D.; Kim, S. *Angew. Chem., Int. Ed.* **2007**, *46*, 734.
- (380) Komatsu, T.; Tamura, A. *J. Catal.* **2008**, *258*, 306.
- (381) Parinyaswan, A.; Pongstabodee, S.; Luengnarueamitchai, A. *Int. J. Hydrogen Energy* **2006**, *31*, 1942.
- (382) Aksoylu, A. E.; Freitas, M. M. A.; Figueiredo, J. L. *Catal. Today* **2000**, *62*, 337.
- (383) Caglayan, B. S.; Soykal, I. I.; Aksoylu, A. E. *Appl. Catal., B* **2011**, *106*, 540.
- (384) Ayastuy, J. L.; Gonzalez-Marcos, M. P.; Gonzalez-Velasco, J. R.; Gutierrez-Ortiz, M. A. *Appl. Catal., B* **2007**, *70*, 532.
- (385) Ebashi, T.; Ishida, Y.; Nakagawa, Y.; Ito, S.-i.; Kubota, T.; Tomishige, K. *J. Phys. Chem. C* **2010**, *114*, 6518.
- (386) Choung, S. Y.; Ferrandon, M.; Krause, T. *Catal. Today* **2005**, *99*, 257.
- (387) Sato, Y.; Terada, K.; Hasegawa, S.; Miyao, T.; Naito, S. *Appl. Catal., A* **2005**, *296*, 80.
- (388) Yu, Q.; Chen, W.; Li, Y.; Jin, M.; Suo, Z. *Catal. Today* **2010**, *158*, 324.
- (389) Kugai, J.; Miller, J. T.; Guo, N.; Song, C. J. *Catal.* **2011**, *277*, 46.
- (390) Borko, L.; Gucci, L. *Top. Catal.* **2006**, *39*, 34.
- (391) Li, B. T.; Kado, S.; Mukainakano, Y.; Miyazawa, T.; Miyao, T.; Naito, S.; Okumura, K.; Kunimori, K.; Tomishige, K. *J. Catal.* **2007**, *245*, 144.
- (392) Persson, K.; Ersson, A.; Colussi, S.; Trovarelli, A.; Jaras, S. G. *Appl. Catal., B* **2006**, *66*, 175.
- (393) Horiuchi, C. M.; Rangan, M.; Israel, B. M.; Medlin, J. W. *J. Phys. Chem. C* **2009**, *113*, 14900.
- (394) Lanza, R.; Canu, P.; Jaeras, S. G. *Appl. Catal., A* **2008**, *348*, 221.
- (395) Lanza, R.; Canu, P.; Jaras, S. G. *Appl. Catal., A* **2010**, *375*, 92.
- (396) Yao, Y.; Fu, Q.; Wang, Z.; Tan, D.; Bao, X. *J. Phys. Chem. C* **2010**, *114*, 17069.
- (397) Zecchina, A.; Rivalan, M.; Berlier, G.; Lamberti, C.; Ricchiardi, G. *Phys. Chem. Chem. Phys.* **2007**, *9*, 3483.
- (398) Yin, J.; Wang, J.; Zhang, T.; Wang, X. *Catal. Lett.* **2008**, *125*, 76.
- (399) Gülmen, M. A.; Sumer, A.; Aksoylu, A. E. *Surf. Sci.* **2006**, *600*, 4909.
- (400) Chin, S. Y.; Alexeev, O. S.; Amiridis, M. D. *J. Catal.* **2006**, *243*, 329.
- (401) Jain, A. K.; Briegleb, B. P.; Minschwaner, K.; Wuebbles, D. J. *J. Geophys. Res., [Atmos.]* **2000**, *105*, 20773.
- (402) Persson, K.; Jansson, K.; Jaras, S. G. *J. Catal.* **2007**, *245*, 401.
- (403) Castellazzi, P.; Groppi, G.; Forzatti, P. *Appl. Catal., B* **2010**, *95*, 303.
- (404) Hou, Z. Y.; Yokota, O.; Tanaka, T.; Yashima, T. *Catal. Lett.* **2003**, *89*, 121.
- (405) Zhao, X.; Yin, M.; Ma, L.; Liang, L.; Liu, C.; Liao, J.; Lu, T.; Xing, W. *Energy Environ. Sci.* **2011**, *4*, 2736.
- (406) Kowal, A.; Li, M.; Shao, M.; Sasaki, K.; Vukmirovic, M. B.; Zhang, J.; Marinkovic, N. S.; Liu, P.; Frenkel, A. I.; Adzic, R. R. *Nat. Mater.* **2009**, *8*, 325.
- (407) Strasser, P.; Koh, S.; Anniyev, T.; Greeley, J.; More, K.; Yu, C.; Liu, Z.; Kaya, S.; Nordlund, D.; Ogasawara, H.; Toney, M. F.; Nilsson, A. *Nat. Chem.* **2010**, *2*, 454.
- (408) Stephens, I. E. L.; Bondarenko, A. S.; Gronbjerg, U.; Rossmeisl, J.; Chorkendorff, I. *Energy Environ. Sci.* **2012**, *5*, 6744.
- (409) Epron, F.; Carnevillier, C.; Marecot, P. *Appl. Catal., A* **2005**, *295*, 157.
- (410) Aranishi, K.; Jiang, H. L.; Akita, T.; Haruta, M.; Xu, Q. *Nano Res.* **2011**, *4*, 1233.
- (411) Matsushita, T.; Shiraishi, Y.; Horiuchi, S.; Tushima, N. *Bull. Chem. Soc. Jpn.* **2007**, *80*, 1217.
- (412) Fang, P. P.; Duan, S.; Lin, X. D.; Anema, J. R.; Li, J. F.; Buriez, O.; Ding, Y.; Fan, F. R.; Wu, D. Y.; Ren, B.; Wang, Z. L.; Amatore, C.; Tian, Z. Q. *Chem. Sci.* **2011**, *2*, 531.
- (413) Zhang, S.; Guo, S. J.; Zhu, H. Y.; Su, D.; Sun, S. H. *J. Am. Chem. Soc.* **2012**, *134*, 5060.
- (414) Frenkel, A. I.; Wang, Q.; Marinkovic, N.; Chen, J. G.; Barrio, L.; Si, R.; Lopez Camara, A.; Estrella, A. M.; Rodriguez, J. A.; Hanson, J. C. *J. Phys. Chem. C* **2011**, *115*, 17884.
- (415) Chen, H.; Wen, W.; Wang, Q.; Hanson, J. C.; Muckerman, J. T.; Fujita, E.; Frenkel, A. I.; Rodriguez, J. A. *J. Phys. Chem. C* **2009**, *113*, 3650.
- (416) Hwu, H. H.; Chen, J. G. *Chem. Rev.* **2005**, *105*, 185.
- (417) Gouy-Pailler, P.; Pauleau, Y. *J. Vac. Sci. Technol., A* **1993**, *11*, 96.

- (418) Esposito, D. V.; Hunt, S. T.; Kimmel, Y. C.; Chen, J. G. *J. Am. Chem. Soc.* **2012**, *134*, 3025.
- (419) Esposito, D. V.; Chen, J. G. *Energy Environ. Sci.* **2011**, *4*, 3900.
- (420) Hsu, I. J.; Kimmel, Y. C.; Jiang, X. G.; Willis, B. G.; Chen, J. G. *Chem. Commun.* **2012**, *48*, 1063.
- (421) Kelly, T. G.; Chen, J. G. *Chem. Soc. Rev.* **2012**.
- (422) Saliccioli, M.; Chen, Y.; Vlachos, D. G. *J. Phys. Chem. C* **2010**, *114*, 20155.
- (423) Saliccioli, M.; Vlachos, D. G. *ACS Catal.* **2011**, *1*, 1246.